STUDY OF CATCHER BEARINGS FOR HIGH TEMPERATURE MAGNETIC BEARING APPLICATION

A Thesis

by

ASHWANTH NARAYANASWAMY

Submitted to the Office of Graduate Studies of
Texas A&M University
in partial fulfillment of the requirements for the degree of

MASTER OF SCIENCE

May 2011

Major Subject: Mechanical Engineering

STUDY OF CATCHER BEARINGS FOR HIGH TEMPERATURE MAGNETIC BEARING APPLICATION

A Thesis

by

ASHWANTH NARAYANASWAMY

Submitted to the Office of Graduate Studies of
Texas A&M University
in partial fulfillment of the requirements for the degree of

MASTER OF SCIENCE

Approved by:

Chair of Committee,	Alan B. Palazzolo
Committee Members,	Gary Michael Gaukler
	Sai Chuen Lau
Head of Department,	Dennis O'Neal

May 2011

Major Subject: Mechanical Engineering

ABSTRACT

Study of Catcher Bearings for High Temperature Magnetic Bearing Application.

(May 2011)

Ashwanth Narayanaswamy, B.E., Kumaraguru College of Technology, India

Chair of Advisory Committee: Dr. Alan B. Palazzolo

The Electron Energy Corporation (EEC) along with National Aeronautics and Space Administration (NASA) in collaboration with Vibration Control and Electro mechanics Lab (VCEL), Texas A&M University, College Station, TX are researching on high temperature permanent magnet based magnetic bearings.

The magnetic bearings are made of high temperature resistant permanent magnets (up to 1000 ^{o}F). A test rig has been developed to test these magnetic bearings. The test rig mainly consists of two radial bearings, one axial thrust bearing and two catcher bearings. The test rig that the catcher bearing is inserted in is the first ultra-high temperature rig with permanent magnet biased magnetic bearings and motor. The magnetic bearings are permanent magnet based which is a novel concept. The Graphalloy bearings represent a new approach for ultra-high temperature backup bearing applications.

One of the main objectives of this research is to insure the mechanical and electrical integrity for all components of the test rig. Some assemblies and accessories required for the whole assembly need to be designed. The assembly methods need to be designed. The preliminary tests for coefficient of friction, Young's modulus and thermal expansion

characteristics for catcher bearing material need to be done. A dynamic model needs to be designed for studying and simulating the rotor drop of the shaft onto the catcher bearing using a finite element approach in MATLAB.

The assembly of the test rig was completed successfully by developing assembly fixtures and assembly methods. The components of the test rig were tested before assembly. Other necessary systems like Sensor holder system, Graphalloy press fit system were designed, fabricated and tested. The catcher bearing material (Graphalloy) was tested for coefficient of friction and Young's modulus at room and high temperatures. The rotor drop was simulated by deriving a dynamic model, to study the effect of system parameters like clearance, coefficient of friction, negative stiffness, initial spin speed on system behavior.

Increasing the friction increases the backward whirl and decreases the rotor stoppage time. Increasing the clearance reduces the stoppage time and increases the peak bearing force. Increasing the initial spin speed increases the rotor stoppage time. The maximum stress encountered for as built conditions is more than allowable limits.

DEDICATION

This piece of work is dedicated to my best friend, Mr.Karthik Srinivasan.

ACKNOWLEDGEMENTS

I would like to express my heartfelt thanks to my advisor Dr. Alan B. Palazzolo, for his advice and patience throughout this research. I would also like to thank Dr. Gary Gaukler and Dr. Sai Lau for being on my thesis committee and their continuous support.

I would like to thank Mr. Randall Tucker for his never dying enthusiasm and help in assembling the test rig together. Special thanks to my close friend, Vishal Wadhvani, for his support and ideas.

Special thanks to my boss, mentor and well-wisher, Dr. Juan Carlos Baltazar, for his support, help, kind words and concern during my stint at ESL, TAMU and during the course of my research.

I would like to thank Layne Wylie, Jeff, Alex, Cole, Johnny Hallford and George of the mechanical engineering machine shop, for offering specialized technical assistance during crucial times.

My heartfelt thanks to Jung Gu Lee for his help in the MATLAB code.

Special thanks to Sandip Hodkhasa for helping us in the assembly during crucial times.

I would like to extend my heartfelt thanks, to Jacob Manuel for his help.

I would like to extend my heartfelt thanks to Kirthiram, Jai Lopez, Karthic for their kind support.

My heartfelt thanks to Xiahoua Zhang, JunHo Su, Zhengxin Zhang, Kyungdae Kang, Zhiyang Wang, Shawn Hagler, Matt Walker, Christopher Hern and others who shared time with me in the Vibration Control and Electro mechanics Laboratory. I would also like to thank Mr. Andrew Provenza of NASA Glenn Research Center and Dr. Heeju Choi of Electron Energy Corporation (EEC) for their continuous support in this project.

I would like to thank my dad, mom, brother, sister, sister in law and my friends for keeping their faith in me.

A large portion of this thesis relates to the development of a unique test rig, to test a full rotating shaft system at 1,000 F. This required extensive machining, designing, welding, and component testing, measuring, and planning tasks which for safety and efficacy reasons had to be performed with my graduate MS student colleague (Vishal Ashok Wadhvani). Thus significant portions of this thesis, appears in my colleagues thesis, since it would be impossible to separate independent contributions on the development of the test rig. My clearly independent contributions include component testing and simulations related to the catcher bearing.

TABLE OF CONTENTS

Page

Page

Page

Page

LIST OF FIGURES

Page

Page

Page

Page

Page

LIST OF TABLES

Page

Page

1. INTRODUCTION

1.1 Magnetic bearings

Magnetic bearing is an electromagnetic device which supports a moving rotor without physical contact.

The magnetic bearings are one of the major achievements in the field of rotating machinery. Its main feature is that there is no contact between the rotating parts. Since there is no contact between the shaft and the bearing, there is no friction, and therefore the bearing losses are kept to a bare minimum. The bearing losses are 5 to 20 times less than that in the case of ball or journal bearings. The absence of contact, results in low mechanical wear and thereby higher life expectancy of the system [1].

There is no need for lubrication and thereby contamination free operating environment. Also it is very much suitable for applications that require operation in sterile environments and vacuum conditions.

With magnetic bearings operating at high speeds becomes a possibility. Very high peripheral speeds could be achieved using magnetic bearings. The only limitation to the high circumferential speed is the strength of the material of the rotor [1].

With active magnetic bearings the stiffness and damping could be controlled using

---

This thesis follows the style and format of ASME: Journal of Tribology.

control electronics.

Since the stiffness and damping could be controlled, the dampening of vibrations could also be controlled effectively.

With magnetic bearings the operation of the rotor could be controlled with high precision. The precision could vary anywhere in the range of 1/100 to 1/1000 of a millimeter [1]. The precision largely depends upon the quality of the sensors used to determine the position of the rotor.

Also the dynamic forces due to unbalance could be reduced by making the rotor rotate about its inertial axis. So the rotor of an active magnetic bearing need not be balanced.

Two salient features of the magnetic bearing system:

- Requirement of a catcher bearing/ backup bearing system to ensure that the shaft hits the catcher bearings first in case of power loss or failure of magnetic bearings thereby protecting the magnetic bearings.
- The magnetic bearings behave in contrast to a mechanical spring. More the air gap lesser the force generated, thereby the magnetic bearings have negative stiffness.

1.1.1 *Applications of magnetic bearings*

The following are the main applications of magnetic bearings [1] among others:

- Flywheel energy storage due to the absence of aerodynamic drag losses and low power consumption.
- Operation in vacuum and sterile conditions due to absence of lubrication and thereby the contamination.
- Turbo machinery for low bearing losses and good vibration damping control.
- Machine tools for high rotational speed and good precision control.
- Medical devices.
- Superconducting bearings.

1.1.2 *Disadvantages of magnetic bearings*

- The expensive nature is one of the major disadvantages.
- Design for high temperature applications are complex.

1.1.3 *Types of magnetic bearings*

The magnetic bearings are divided into two types [1]:

1. Active magnetic bearings.
2. Passive magnetic bearings.

In the active magnetic bearings an electromagnet is used along with a feedback control system consisting of sensors, control electronics, power amplifiers etc. A passive magnetic bearing uses only permanent magnets to levitate the shaft. The active magnetic bearings have a lot advantages over the passive magnetic bearings viz. control of static and dynamics stiffness, damping, load independent static positioning etc. But the passive magnetic bearing has only a fixed set of properties.

1.2 An introduction to the current research

The current research supported by Electron Energy Corporation (EEC) and National Aeronautics and Space Administration (NASA) is on active magnetic bearings for high temperature applications. The magnetic bearings make use of high temperature permanent magnets (HTPM) developed by EEC. The bearing system has been designed to carry a design load of 500 lb. [2] .The components of the system include: two radial bearings, one thrust bearing, one permanent magnet brushless DC motor and two catcher bearings. The two catcher bearings make use of a solid lubricant called Graphalloy.

The two HTRMB (high temperature radial magnetic bearings) and one axial bearing provide the radial and axial force necessary to levitate the shaft. The magnetic bearings are protected / backed up by two catcher bearings-in case there is a failure of the magnetic bearings/ power loss. Mr. Zhengxin Zhang has worked on the development of the brushless DC motor [2]. It can produce power in the range of 3.75 to 7.5 kW with maximum speed of 20000 rpm.

On successful completion, these kinds of bearings can be used in high performance, high temperature and high speed applications like space vehicles, jet engines and deep sea equipment [3].

1.3 Scope of the research

The current research deals with the following the tasks, problems and challenges that were faced in the assembly and final testing stage:

- Successful assembly of all the components in the test rig by developing fixtures and methods for assembly.
- Due to the nature of the high radial forces that would be involved during the magnetic levitation testing, assembly of the internal components of the rig need to be rigid with absolutely no allowance for movement.
- Due to the fragile nature of the most internal parts and very small air gap among other reasons it's highly mandatory to insure the mechanical integrity of the components of the test rig.
- Due to extremely small air gap (about 0.030 inches or 30 mils) the magnetic bearings need to be installed with very little tolerance for concentricity.
- Study of the properties of Graphalloy and their change with respect to temperature to be studied to design the catcher bearing effectively.

- Design of catcher bearings that can function effectively at 1000 F by conducting basic stress analysis.
- Simulate the vibrations of the falling rotor onto catcher bearings by deriving the equations of motion simulating it using a MATLAB code.
- Perform a parametric study of the effect of spin speed and coefficient of friction on the vibrations of the rotor.
- Design and fabrication of sensor holder assembly, calibration and testing of the sensors and other components involved, and to ensure minimal noise due to vibration or other external sources.
- Interface of all the internal components of the test rig and all external components (control electronics) with high priority given to ensure personnel safety while testing of the magnetic bearings.

1.4 Literature review

G. Sun, A.B. Palazzolo and others performed numerical simulations of a rotor drop on CBs in flywheel energy storage system [4]. It was conducted assuming a Hertzian load–deflection relationship between mechanical contacts, speed-and preload dependent bearing stiffness due to centrifugal force, and a Palmgren's drag friction torque.

G.Sun did the numerical analysis of a rotor drop on catcher bearings and resulting thermal growths due to their mechanical rub using catcher bearing and damper models [5]. The catcher bearing was modeled based on its material, geometry, speed and preload using the Hertzian load–deflection formula, and the thermal growths of bearing components during the rotor drop were estimated using a one dimensional thermal model.

In another study by [6] Antti Ka¨rkka¨ inen and others, the dynamics of rotor supported by active magnetic bearings during the drop on catcher bearings was studied employing a detailed simulation model. The catcher bearings were modeled using a ball bearing model which takes into account damping and stiffness properties, oil film, inertia of rolling elements and friction between races and rolling elements. The model of a flexible rotor system accounts for unbalances and stiffness and damping properties of the support.

R.G.Kirk [7] reviewed the analytical techniques for rotor transient response. The results of transient response predictions were presented to signify the important parameters in the design for rotor drop. An extended Jeffcott model was used for the modeling of a symmetric rotor-beam type model. Kirk concluded that required damping levels for a safe rotor drop will depend upon total rotor weight, amount and distribution of rotor imbalance, the location of the rotor free-free mode, the location of the rotor rigid bearing first bending mode with support at the auxiliary bearing axial locations. He showed that a balanced rotor condition is required to lessen the possibility of the forward whirl. He

showed that soft mount lubricated surface gives the best performance for both initial impact force level and peak transient force levels. He also recommends step balance of rotors to reduce dynamic couples.

In another study by Kirk [8] a theoretical formulation for the transient response of the flexible rotor was proposed and solved numerically .The objective of this study was to get the orbit of the rotor and to determine the forces acting on the rotor and backup bearing. The destructive back whirl of the rotor could be analytically predicted at very light support damping / high support damping. The backward whirl would cause a high contact force. An optimum support damping ratio was recommended.

In yet another study [9] Kirk did the analysis for rotor transient response during the rotor drop onto the catcher bearings of the classical antifriction type. The results deal with some of the areas of concern and show how the rotor can experience either forward or backward whirl after the drop.

In yet another study [10] Kirk did the transient response and contact force evaluation of full-size test rotor for various levels and distribution static and dynamic unbalance. The recommendations for shop testing to increase the probability of stable operation are also given.

Varun Rajesh Gandhi did extensive work for his thesis project [3] in the design and fabrication of permanent magnet based magnetic bearings (axial and radial bearings), experimental measurement of position, current stiffness etc.

Zhengxin Zhang did extensive work on the high temperature motor [2] made of EEC permanent magnets for his thesis project. In this study the numerical values of the voltage, power and torque output were predicted from the non-linear finite element model of the rotor. He developed an open loop approach and succeeded in spinning the rotor with capability of self-starting.

In study by Schweitzer, G., Bleuler, H. and Traxler [1], deal with basic properties and applications of magnetic bearings. They deal with different kinds of magnetic bearings, their similarities and differences, design of controls to achieve feedback control and other issues.

In a study by J.Schmied and J.C.Pradetto [11] the behavior of a one ton compressor rotor being dropped on auxiliary bearings (ball bearings was reported). They determined that the most critical conditions are the whirling conditions and they concluded that the whirling condition must be prevented by an appropriate design.

1.5 What is the novelty?

The present research is a bit different and deals with magnetic bearings in a high temperature environment to the order of 1000 ^{o}F. The usage of Graphalloy bearings is a new approach in the process instead of bearings with rolling elements. The purpose of this research study is to study and simulate the rotor drop in these above mentioned circumstances.

2. EXPERIMENTAL SETUP OF THE TEST RIG

2.1 Overall setup

The whole assembly consists of two radial bearing, one thrust bearing with built in catcher, two catcher bearings, and one motor is shown Figure 2-1. A rotor with multiple pieces is supposed to be levitated with the help of the bearings and spun with the help of the motor. All these internal parts are assembled meticulously within a thick outer cylinder cast out of low carbon steel.

Each of the bearings is sandwiched between two stator plates. These stator plates sit at corresponding locations in the inside of the cylinder. The arrangement and order of the internal parts is as shown in the figure. The motor sits between the two radial bearings. One catcher bearing on the top of the top radial bearing and another catcher bearing below the bottom radial bearing are the backup bearings. They prevent the shaft from hitting the radial bearings and thereby protecting them.

The cut section is as shown in Figure 2-2 below. One could see the sensor locations in the cut section. Two sensors at the top (at right angles) and two sensors at the bottom (correspondingly below the top sensors and at right angles) allow to have the feedback loop with the controller possible. The top sensors are kept above top catcher bearing. A special washer has been machined so as to provide for the target surface. The axial sensor (the fifth sensor) sees the bottom of the shaft from under the axial bearing.

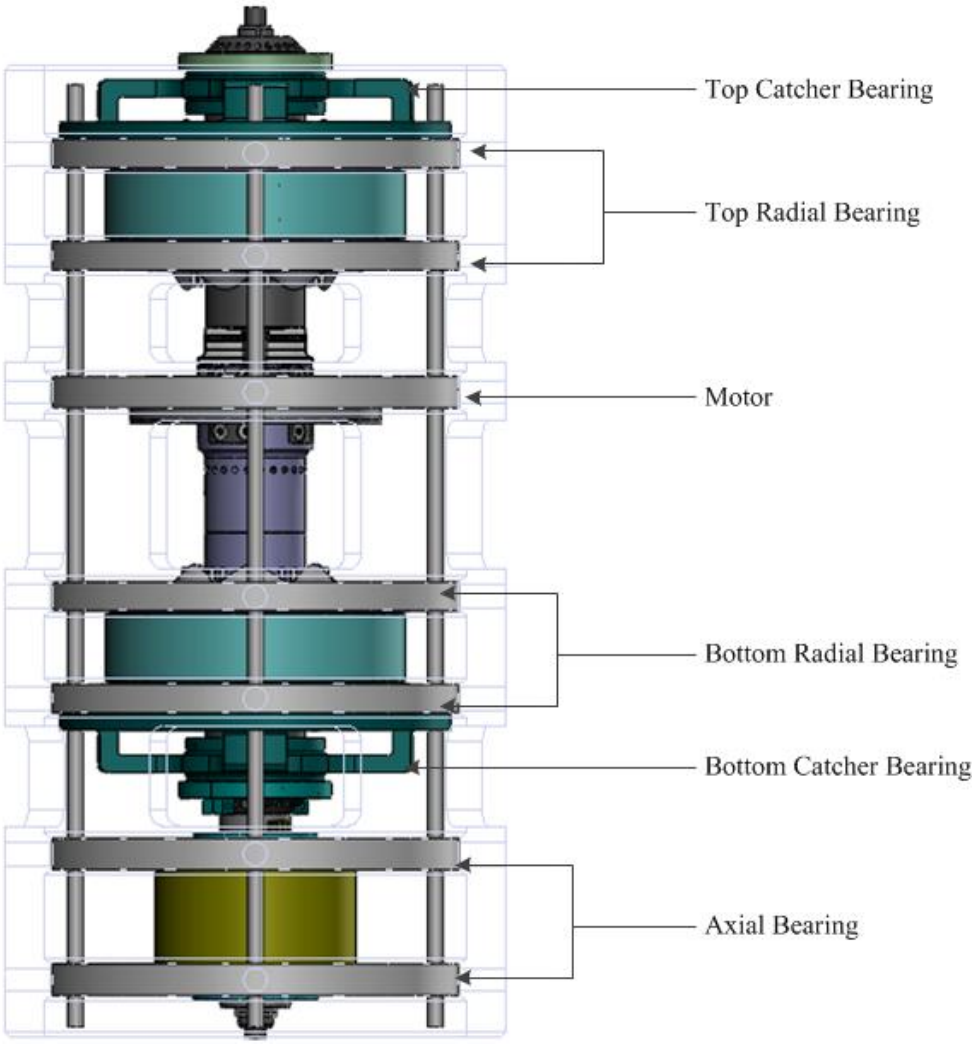

Figure 2-1 Different components of the magnetic bearing test rig

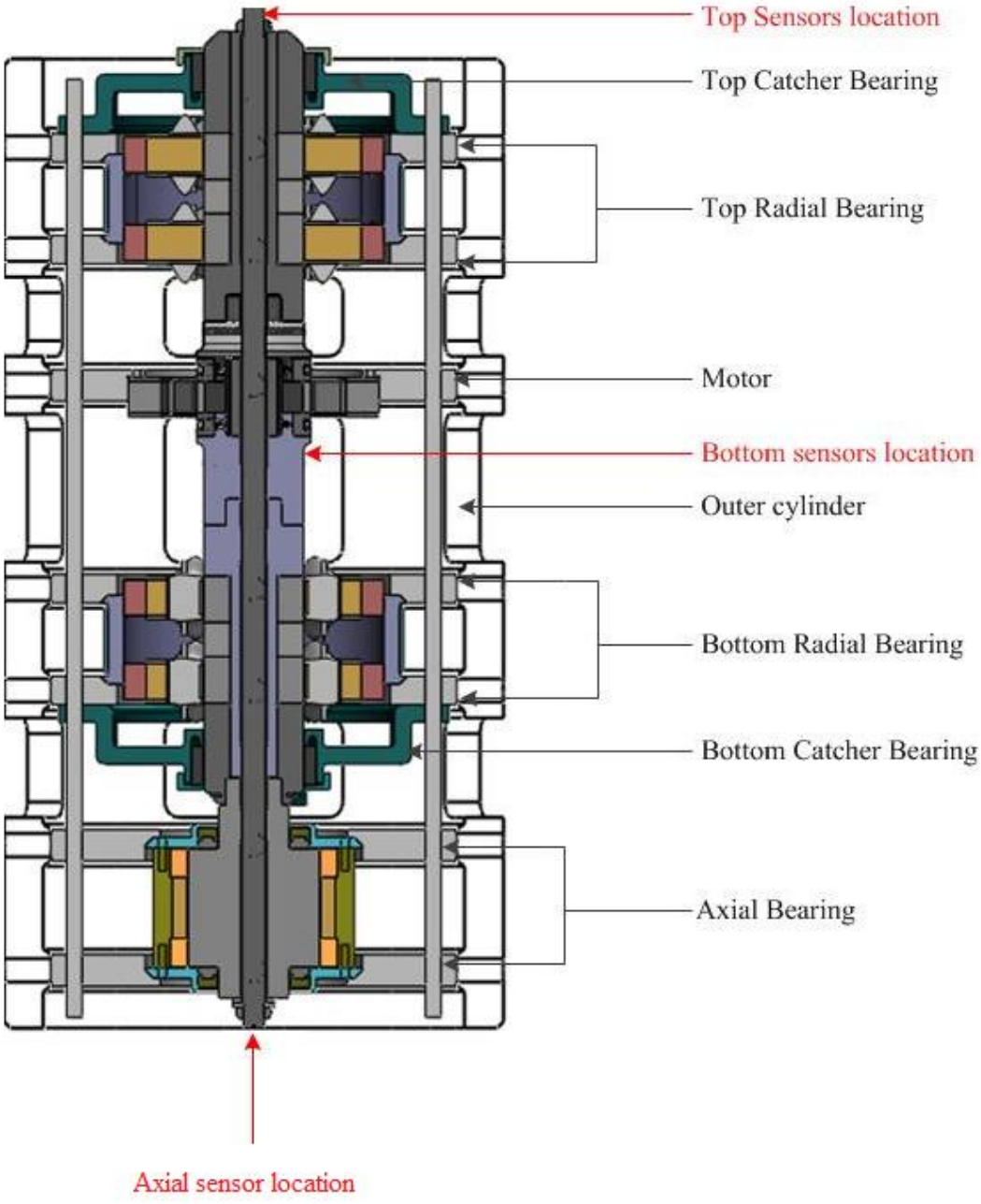

Figure 2-2 Cut section of the magnetic bearing test rig

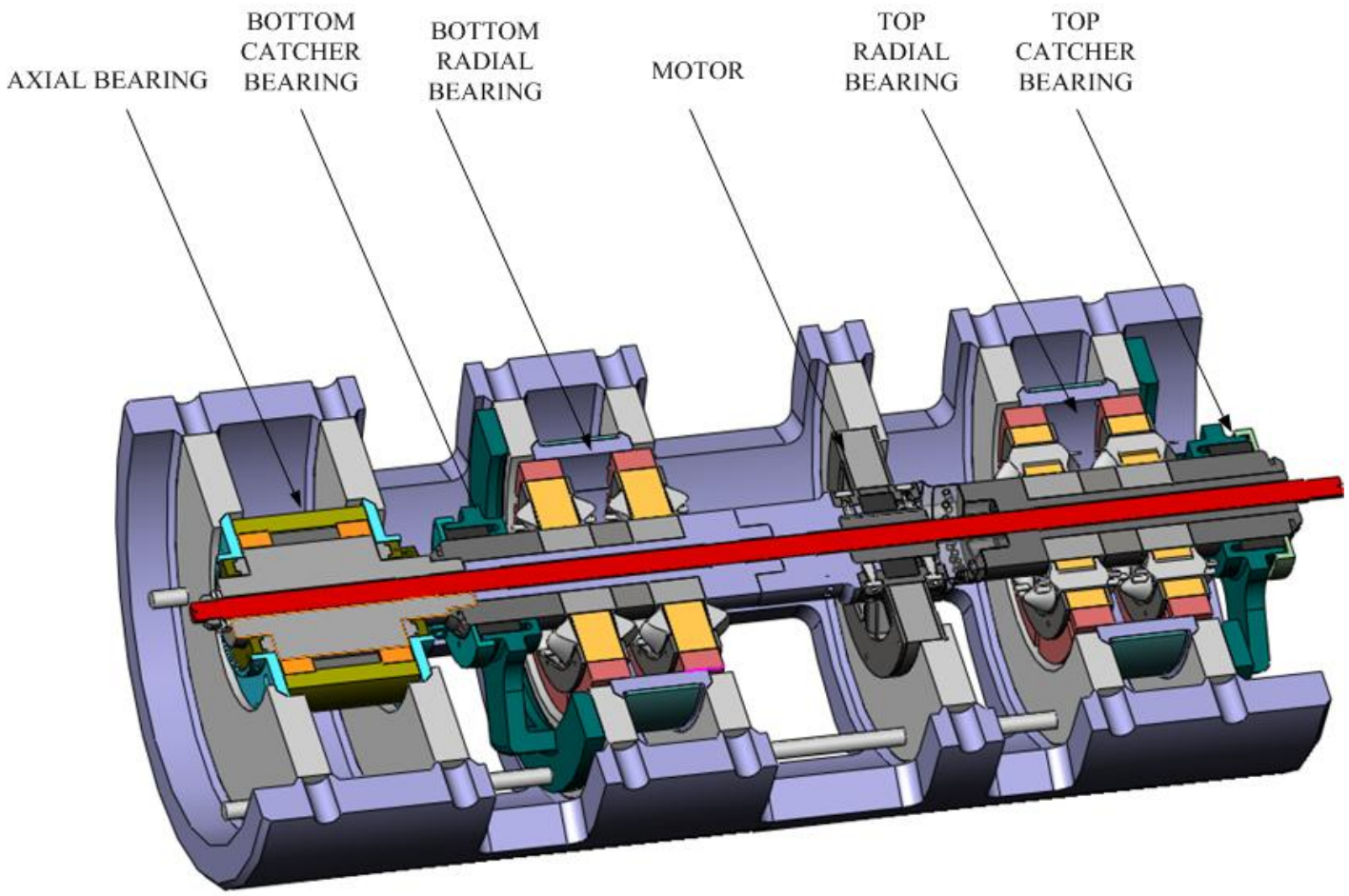

Figure 2-3 3-D section view of the magnetic bearing test rig

The test rig cut section in 3D is as shown in Figure 2-3; there are 7 stator plates at different heights (two each for axial bearing and two radial bearings and one for motor). The catcher bearings (one under the bottom radial bearing and another one on top of the top radial bearing could be clearly seen). One could also see the different pieces of the rotor (with interference fits) being held together by a tie shaft rod (shown in red). The tie shaft is locked from the top and bottom using locknuts). The tightening torque of the locknuts helps to keep the rotor rigid.

2.2 Outer cylinder

Figure 2-4 Outer cylinder

Figure 2-4 shows the outer cylinder in the test rig. The outer cylinder rests on four pins and is also supported from the sides by 8 radial pins (4 on top and 4 on bottom).The support pins ensure that outer cylinder is supported well and also that the heat losses due to conduction (by direct metal to metal contact) is minimum.

The cylinder is mounted to a floor mounted stand which is attached to the ground/concrete.

Figure 2-5 Support pins for outer cylinder

Figure 2-5 above shows the bottom part of the outer cylinder with supports from side

support pins and bottom support pins. Before assembling the bearings and motor inside the outer cylinder were leveled using spirit levels.

2.3 Stator plates

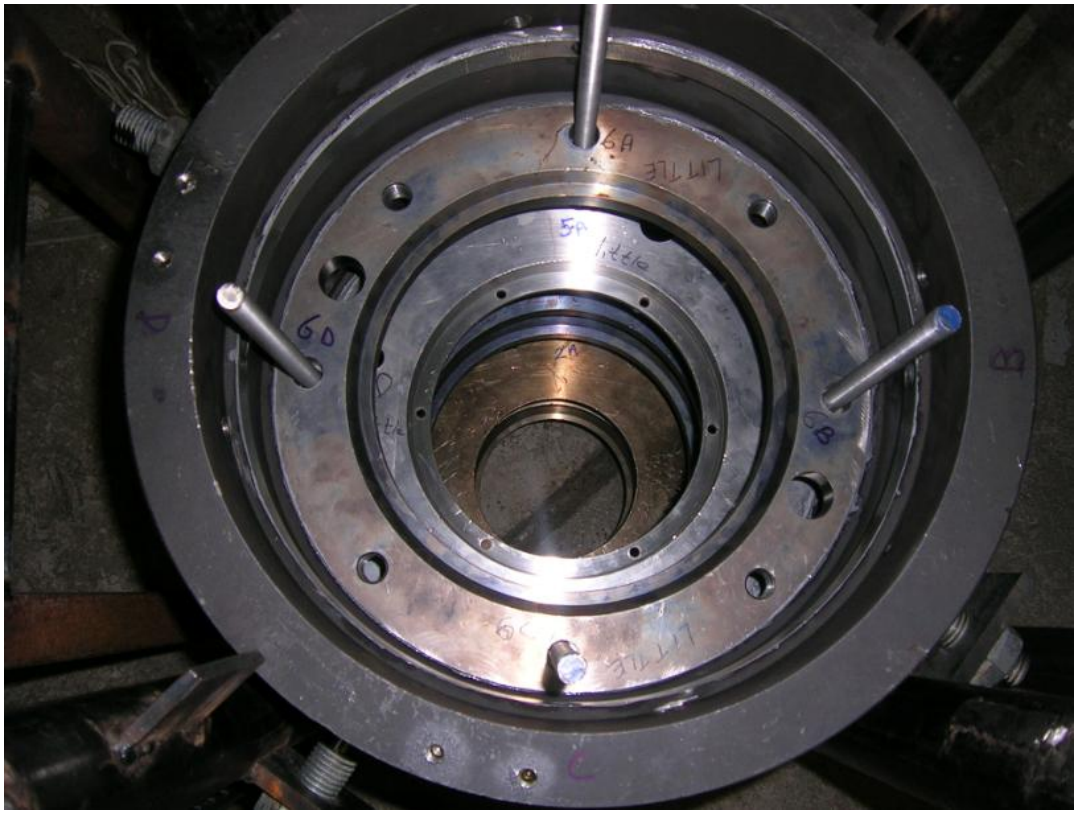

Figure 2-6 Stator plates assembled inside the cylinder

Figure 2-6 above shows the arrangement of the stator plates inside the outer cylinder. The stator plates are aligned using four all thread rods that go all the way to the bottom of the cylinder. The all thread rods are held in place by securing them to a locator plate

at the bottom. The nuts above and below the stator plates provide the axial support for the stator plates. There are provisions on the side of the cylinder to screw in setscrews which go touch the stator plates. Four radial set screws at 90 degrees provide the radial support for the stator plates. It is as shown in Figure 2-7.

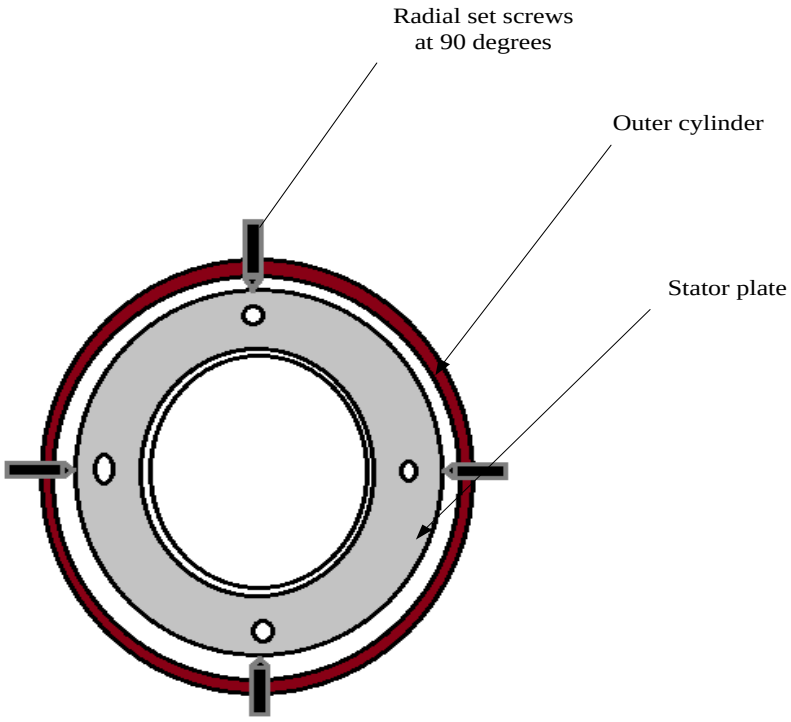

Figure 2-7 Stator plates-radial support

Figure 2-8 Stator plates axial support

The double nuts under the stator plates (mounted on each of the four all threads) provide the axial support and are shown in Figure 2-8 .

2.4 Radial bearings

There are two radial bearings. Both are identical though. One is the top radial bearing and the other one is the bottom radial bearing.

The main parts of the radial bearing are:[3]

1. Rotor lamination stacks

2. Stator lamination stacks

3. Permanent Magnets

4. Segmented back iron

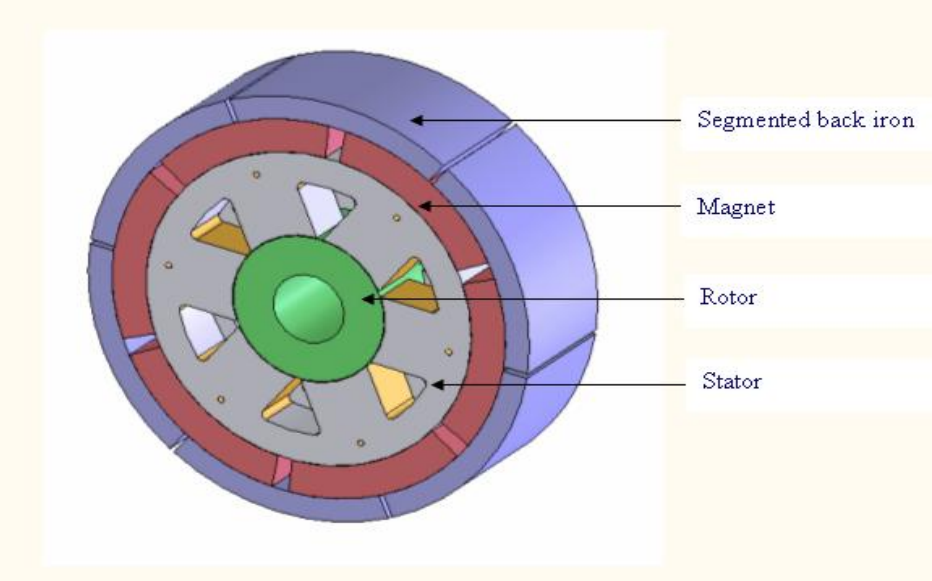

Figure 2-9 Radial magnetic bearing

The 3D model of radial bearing is as shown in Figure 2-9. The radial bearing consists of two planes. (Top and bottom plane) on either sides. Each plane has six permanent magnets. From one of the poles the bias flux is pushed into the rotor. The bias flux then returns to the other plane by passing through the rotor laminations. The back iron plates helps to conduct the bias flux in the axial direction.Both the poles of the motor are revresely polarized[3].

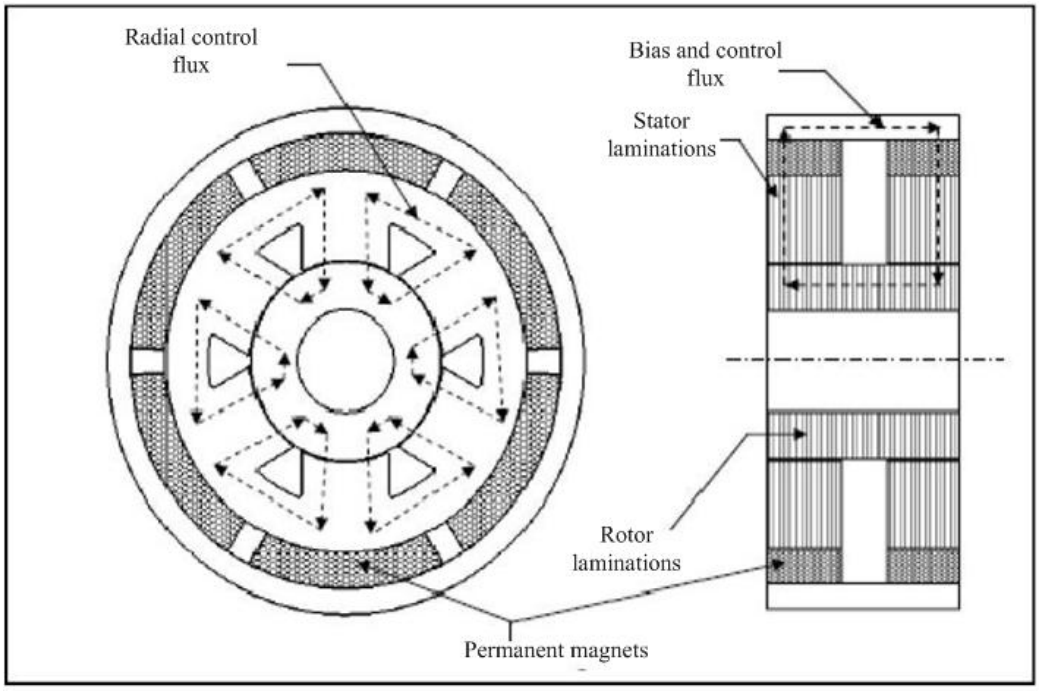

Figure 2-10 Flux flow for radial magnetic bearing

The flux flow is shown in Figure 2-10. The control flux is generated due to the current flowing through the coils. This current flow through the coils is controlled by the feed back control system. This control flux circulates radially. The system has been designed in a way that the bias flux + control flux acts on one side of the rotor and bias flux - control flux acts on the other side of the rotor. This produces a net force on the rotor. Since the net current flowing through the coils is controllable this net force is also controllable.

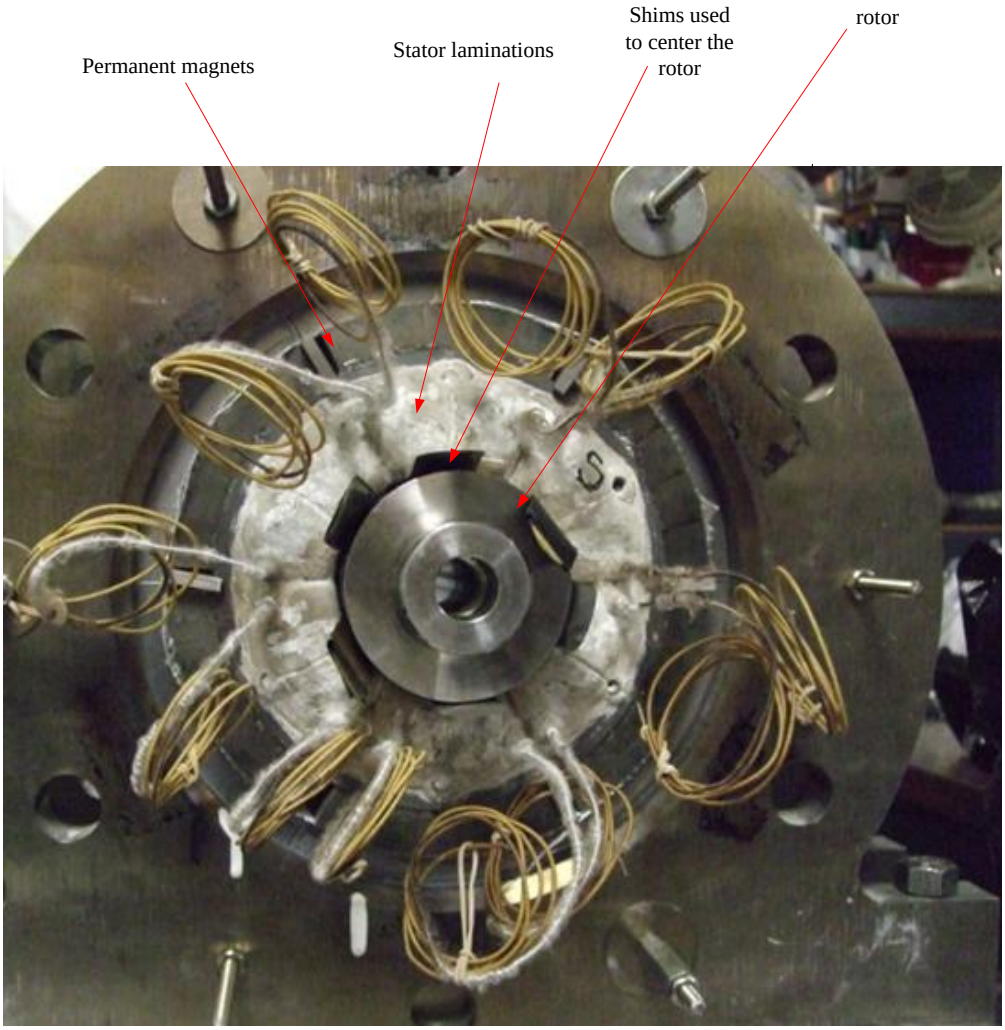

Figure 2-11 Radial magnetic bearing

The radial bearing with attached end plates, rotor and stator laminations are clearly seen in Figure 2-11. The shims are used to center the rotor (approximately) before assembling it inside the rotor. These shims were inserted by an arduous and time consuming process.

Outer diameter of rotor	=	3.186 in
Total diametric thickness of shims	=	0.039in
Inner dia of radial bearing = 3.186+0.039	=	3.225 in

2.5 Axial bearing

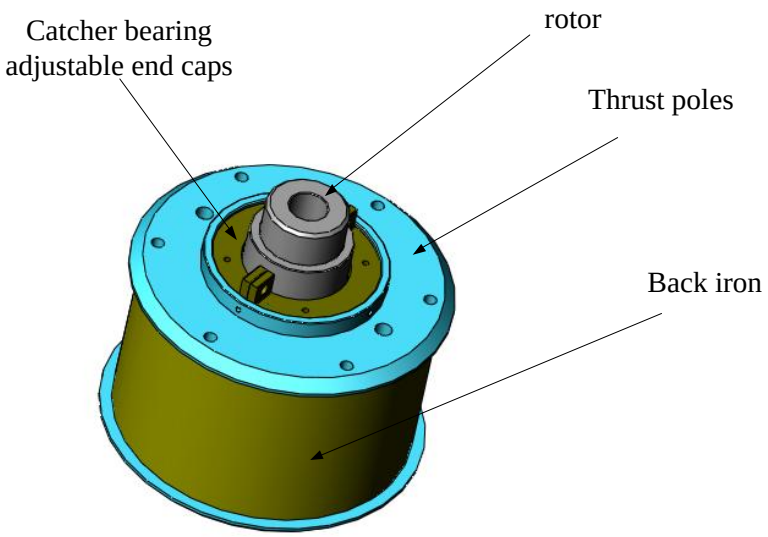

Figure 2-12 Axial bearing

The axial bearing shown in Figure 2-12 consists of the following main parts:

- Back iron.
- EEC high temperature permanent magnet.

- Thrust bearing coils.
- Rotor.
- Axial poles/thrust poles.

The principle of working of the axial bearing is same as that of the radial bearing. The difference is thatthere is no radial force control coils and that a solid rotor is used. The two axial poles are bolted to each other using holes in the back iron.The catcher bearings are located on either sides on the axial poles. The catcher bearing allowance could be adjusted by adjustable endcaps. The back iron, rotor and the axial poles are made out of Hiperco-50. The cut section is shown in Figure 2-13.

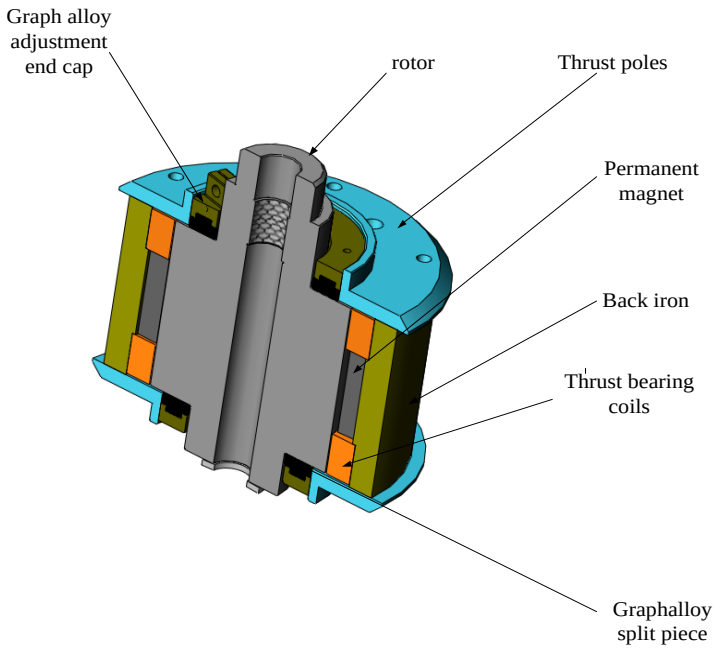

Figure 2-13 Axial bearing-cut section

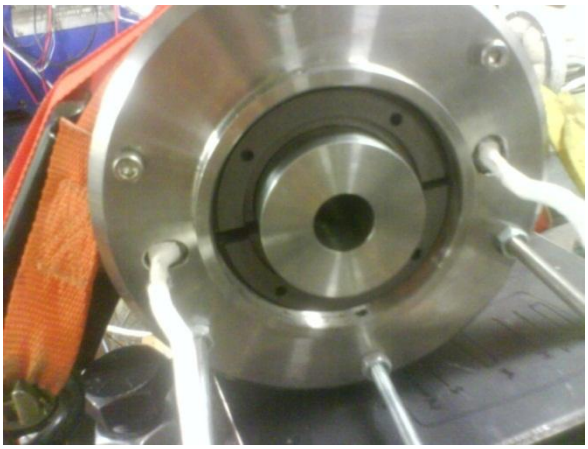

Figure 2-14 Axial bearing-graph alloy split pieces

The Figure 2-14 shows the Graphalloy split pieces in the catcher bearing on one of the sides.These catcher bearing plates provide axial protection for the bearing.

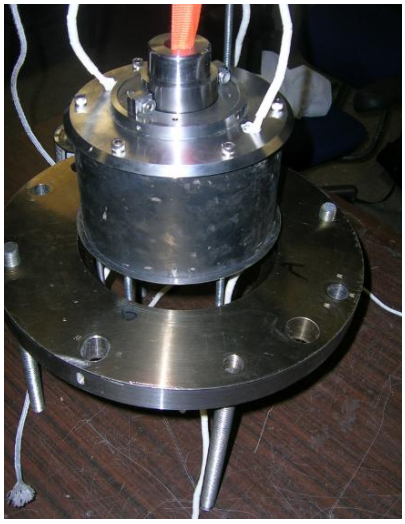

Figure 2-15 Axial bearing – aligned onto the bottom stator plate

The Figure 2-15 shows a fully assembled thrust bearing. The thrust bearing is assembled on its corresponding bottom stator plate so that it could be assembled into the rig.

2.6 Motor

The motor is capable of operating at high temperatures up to 1000 ^{o}F. The power output ranges from 3.75 to 7.5 kW. The stator has 6 poles while the rotor has 4. The motor is capable of self-starting with a three phase controller. The maximum ampere and voltage ratings are 10A and 24V respectively. Mr.Zhengxin Zhang has worked extensively in developing this high temperature motor [2].

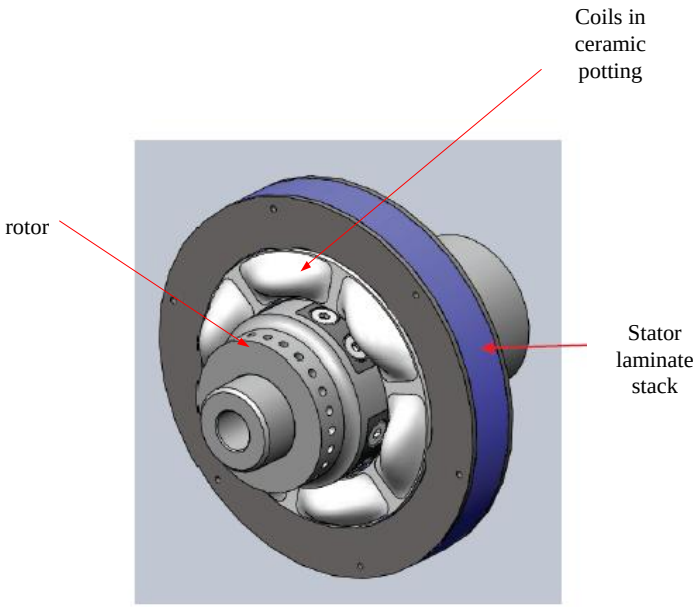

Figure 2-16 Motor

A 3D model of the motor is as shown in Figure 2-16. The motor consists of stator laminate stacks, motor coils buried in ceramic potting, rotor. The rotor before assembly is held at center approximately by means of using shims.

2.6.1 *Rotor*

The rotor consists of four T550 magnets which are oriented to make magnetic flux flow circumferentially through them. The Figure 2-17 shows the magnets are buried inside the rotor. The buried magnets are placed in such way that the north south orientation alternates around the rotor. Each magnet repels the magnets adjacent to it.

Thus the rotor has two north and two south poles. To get this construction, it is made of two materials Hiperco-50 (Cobalt-iron-vanadium alloy) and Inconel -718. Inconel 718 is non-magnetic and Hiperco-50 has high permeability [2].

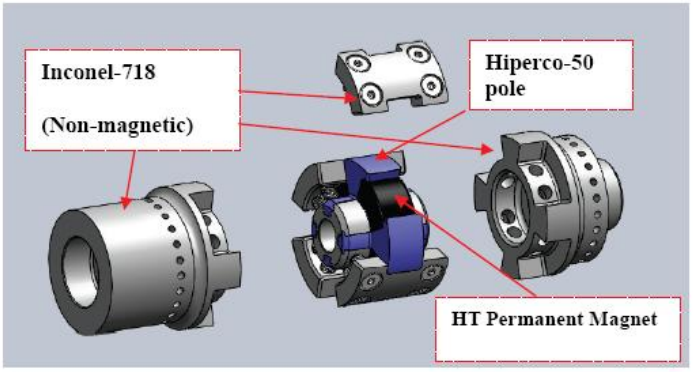

Figure 2-17 Rotor parts (corresponding to the motor)

2.6.2 *Stator*

The stator as shown Figure 2-18 has 6 poles. The stator laminate stacks are made of Hiperco-50. Each of the 6 poles has a coil wound. The figure shows the coil being wound on the poles. After the coils are wound, they were buried in ceramic potting. So, the coils will not be visible outside. The coils on the stator poles are in series with the corresponding coil which is at 180 degree. Thus the six poles are converted into three electric coil pairs [2].

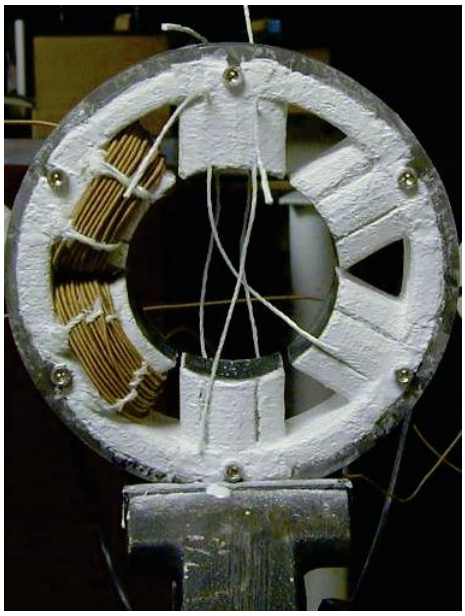

Figure 2-18 Stator for motor

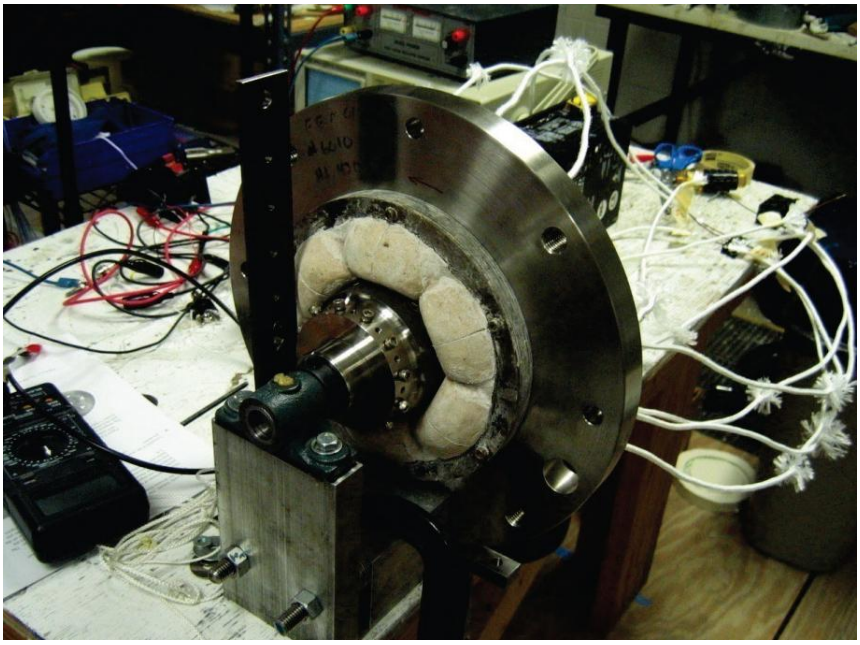

Figure 2-19 Rotor subassembly-ready for assembly

The Figure 2-19 above shows the motor subassembly in assembled condition with rotor inside.

2.7 Catcher bearing

The catcher bearings/retainer bearings act as protection for the main radial bearings in case there is a power loss or if there is a fault with the controller or the radial bearings itself / any other reason. The rotor hits the catcher bearing and not the radial bearing. In other words the clearance between the shaft/rotor and the catcher bearing is less when compared to the clearance between the radial bearings and the shaft/rotor.

At the radial bearings:

Outer diameter of shaft	:	3.186 in
Inner diameter of graph alloy	:	3.205 in
Net diametrical clearance	:	0.019 in

Net allowable clearance between the rotor and radial bearing: 0.039 in.

The catcher bearing has Graphalloy, which acts as the solid lubricant. It is an alloy of graphite and it's capable of operating at temperatures up to 1500 ^{o}F. The Graphalloy is manufactured by a company called Graphite Metalizing Corporation. It works at high temperatures whereas oil-based lubricants oxidize. It also works in run dry applications. It is capable of operating up to 100,000 rpm.

The catcher bearing as shown in Figure 2-20 has an Inconel catcher bearing central housing /plate. The Graphalloy is a single piece with a taper on its outer surface. A split stainless steel shell, which has a taper on its inner surface, is placed on top of washer inside the catcher bearing housing. The Graphalloy forms a tapered press fit with the shell. The tapered press fit calculations are dealt with in a separate section in this report. The press fit has been designed so that the interference would exist even at higher temperatures. The interference fit could be adjusted by turning an end cap which pushes the Graphalloy piece further inside thereby increasing the interference.

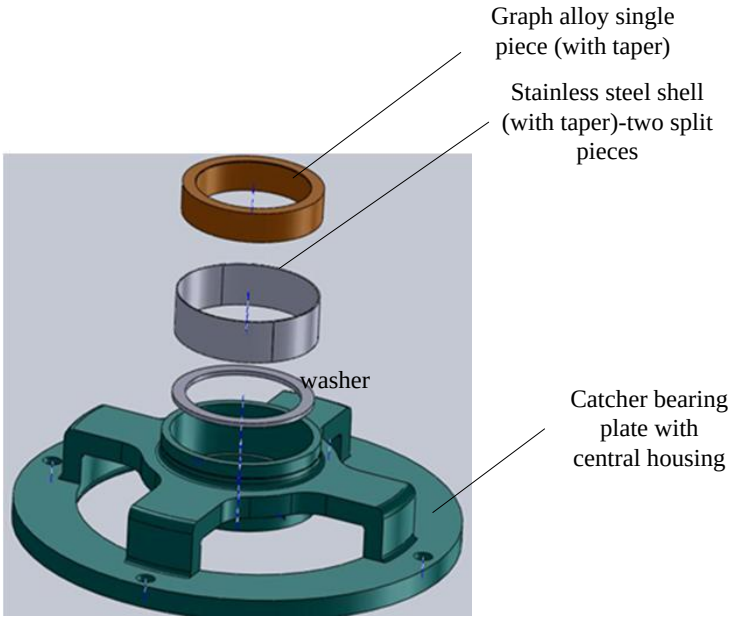

Figure 2-20Catcher bearing subassembly-ready for assembly

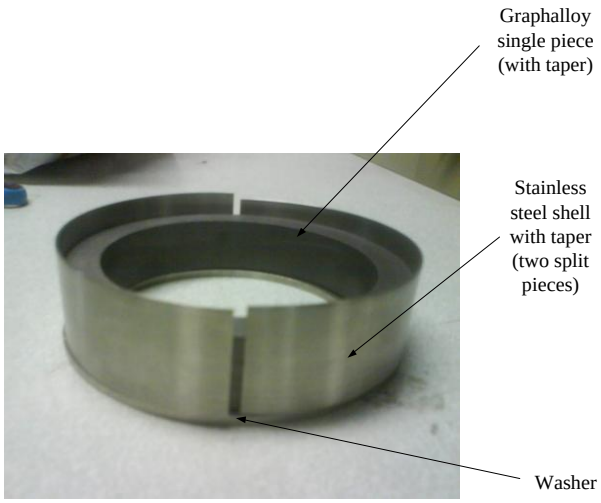

Figure 2-21 Graphalloy, shell and washer for catcher bearing

The Graphalloy, shell and washer are arranged inside the catcher bearing casing as in Figure 2-21.

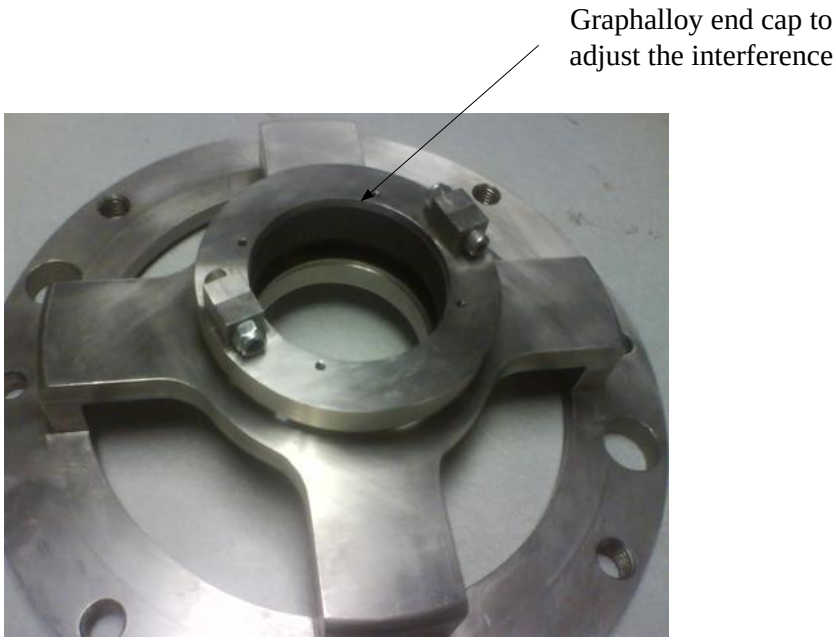

Figure 2-22 Catcher bearing-end cap

Installation of Graphalloy end cap is shown in Figure 2-22.

2.8 Rotor

The rotor complete assembly is as shown in Figure 2-23. Before assembling into the test rig, the rotor is not assembled as one single piece. The rotors are in 4 parts. Each of the parts is centered inside the axial bearing, two radial bearings and motor as shown in the figure. The centering is approximate using shims as explained and shown in the previous

sections.

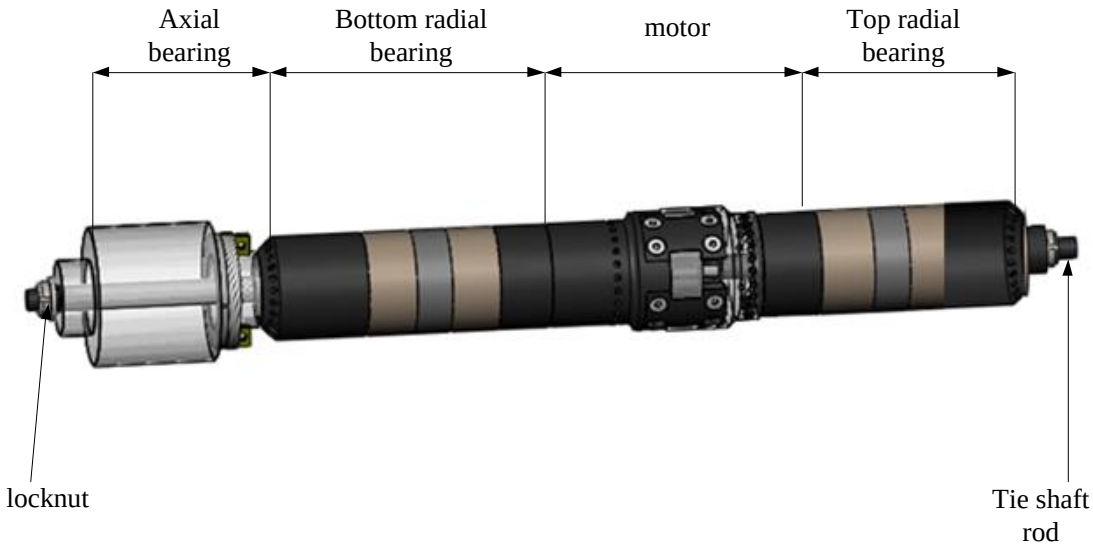

Figure 2-23 Complete rotor assembly

Each of the bearings and motor are assembled inside the test rig. Then a tie shaft rod (shown in the figure above) is used to tighten all the parts together so as to:

1. Achieve the interference fit between different sections
2. Tie all the four parts of the rotor together so that it would behave as one single rigid unit

Locknuts are used either sides to tie all the pieces together. The rotor pieces are provided with relief grooves at step locations to provide for proper mating.

In Figure 2-24 one could see the tightening of the bolts from the top so as to achieve the interference fit.

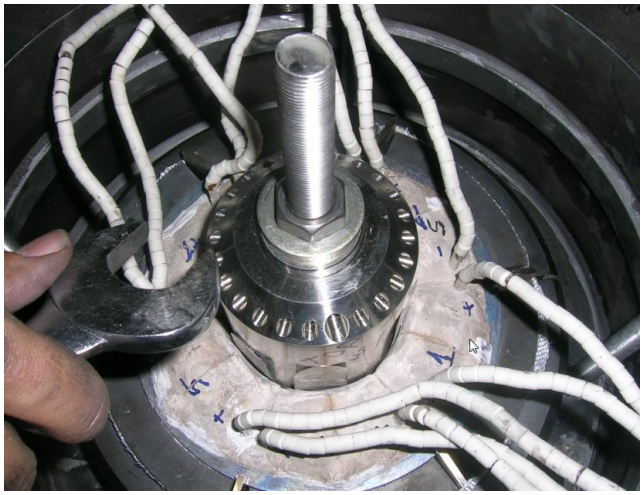

Figure 2-24 Tie shaft rod being used to achieve interference fit

Shown Figure 2-25 is the cut section view of the rotor. It has a stepped arrangement at different points to provide for the axial thrust and thereby to arrest axial movement.

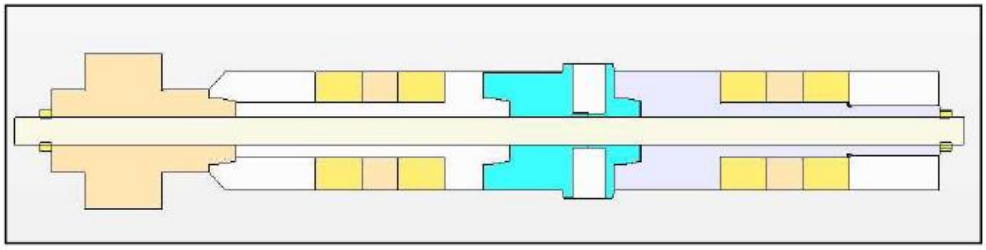

Figure 2-25 Cut section of rotor

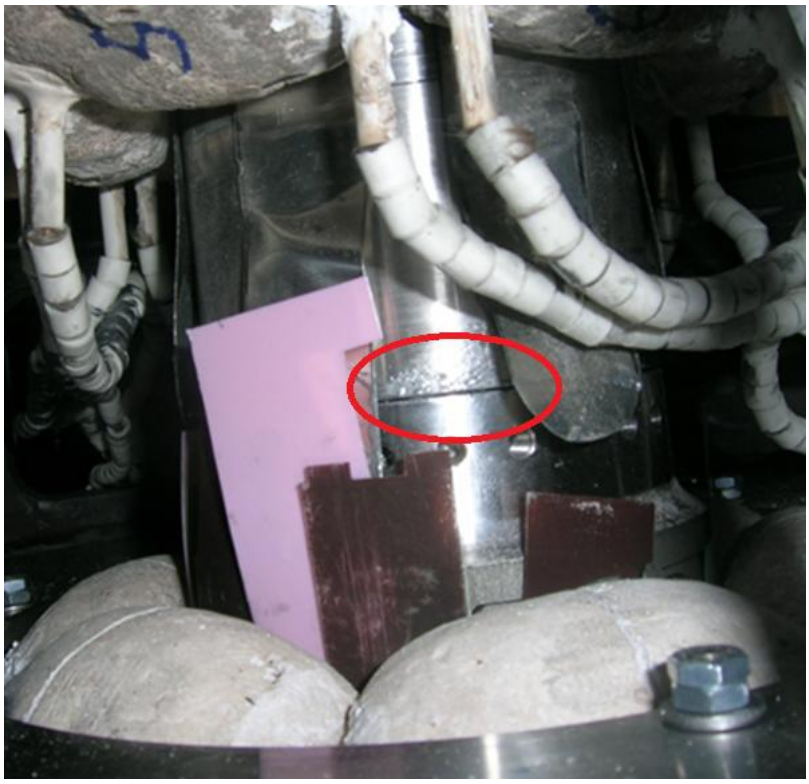

Figure 2-26 Interference fit between the top radial bearing and motor

Figure 2-26 shows the interference fit that was achieved between the radial bearing and motor. But the interference fit between the shaft pieces, between the bottom radial bearing and axial bearing has not been achieved yet. There is a gap of about 0.09 inches which is yet to be covered. The gap did not close even after applying huge torque by ratchet lever.

2.9 Control electronics

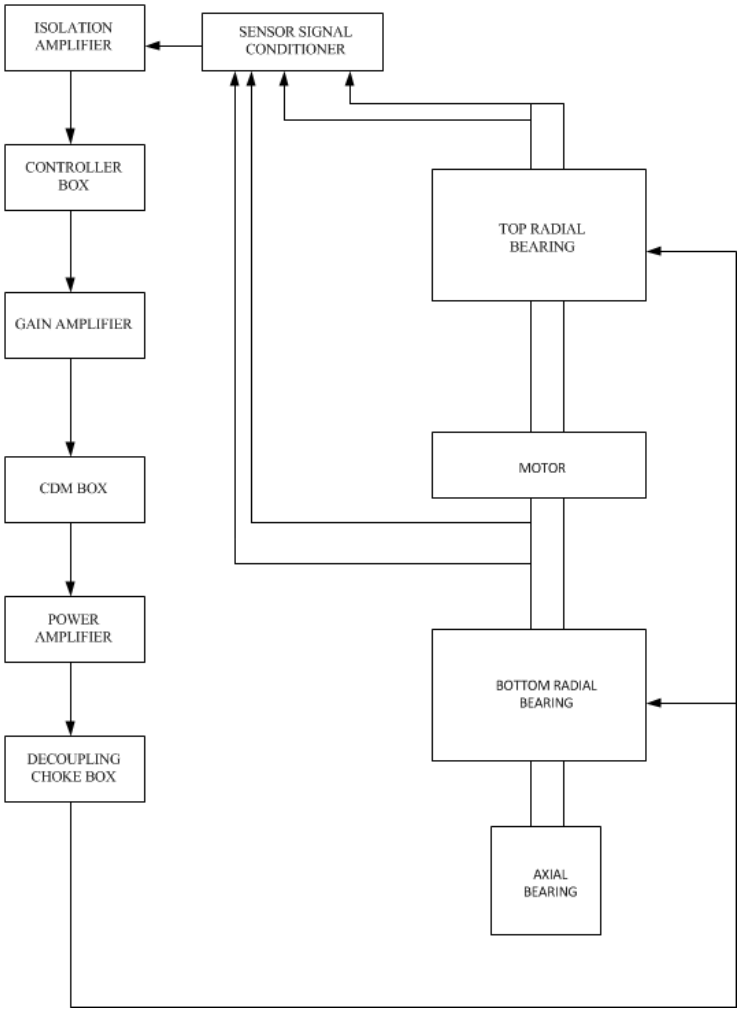

Figure 2-27 Control electronics to achieve feedback control

Figure 2-27 shows the control electronics used in the test rig for control.

The control electronics deal with maintaining the relative position of the rotor with respect to the bearings' axis. The bearings are assembled in a way that their positions are rigid so that no movement is allowed whatsoever.

The main component of the control electronics are the **sensors.** The sensors have very high resolution to the order of mils (one mil=0.001 inch). The magnetic bearing test rig uses five sensors for feedback control. Two sensors are at the top of the top radial bearing (at 90 degrees) and two sensors are above the bottom radial bearing (at 90 degrees and exactly below the corresponding sensor at the top). The axial sensor is installed under the tie shaft. The sensors are fixed rigidly to the setup by use of sensor holders. The sensors sense the location of the shaft continuously.

The sensors lead themselves into the sensor signal conditioner whose output is a mill volt reading based on the position of the sensor.

Isolation amplifiers provide electrical isolation and an electrical safety barrier. They protect the sensors from common mode voltages, which are potential differences between instrument ground and signal ground. Instruments without an isolation barrier that are applied in the presence of a common mode voltage allow ground currents to circulate, leading in the best case to a noisy representation of the rotor location predicted. The output of the isolation amplifiers is fed into the controller.

The **controller** compares the required position with the current position (uses the output from the five sensors) and outputs a voltage.

The single voltage from the controller (controller gain) is very small and it is amplified using a **gain amplifier.** The output of the gain amplifier is fed into the CDM box.

The **CDM box** (current distribution matrix box) divides the single voltage output received from the controller into six different output voltages (one each for each of the six coils in the radial bearings).

The output of the CDM box cannot be used since their outputs are very small. Hence they need to be amplified to an extent that can power up the coils. The output of the CDM box is therefore fed into the **power amplifiers**. The decoupling choke box is shown in Figure 2-28.

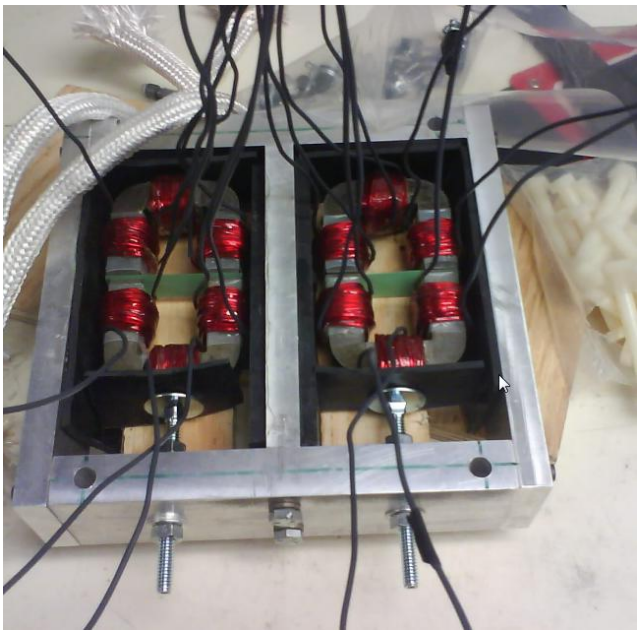

Figure 2-28 Decoupling choke box

Due to current passing through the coils mutual and self-inductances are developed. These inductances may affect the stability .To insure the stability of the circuit's operation a decoupling choke box is used, which negates these inductances.

The output of the decoupling choke box is fed to the bearings.

3. TESTING, CALIBRATION AND EXPERIMENTATION

3.1 Sensor testing and calibration

3.1.1 *Kaman sensors*

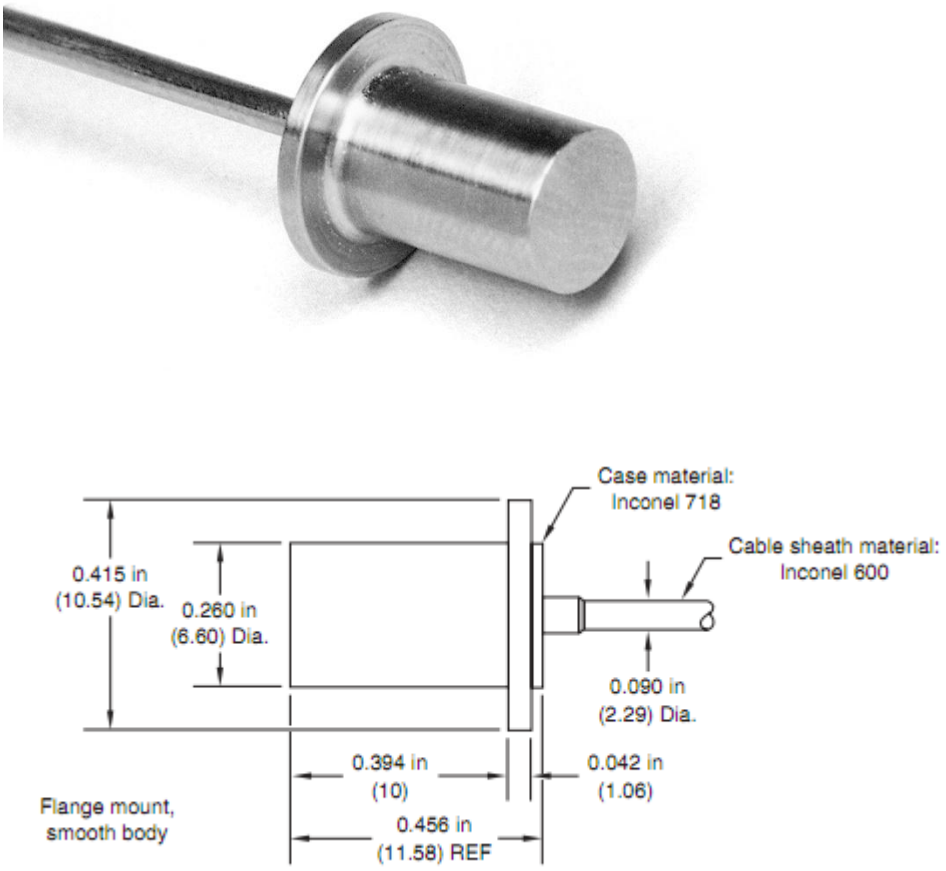

Figure 3-1 Kaman sensor-KD1925

The sensor and the dimensions are shown in Figure 3-1.

3.1.2 *Sensor specifications*

Make: Kaman

Model: KD1925

Operating distance range: 0 to 50 mils

Input: 120VAC

Output: 50mv/mil

Target material: non-magnetic materials

Operating temperature range: 77^{o}F to 1000 ^{o}F

Linear range: 0 to 50 mils

Parallelism error tolerance: +/- 2 degrees

Total cable length: 15 feet

Material: Inconel

Installation requirements:

- Target material should be at least 3 times diameter of sensor (about 1 inch).
- Target material should be non-magnetic.
- The face of the target and front face of the sensor should be parallel (error tolerance +/- 2 degrees).

- Target material with low resistivity preferred.
- Sensor should calibrated for linearity before installation.
- The sensor should be setup so that it always measures in the linear range of o to 50 mils.
- There should not be any metallic parts other than target within 1” of the sensor.
- The sensor cable’s output is connected to a signal conditioner.

3.1.3 *Signal conditioner*

The signal conditioner used is shown in Figure 3-2.

Figure 3-2 Kaman signal conditioner- KDM-8206 3U/84 HP

The model of the signal conditioner is model KDM-8206 3U/84 HP (KAMAN make)

The signal conditioner is used to process the output of the sensors and convert it into a calibrated voltage output.

3.1.4 *Sensor noise*

Sensor noise was one of the major concerns while setting up the sensors. Sensor noise is the variation in the sensor output for no variation in the target's displacement. The thumb rule for acceptable sensor noise was assumed as <50 mv (variation of less than 50 mv in the sensor output voltage which corresponds to 1 mil in the linear range).

It was understood that the noise in the output of the sensors could be caused by the following reasons:

1. Certain sensor-cable-sensor box slot combinations (it was understood that almost all Kaman sensors available with us had a certain combination of cable and slot which gave acceptable sensor noise.

2. Improper placement /installation of sensors. In other words the installation errors are beyond tolerance limits. The installation requirements are as follows:

    a. The surface of the sensor and the target need to be parallel.

    b. No metallic parts should be present within two diameters of the sensor.

    c. The axis of the sensor should cut the axis of the target.

The correct sensor-cable-slot combinations were selected for noise levels to be lesser than the tolerance limits. These combinations are shown in Table 3-1.

Table 3-1 Sensor, cable, slot combinations

sensor	**cable**	**slot**	**noise (maximum amplitude in mv)**	**equivalent in mils**
S0121249-01-06	S0121249-01-07	3	45	1.00
S0121249-01-02	S0121249-01-02	7	35	0.78
S0121249-04-01	S021249-01-04	2	38	0.84
S0121249-01-01	S0121249-01-03	5	40	0.89
S0121249-01-07	S0121249-01-08	4	40	0.89

3. Sensor holders not being rigid enough to dampen the vibrations:

   If the sensor holders vibrate they might introduce some noise into the system. So the sensors were installed in sensor holders and tested for noise levels by gently taping them and introducing some vibrations to simulate worst operating conditions for the sensor.

3.1.5 *Sensor calibration*

The objective was to determine the linear range of the sensors, so that the sensors could be setup so that the output is in the linear range. If the output is not in the linear range, the resulting displacement estimation from the voltage output of the sensor would be erroneous and thereby might result in an unstable system.

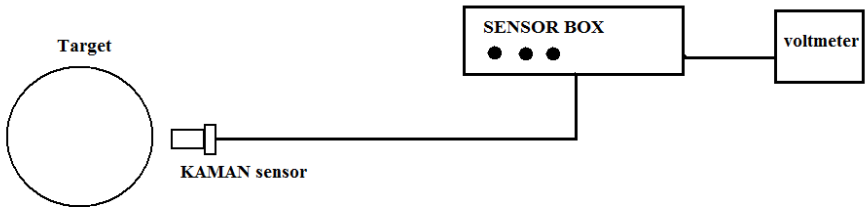

Figure 3-3 Setup for sensor calibration

The calibration procedure as advised by the manufacturer was followed. The setup used for calibration is shown in Figure 3-3. The sensor output was set to zero when the target was made to touch the sensor. The next step was 25 mils and 50 mils respectively. The necessary calibration procedure was undertaken (essentially screw adjustments on the sensor box to linearize the output. The final result was that all 5 sensors which were selected, were calibrated for linearity and the sensor outputs varied almost linearly from 0 to 2500mv (approximately outputting 50 mv per mil away from the target).

3.1.6 *Results*

Table 3-2 Sensor set 1: distance vs. voltage output

Distance in mils	Voltage in mv
0	2.23
9.5	416
26	1211
29.5	1412
38.5	1972

The results for sensor set 1 is given in Table 3-2.

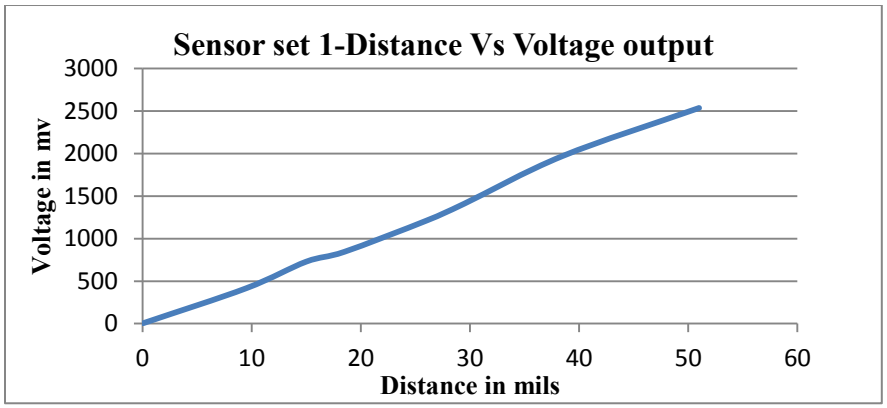

Figure 3-4 Sensor set 1: distance vs. voltage output

Figure 3-4 gives the response for sensor set 1.

Table 3-3 Sensor set 2: distance vs. voltage output

Distance in mils	Voltage in mv
0	15
9.5	470
15	745
29.5	1408
51	2533

The results for sensor set 2 is given in Figure 3-5.

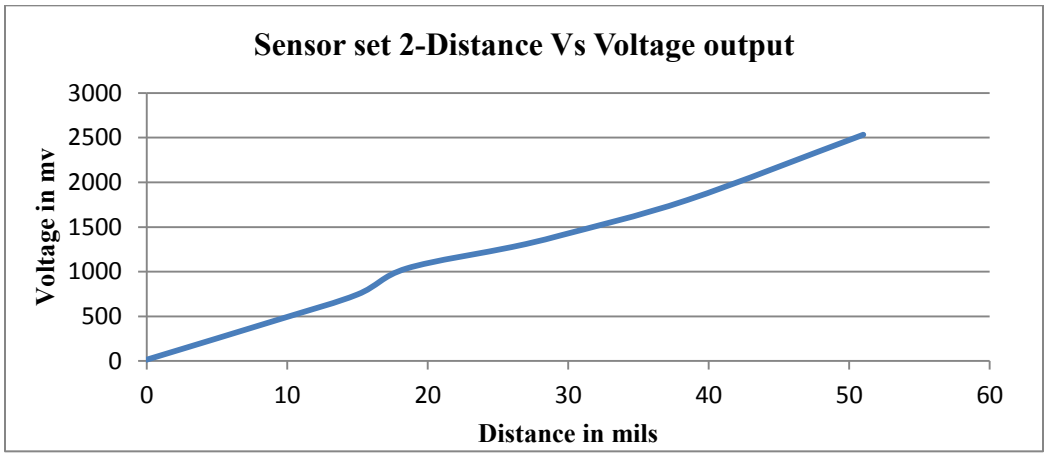

Figure 3-5 Sensor set 2: distance vs. voltage output

Table 3-4 Sensor set3: distance vs. voltage output

Distance in mils	Voltage in mv
0	4
9.5	493
15	747
29.5	1572
38.5	2012
51	2641

The results for sensor set3 is given in Figure 3-6.

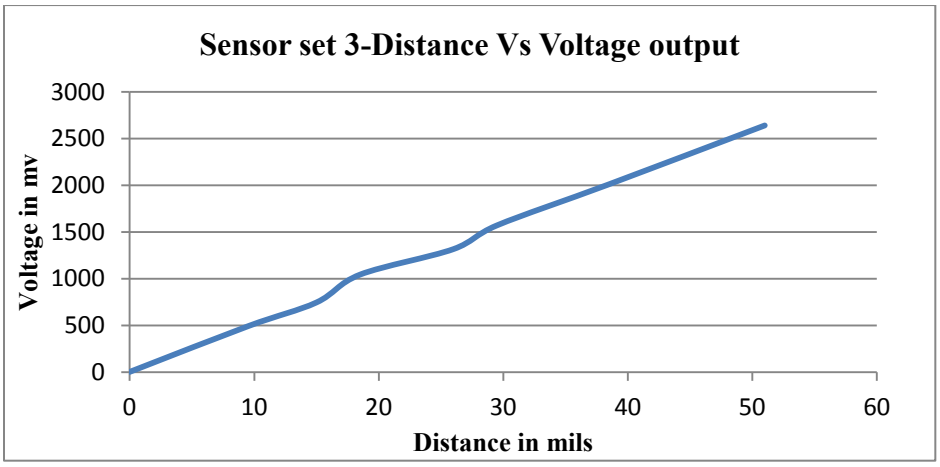

Figure 3-6 Sensor set 3: distance vs. voltage output

Table 3-5 Sensor set4: distance vs. voltage output

Distance in mils	Voltage in mv
0	-3.4
9.5	445
15	763
38.5	1823
51	2573

The results for sensor set4 is given in Figure 3-7.

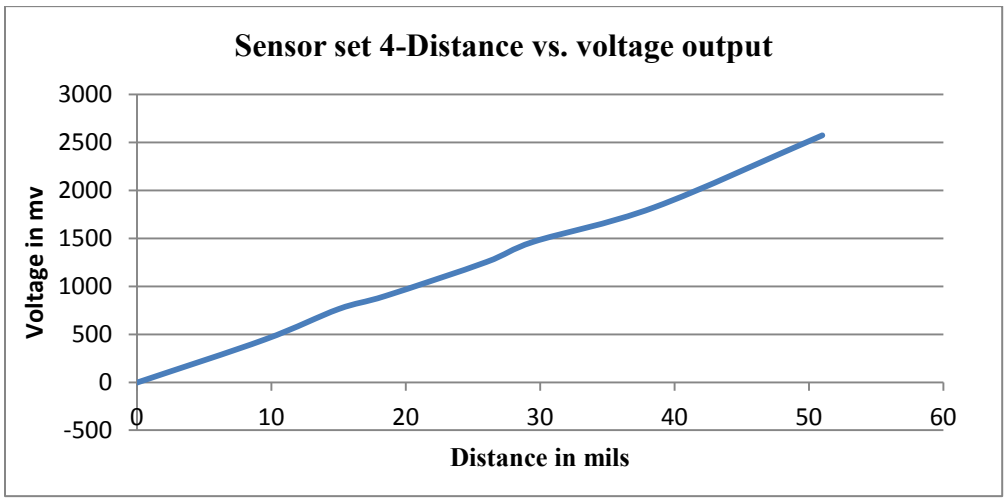

Figure 3-7 Sensor set 4: distance vs. voltage output

Table 3-6 Sensor set5: distance vs. voltage output

Distance in mils	Voltage in mv
0	-20
9.5	483
15	744
29.5	1453
38.5	1943
51	2593

The results for sensor set5 is given in Figure 3-8.

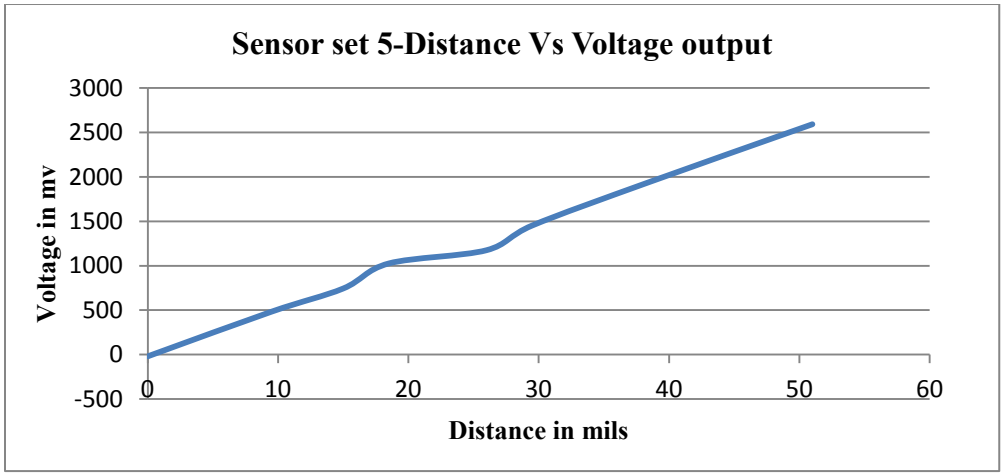

Figure 3-8 Sensor set 5: distance vs. voltage output

3.2 Determination of properties of Graphalloy

The properties of the Graphalloy material (used as solid lubricant) viz. coefficient of friction and Young's modulus is unknown. The above said properties and their change with respect to temperature is of very high interest in the case of usage of the graph alloy as solid lubricant.

We need to know how the Graphalloy will behave at high temperatures to predict the motion of the rotor at high temperatures. To be specific we need to know the coefficient of friction and Young's modulus determined at different temperatures. So a series of experiments were conducted to determine the following:

a. Measurement of coefficient of friction at room temperature.

b. Measurement of coefficient of friction at high temperature.

c. Measurement of Young's modulus at room temperature.

d. Measurement of Young's modulus at high temperature.

3.2.1 *Measurement of coefficient of friction at room temp*

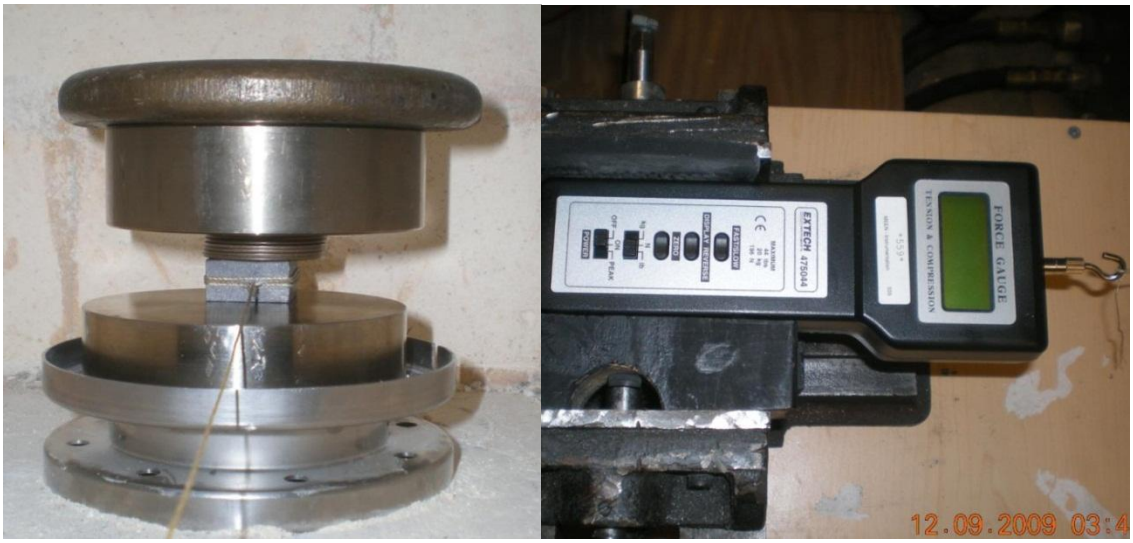

Figure 3-9 Setup to measure coefficient of friction at room temperature

The setup to measure coefficient of friction at room temperature is shown in Figure 3-9.

The rectangular bock of graph alloy was placed on a surface made of Inconel. The rectangular block placed on the Inconel surface was loaded on the up, by a known weight. This known weight is the normal force acting on the rectangular block of graph alloy. The rectangular block was tied with a thread, the other end tied to a high sensitivity force gauge.

The minimum reading of the force gauge is 0.01 lbs. The force gauge was held in movable vice. The vice is movable in one direction (in the direction of the thread), thus by moving the vice a tangential forced is applied to the rectangular block via a tension in the thread, which in turn is measured in real time by the force gauge.

Two readings on the force gauge were measured:

1. The force value which makes the block to start movement from rest.

2. The reading on the force gauge when the block is moving.

One could recall that the friction which acts on body at rest is called static friction; the one which acts when it's moving is called kinetic friction.

The value of static friction is more than that of kinetic friction. The use of a force gauge enabled the measurement of force required .A total of 17 readings were taken. They are tabulated below:

The average value of coefficient of static friction was determined to be 0.140 at room temperature.

Table 3-7 Coefficient of static friction of Graphalloy at room temperature

Static friction		
Normal force	**Tangential force**	**Coefficient of friction**
lbs.	lbs.	no unit
3.366	0.56	0.166
3.366	0.48	0.143
3.366	0.55	0.163
3.366	0.56	0.166
3.366	0.53	0.157
3.366	0.51	0.152
3.366	0.57	0.169
3.366	0.49	0.146
3.366	0.44	0.131
3.366	0.44	0.131
5.99	0.72	0.12
5.99	0.68	0.114
5.99	0.58	0.097
5.99	0.68	0.114
5.99	0.7	0.117

Table 3-7 tabulates the values observed to calculate the coefficient of friction. The

average value of coefficient of friction was 0.14; the standard deviation was 0.022.

Table 3-8 Coefficient of dynamic friction of Graphalloy at room temperature

Kinetic friction		
Normal force	**Tangential force**	**Coefficient of friction**
lbs.	lbs.	no unit
3.366	0.32	0.095
3.366	0.4	0.119
3.366	0.46	0.137
3.366	0.48	0.143
3.366	0.43	0.128
3.366	0.46	0.137
3.366	0.47	0.14
3.366	0.44	0.131
3.366	0.41	0.122
3.366	0.36	0.107
5.99	0.65	0.109
5.99	0.56	0.093
5.99	0.6	0.1
5.99	0.63	0.105

From Table 3-8 the average value of coefficient of dynamic friction was determined to be 0.117 at room temperature. All the coefficient of friction readings were close enough with a standard deviation of approximately15%. The average static coefficient of friction measured is 0.143 and average kinetic coefficient of friction measured is 0.119.

3.2.2 *Measurement of coefficient of friction Graphalloy at high temp*

The following setup was used to determine the coefficient of friction at high temperature:

Figure 3-10 Setup to measure coefficient of friction at high temperature

Figure 3-10 shows the setup that was used to determine coefficient of friction at high temperature.The same experiment described earlier to determine the coefficients of static and dynamics friction need to be repeated at higher temperature .The same setup with a known weight placed on the test Graphalloy piece is placed in a furnace; so as to conduct the experiment in a high temperature environment.

The high temperature wire is used instead of normal string so as to withstand high temperature to the order of 1000 ^{o}F. A thermocouple was used to measure the temperature of Graphalloy. The setup was kept inside the furnace and insulated from the outside environment using an insulating board.The experiment was repeated as before. The only change being the experiment was repeated at different temperature.

The coefficient of friction increases drastically from 750 ^{o}F to 1000 ^{o}F. The average value of coefficient of static friction at 1000 ^{o}F was determined to be around 0.47.

Table 3-9 Coefficient of static friction of Graphalloy at high temperature

Static friction			
Temperature	**Normal force**	**Tangential force**	**Coefficient of friction**
^{o}F	lbs.	lbs.	no unit
76	5.99	0.6	0.1
500	5.99	0.7	0.117
750	5.99	0.77	0.129
1000	5.99	2.81	**0.469**
1000	5.99	2.89	**0.482**
1000	5.99	2.85	**0.476**

Table 3-9 tabulates the values observed to determine the coefficient of static friction at high temperature. The value of coefficient of dynamic friction increases drastically from 750 to 1000 ^{o}F.

Table 3-10 Coefficient of kinetic friction of Graphalloy at high temperature

Kinetic friction			
Temperature	**Normal force**	**Tangential force**	**Coefficient of friction**
^{o}F	lbs.	lbs.	no unit
76	5.99	0.5	0.083
500	5.99	0.55	0.092
750	5.99	0.48	0.08
750	5.99	0.48	0.08
1000	5.99	1.3	0.217
1000	5.99	1.15	0.192
1000	5.99	1.15	0.192

Table 3-10 tabulates the values observed to determine the coefficient of dynamic friction at high temperature. The average value of coefficient of dynamic friction at 1000 ^{o}F was

determined to be 0.20.

3.2.3 *Determination of Young's modulus of Graphalloy at room temp*

3.2.3.1 Experimental setup

A special setup used to determine the Young's modulus of Graphalloy is shown in Figure 3-11. A beam of square cross section was used. The beam was loaded at different points with known weights. The deflection was measured at a known distance from one end of the beam. From the deflection the Young's modulus of the material was calculated.

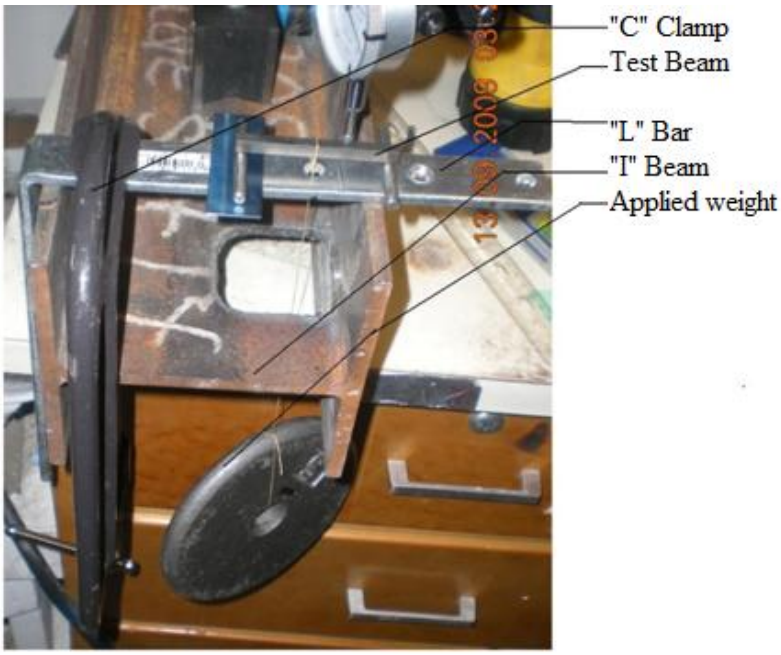

Figure 3-11 Setup to measure Young's modulus at room temperature

The Figure 3-12 shows the schematic setup for the experiment.

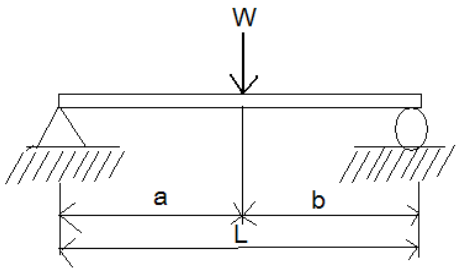

Figure 3-12 Schematic setup for the experiment

Figure 3-13 Setup to measure Young's modulus at room temperature

A heavy "I" beam was used as shown in Figure 3-13. The flanges of the "I" beam support an "L" beam. The L beam was preloaded using "C" clamp. This preloaded was to prevent any further deflection in the L beam. The graph alloy beam was placed and

positioned on the L beam. The string attached to the graph alloy beam which passes through an opening in the L beam and in the web of the "I" beam, was used to suspend weights from below and thereby load the graph alloy beam at different points. The deflection was measured using a dial indicator placed on the graph alloy beam.

3.2.3.2 Readings

Around fifteen readings were taken. The applied weight, length between supports and deflection were measured.

Table 3-11 Young's modulus of Graphalloy at room temperature

Weight (W)	**Beam Length (L)**	**Distance 'a'**	**Distance 'b'**	**Distance 'x' (from left)**	**Measured deflection (Δ)**	**Young's modulus**
lbs.	in	in	in	in	in	lbs./in^2
5.04	2.677	1.339	1.339	1.811	0.005	970,165
5.04	2.677	1.24	1.437	1.516	0.006	929,483
5.04	2.677	1.339	1.339	0.787	0.004	1,133,494
5.04	2.756	1.457	1.299	2.303	0.006	**508,854**
5.04	2.756	1.417	1.339	2.362	0.005	**532,626**
5.04	2.756	1.378	1.378	1.713	0.006	970,168

As shown in Table 3-11 the Young/s modulus was determined from these readings using standard formulae.

The readings in red were neglected because of too much variation from the rest of them. The average Young's modulus of Graphalloy at room temperature was found as 929,486 lbs. /in^2

3.2.4 *Determination of Young's modulus of Graphalloy at high temp*

The same experiment needs to be repeated at high temperature.

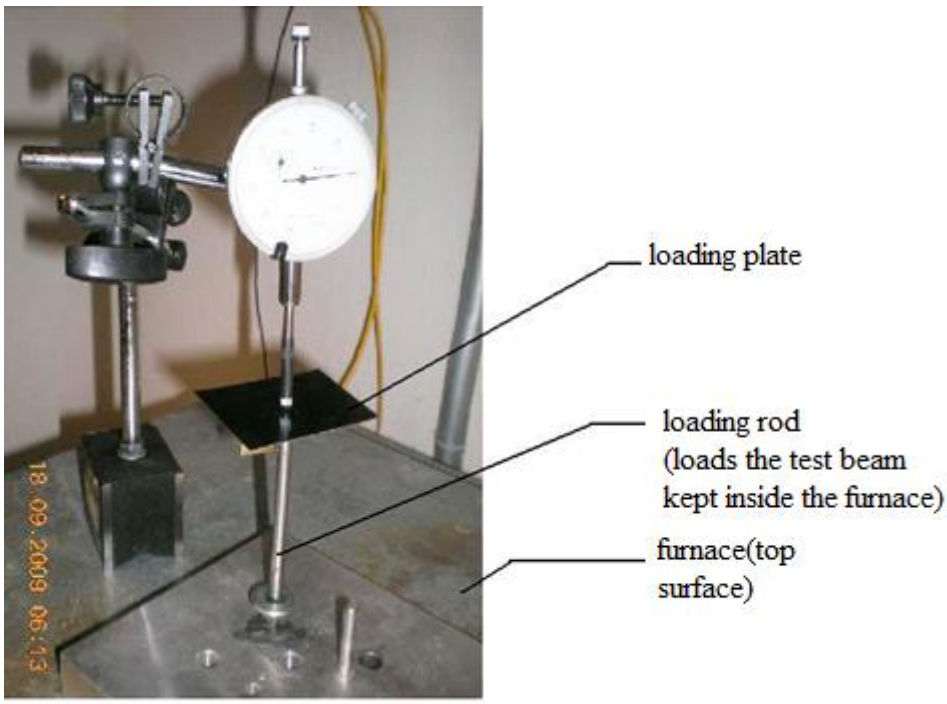

Figure 3-14 setup to measure Young's modulus at high temperature

The setup shown in Figure 3-14 established on top of the furnace was used in the experiment. The weights were kept on the loading plate, which extends to a loading rod. The loading rod extends into the inside of the furnace and loads the test specimen as shown in Figure 3-15.

Figure 3-15 Loading of test beam

A thermocouple-mill volt converter-voltmeter connection is used to indicate the temperature inside the furnace. Around fifteen readings were taken. The measurements include the following:

1. Weight applied.
2. Length between supports for the beam.
3. Point of application of weight.
4. Point at which deflection was measured.

5. Actual deflection.

Table 3-12 Young's modulus of Graphalloy at high temperature

Temperature	**Weight (W)**	**Beam Length (L)**	**Distance 'x' (from left)**	**Measured deflection (Δ)**	**Young's modulus**
^{o}F	lbs.	in	in	in	lbs./in^2
510	2.5	2.5	1.25	0.002	1,173,099
755	2.5	2.5	1.25	0.0025	938,479
770	5.04	2.5	1.25	0.0035	1,351,410
1000	2.5	2.5	1.25	0.0025	938,479
1004	5.04	2.5	1.25	0.0035	1,351,410

Table 3-12 we could find that the average value of Young's modulus of Graphalloy at 1000^{o}F is 1116477 lbs. /in^2 and the standard deviation is 202,991 or about 18%. There is no readily apparent increase/decrease in young's modulus over increase in temperature. (In the experiment Distance "a" and "b" are 1.25 m.)

3.3 Testing of the radial movement of plates

It was required to have enough radial movement of the stator plates, so that the rotor (inside the bearings and motor) after complete assembly could move freely enough and settle down wherever it had the tendency to get settled. This way we could ensure the rotor would be in a centered position. If we could recall, all rotor pieces inside the bearings were centered by using shims all around the rotor.

It was required to know the radial clearance of each of the plates in the cylinder. So the radial movement of each of the stator plates needed to be tested. In other words the radial clearance of each of the stator plates with the cylinder was tested. The test setup is shown in Figure 3-16.

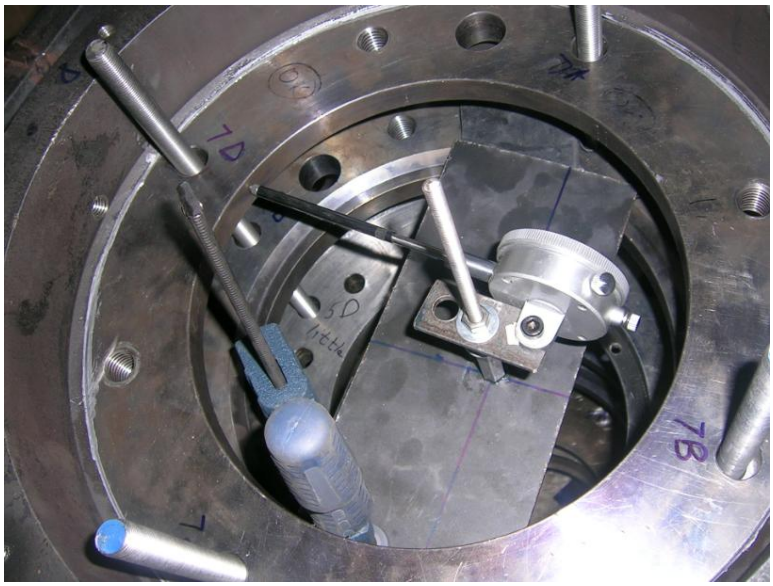

Figure 3-16 Setup for testing radial movement of plates

3.3.1 *Procedure for testing radial movement*

The following steps were followed:

1. Each of the stator plates were assembled inside the cylinder.
2. By using a special fixture a dial indicator was attached onto the plates (on the inside diameter surface-please refer figure for more clarity).
3. The following steps were performed:
    a. Step1: the plate was pushed on one side by using a radial set screw on side1. The scale of the dial indicator was changed to zero at this point.
    b. Step2: Now the set screw was loosened from side1 and the plate was pushed from the other side using the set screw from side 2. Now the net reading on the dial indicator would show the total radial movement of the stator plate.

The testing procedure is schematically shown in Figure 3-17.

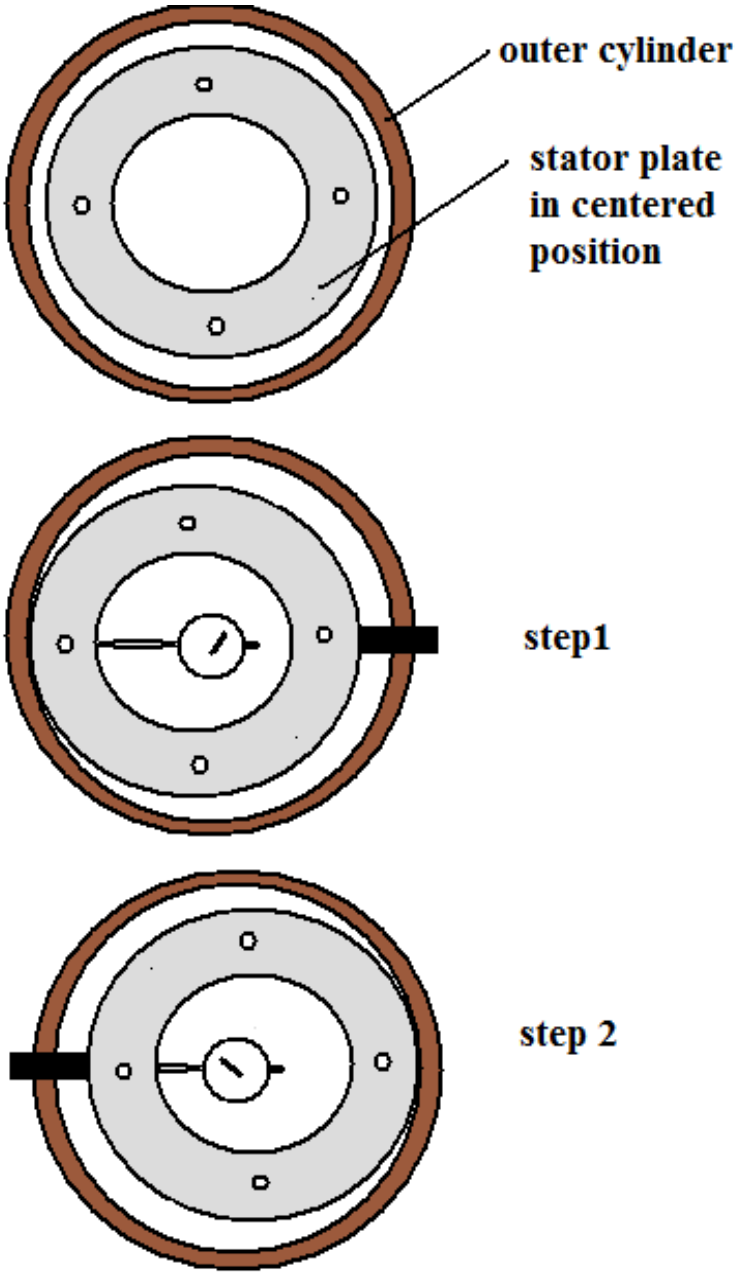

Figure 3-17 Procedure for testing radial movement of plates

The results are tabulated as below in Table 3-13.

Table 3-13 Radial movement of the stator plates

Plate no.	**Translation in x direction**	**Translation in y direction**
	mils	**mils**
7	5	6.5
6	6.5	4.5
5	7	6.5
4	5.5	5
3	11	7.5
2	3	5
1	3.5	5

It was decided that, to be surer of the centering of the rotor, some more radial clearance was to be sought after. So, all the stator plates were turned in the lathe, to have a total radial clearance of 40 mils. This way there would be more room for the rotor to move and get it centered.

3.4 Radial bearing magnetic flux density testing

Both the radial bearings were required to be tested for control and bias flux before the assembly of the bearings and motor were done. The bias flux is the flux due to the permanent magnets. In other words the bias flux is the flux present without the current flowing through the coils. The control flux is the flux with the current.

The flux was tested using a current meter. The tests showed a reversed polarity in one of the bearings. But they could be taken care of while making the connections at the control electronics end. The table below shows the control and bias flux measured for the top and bottom radial bearings.

Table 3-14 Magnetic flux test for top radial bearing-top plane

Pole	Plane	Voltage	No Current	With Current
		mv	Magnetic flux density (Tesla)	Magnetic flux density (Tesla)
1	Top	-515	-0.049	-0.063
2	Top	-515	-0.023	-0.027
3	Top	-496	-0.026	-0.033
4	Top	-465	-0.052	-0.065
5	Top	-518	-0.054	-0.072
6	Top	-491	-0.12	-0.155

Each bearings has two planes-top and bottom; each plane has 6 poles; in each of the planes the poles are numbered from 1 to 6 in sequence. Pole 1 of the top plane corresponds to pole 1 of the bottom plane and lies directly below it and so on.

The results for top radial bearing-top plane is shown in Table 3-14.

Table 3-15 Magnetic flux test for top radial bearing-bottom plane

Pole	Plane	Voltage	No Current	With Current
		mv	Magnetic flux density (Tesla)	Magnetic flux density (Tesla)
1	Bottom	-522	0.044	0.052
2	Bottom	-541	0.021	0.022
3	Bottom	-533	0.021	0.024
4	Bottom	-533	0.035	0.043
5	Bottom	-466	0.051	0.063
6	Bottom	-558	0.057	0.072

The results for top radial bearing-bottom plane is shown in Table 3-15

Table 3-16 Magnetic flux density test for bottom radial bearing-top plane

Pole	Plane	Voltage	No Current	With Current
		mv	Magnetic flux density (Tesla)	Magnetic flux density (Tesla)
1	Top	-459	-0.019	-0.022
2	Top	-464	-0.018	-0.015
2	Top	435	-0.021	-0.023
2	Top	440	-0.019	-0.022
2	Top	450	-0.021	-0.023
2	Top	380	-0.022	-0.025
2	Top	435	-0.021	-0.017
3	Top	-420	-0.037	-0.041
4	Top	-508	-0.155	-0.178
5	Top	-489	-0.036	-0.041
6	Top	-489	-0.04	-0.048

The results for bottom radial bearing - top plane is shown in Table 3-16. The values are in red because the coiling seem to be reversed in the top plane –second pole and it needs to be taken care of while connecting to the control electronics.

Table 3-17 Magnetic flux density test for bottom radial bearing-bottom plane

Pole	Plane	Voltage	No Current	With Current
		mv	Magnetic flux density (Tesla)	Magnetic flux density (Tesla)
1	Bottom	-503	0.022	0.025
2	Bottom	-492	0.014	0.017
3	Bottom	-473	0.033	0.04
4	Bottom	-454	0.043	0.055
5	Bottom	-512	0.064	0.078
6	Bottom	-487	0.028	0.032

The results for bottom radial bearing - bottom plane is shown in Table 3-17.

3.5 Insulation and heating test

To test the magnetic bearing test rig at 1000 ^{o}F, the whole test rig needs to be heated up to about 1000 ^{o}F. Three band heaters and two radiant heaters were used to heat the test rig. However, the target temperature of 1000 ^{o}F was achieved even without operating the radiant heaters.

The band heaters enclose the outer cylinder (in a concentric fashion to the outer periphery of the low carbon steel cylinder. Since the outer cylinder has only point

contact the conduction heat losses are greatly reduced. To reduce the heat losses by Zircar sheets play a big role.

The test rig was properly insulated by using Zircar sheets Zircar Alumina silica type ceramic (Eco-1200A).

Figure 3-18 Outer cylinder with band heaters assembled on to them

The outer cylinder with Zircar insulation is as shown in Figure 3-18. The heating of the band and radiant heaters are controlled by using a controller [3].

Figure 3-19 Outer cylinder with radiant heaters and insulation sheets

Apart from Zircar sheets other high temperature insulation material were also used to achieve 1000^{o}F target temperature. This is shown in Figure 3-19. The target temperature was measured using thermocouples placed at strategic locations inside the outer cylinder. The heater controller consists of the Watlow CLS-216 controller and a number of solid state relays to provide for the switching control of the band and radiant heaters.

The whole test setup when heated emits unpleasant smells. This called for installation of exhaust piping. The test setup was insulated from the outside environment by fabricating an enclosure covered with transparent covers. Exhaust piping was installed exclusively for this setup. Blowers installed outside the lab blew out the unpleasant gases from the inside of the enclosure to the outside atmosphere.

Figure 3-20 Enclosure with exhaust piping

The enclosure with exhaust piping is as shown in Figure 3-20.

4. DESIGN AND FABRICATION OF ACCESSORIES

4.1 Sensor holders

The position sensors (Kaman make) are capable of operating at very high temperatures. They are very expensive and the output wires are sensitive to temperature. Efficient functioning of the sensors is extremely important for proper feedback from the controllers. So a need for a physical structure to hold the sensors strategically in place and protect them was imminent.

4.1.1 *Objectives/ design constraints*

- Should hold the sensors in proper alignment –facing the shaft.
- The axis of the shaft needs to cut the axis of the sensor at 90 degrees.
- The front face of the sensor needs to be parallel to the face of the shaft (+/- 2 degrees).
- The sensor holders should be able to withstand the high temperatures to the tune of 1200 ^{o}F and preferably nonmagnetic.
- Should provide a way to hold the sensors in place without negligible vibration/movement.
- Should provide a way to adjust the sensors position.

- A strategic location needs to be picked so that there will be no metal parts in the vicinity of the sensing portion (about two diameters of the sensor).
- The sensor holders need to be mounted on the outer cylinder.

The sensor holders fit into the outer housing and target the shaft. The sensor holders are attached to stainless steel mounts, called attachment plates, which have milled slots in them. Nuts, bolts and washers can be used into the holes drilled into the cylinder to fix the sensor holders firmly in place. The position of the sensors can be adjusted by using the slots. Two sensor holders were designed.

4.1.2 *Bottom sensor holder*

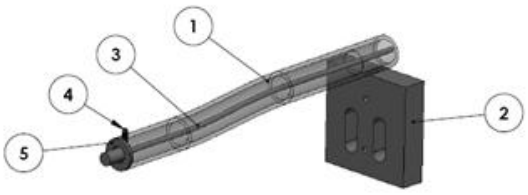

Item no	Description
1	Tube-bottom
2	Attachment plate-bottom
3	sensor
4	4-40 set screw
5	washer

Figure 4-1 Sensor holder-bottom

The bottom sensor holder is shown in Figure 4-1.

4.1.3 *Top sensor holder*

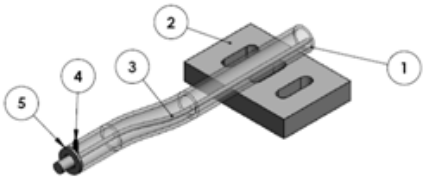

Item no	Description
1	Tube-Top
2	Attachment plate-Top
3	sensor
4	4-40 set screw
5	washer

Figure 4-2 Sensor holder-top

The bottom sensor holder is shown in Figure 4-2.

4.1.4 *Axial sensor holder*

The axial sensor holder is fit to the bottom of the test rig exactly under the tie shaft rod, so that the axial position can be sensed. The axial sensor holder is fabricated out of bent stainless steel plates.

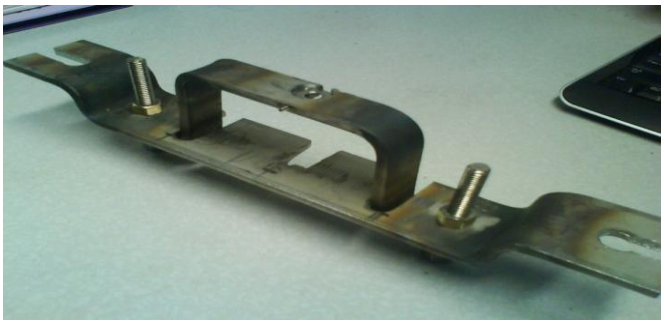

Figure 4-3 Axial sensor holder

The axial sensor holder is shown in Figure 4-3.

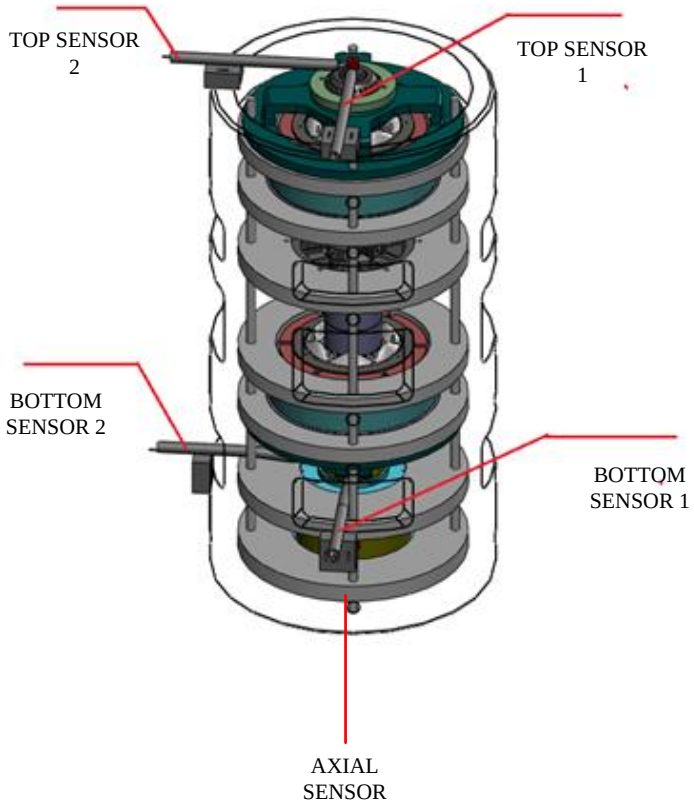

Figure 4-4 Sensor positions

The sensor holders were mounted onto the outer cylinder as shown in Figure 4-4.

4.2 Design of press fit for Graphalloy catcher bearings

The press fit is between the Graphalloy and Graphalloy casing. The rotor comes into contact with the Graphalloy thereby protecting the bearings. The Graphalloy is subject to wear as the rotor runs. If the Graphalloy wears the net radial clearance between the Graphalloy and rotor could decrease. So it was decided to have a tapered press fit for Graphalloy. The idea is to turn the Graphalloy casing cap to move the Graphalloy inside (thereby drive the tapered Graphalloy piece inside and increase the interference) so as to maintain the radial clearance between the rotor and Graphalloy.

Also the press fit helps the Graphalloy to be kept in place when the rotor runs at high speed. Also the Graphalloy tends to lose interference at high temperature (coefficient of thermal expansion of Graphalloy is 3.5*10^-6 in/in/ ^{o}F which is less than that of Inconel 7*10^-6 in/in/ ^{o}F). So there needs to be a way to increase interference at high temperatures by moving the cap in. The Graphalloy inside the Inconel Graphalloy casing is as shown in Figure 4-5.

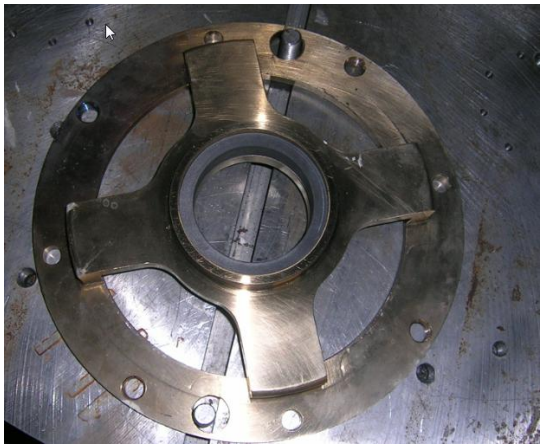

Figure 4-5 Graphalloy inside catcher bearing plate

4.3 Design constraints

The press fit should exist at high temperatures (1000 ^{o}F maximum). The stress on Graphalloy should be optimal (Graphalloy can withstand a maximum compressive stress of 20000 psi and tensile stress of 4000 psi). The graph alloy casing (made of Inconel) was not originally designed for a tapered press fit. So a design modification to include a tapered portion was included. The assembly procedure is as shown in Figure 4-6.

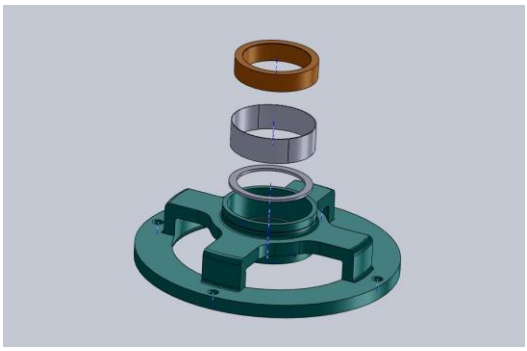

Figure 4-6 Assembly of Graphalloy catcher bearing

The interference in the tapered press fit is as shown in Figure 4-7.

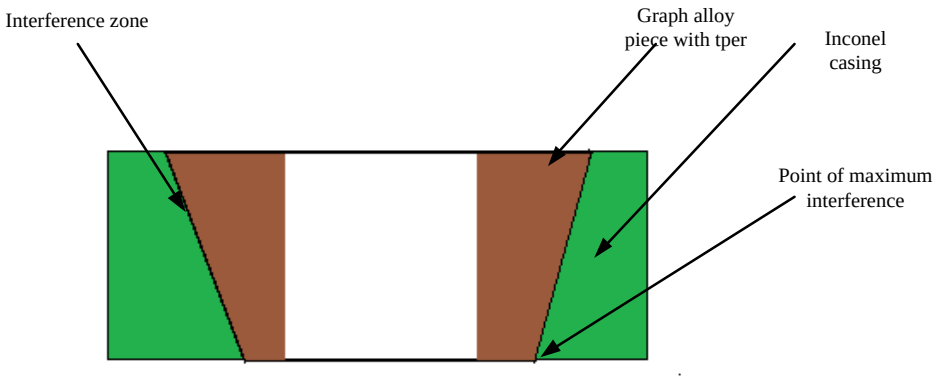

Figure 4-7 Interference of tapered press fit inside catcher bearings

4.3.1 *Design calculations*

4.3.1.1 Objectives

1. The interference should exist at 1000 ^{o}F (considering the fact that the Graphalloy expands at a lesser rate than that of the Inconel casing).

2. The interference is maximum at room temperature; in other words stresses on Graphalloy will be the maximum at room temperature; these stresses should be well below the allowable stresses for Graphalloy. The maximum allowable compressive stress for Graphalloy is 20,000 psi and allowable tensile stress is 4,000 psi.

Maximum diametric Interference at 1000 ^{o}F is given by

$$\delta_{1000} = d_i (1+ 1000 \text{ X } \alpha_i) - d_o (1+ 1000 \text{ X } \alpha_0)$$

δ_{1000}- maximum diametric interference at 1000 ^oF along the interference zone

d_o – diameter of outer member (Inconel) at the point of maximum interference

d_i – diameter of inner member(Graphalloy) at the point of maximum interference

α_i – coefficient of thermal expansion of inner member (Graphalloy) ($3.5 \text{ X } 10^{-6}$ in/in/ ^oF)

α_0 – coefficient of thermal expansion of outer member (Inconel) ($7 \text{ X } 10^{-6}$ in/in/ ^oF)

It was decided arbitrarily to have a maximum interference of about 12.5 mils at 1000 ^oF.

It was also decided to have an arbitrary value of 3.935 in for d_i.

Inserting the above values in the equation gives a value of 3.909 for d_o.

This gives an initial diametric interference **δ =0.026** in at room temperature.

The stress values for this arbitrary dimensions was checked as below:

The pressure ‘p’ acting on the mating surface is given by

$$\frac{\delta}{d\left\{\frac{1}{E_0}\left[\frac{(d_0^2+d^2)}{(d_0^2-d^2)}+\upsilon_0\right]+\frac{1}{E_i}\left[\frac{(d^2+d_i^2)}{(d^2-d_i^2)}-\upsilon_i\right]\right\}}$$

δ – Diametric interference at the point of maximum interference (0.026 in)

E_o – young's modulus of outer member (Inconel) (30 X 10^6 psi)

E_i – young's modulus of inner member (Graphalloy) (1,116,477 psi-determined experimentally)

V_o –Poisson's ratio of outer member (Inconel) (0.3)

V_i –Poisson's ratio of inner member (Graphalloy) (0.3)

The pressure acting on the mating surface was calculated as **23.68 psi.**

The tensile stress acting on the outer member is given by:

$$\sigma_{t_o} = p * \left[\frac{(d_0^2 + d^2)}{(d_0^2 - d^2)}\right]$$

This was calculated as **39.76 psi** which is within allowable limits.

The tensile stress acting on the inner member is given by:

$$\sigma_{t_i} = -p * \frac{(d^2 + d_i^2)}{(d^2 - d_i^2)}$$

This was calculated as **7135 psi** which is within allowable limits. The results are shown in Table 4-1.

Table 4-1 Interference vs. force at interface for Graphalloy tapered press fit

Interference in mils	Force in pounds
0.4	109.43
2.6	711.47
4.8	1313.87
7	1916.63
13.6	3727.25
15.8	4331.7
26	7138.38

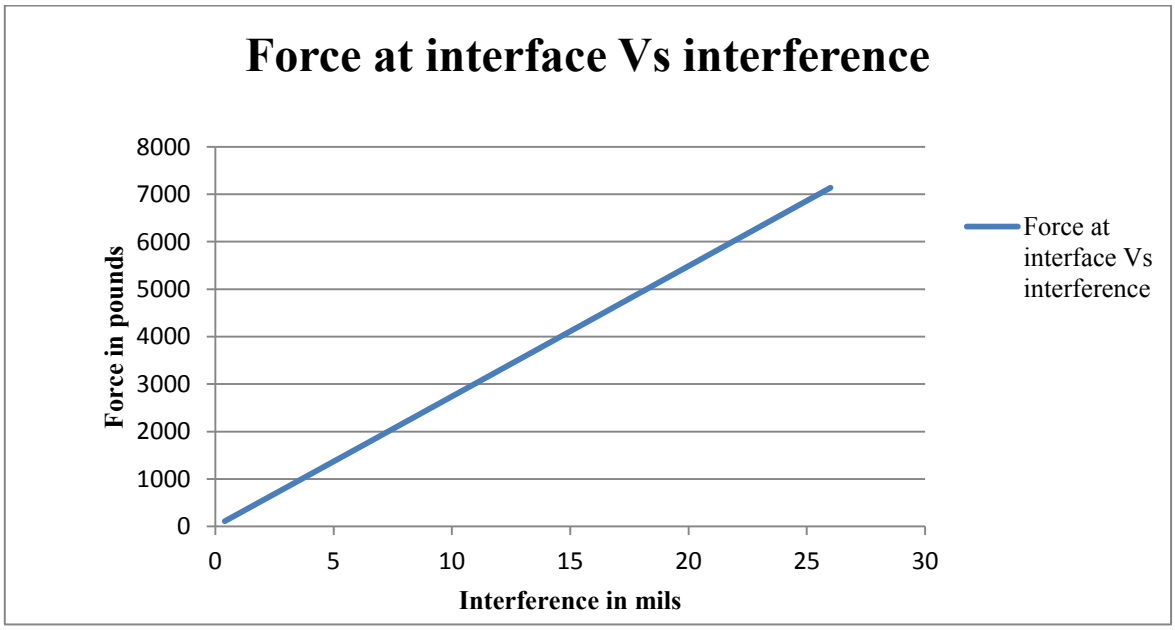

Figure 4-8 Force at interface vs. interference for catcher bearings

Figure 4-8 shows the force at interface values for different values of interference.

The other dimensions of the press fit like the taper angle were decided arbitrarily, since the worst scenarios have been taken care of.

4.3.2 *Problems with maintaining interference at high temperature*

The catcher bearing system was designed to have interference, even at higher temperature (at least 1000 ^{o}F). The Graphalloy is supposed to have interference of 12.5 mils at 1000 ^{o}F.

It was decided to test this out before the catcher bearing was installed in the assembly.

Under controlled heating conditions inside a furnace (where the temperature was measured by using a thermocouple) the interference was examined at different temperatures. The assembly lost all the 26 mil interference at a temperature of 850 ^{o}F.

The reason why the Graphalloy lost all its interference is that the Inconel casing was expanding at a faster rate than predicted. The reason why the Inconel casing was expanding more than predicted rate has not been understood even after sufficient efforts. This is one area where efforts are required in the future.

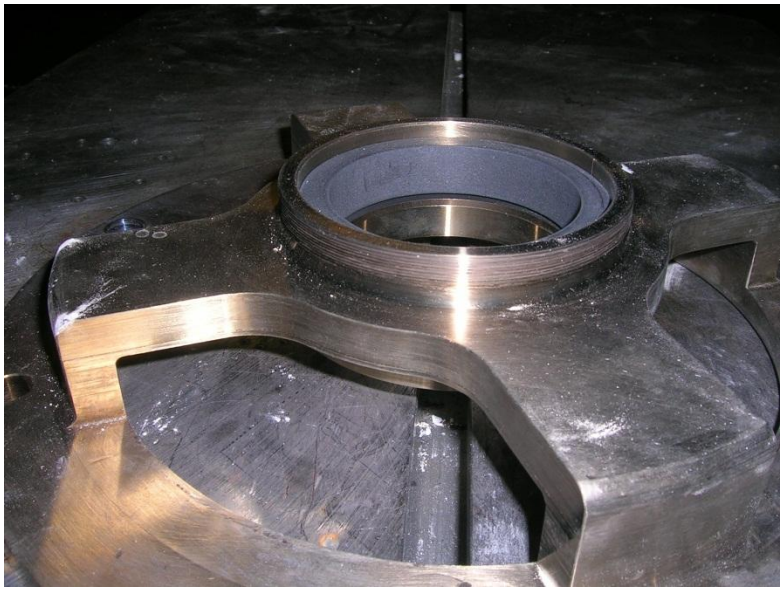

Figure 4-9 Graphalloy heating test

Figure 4-9 shows the catcher bearing assembly with Graphalloy after the heating test.

5. ASSEMBLY

5.1 Introduction

To achieve full system assembly, first each of the following four individual subassemblies needs to be assembled and setup. They are:

1. Axial bearing and the corresponding rotor part.
2. Bottom radial bearing and the corresponding rotor part.
3. Motor and the corresponding rotor part.
4. Top radial bearing and the corresponding rotor part.

They were assembled by centering the corresponding rotor part by the use of shims all around. This part was done by students who previously worked on the project in an arduous and time consuming process by use of special fixtures.

Initially the bearing/motor sub-assemblies were without stator plates attached to them. The subassembly needs to sit/get aligned on a bottom stator plate so that the subassembly could be lifted by the bottom stator plate and then assembled into the rig.

We had to be careful while lifting the bearing and aligning it with the bottom stator plate because; the rotor piece is centered loosely inside the bearing with shims around. If the rotor is not supported while lifting, it might fall off due to its self-weight. So a special fixture was fabricated to lift the bearing as well as to support the centered rotor at the same time.

The sub-assemblies were assembled into the outer cylinder in the same order from 1 to 4 mentioned above. The assembly process had the following operations:

1. Setting up the bearing/motor on the work table.
2. Lifting the bearing/motor using the special fixture and hydraulic lift.
3. Aligning the bearing/motor onto the bottom stator plate.
4. Lifting the motor/bearing by the bottom stator plate using the hydraulic lift.
5. Assembling the motor/bearing into the test rig.
6. Centering of the stator plates.

5.2 STEP 1: Setting up the bearing/motor subassembly

We need to setup the bearing/motor sub assembly so that the subassembly could be lifted and aligned onto the bottom catcher bearing. The setting up process is as shown in Figure 5-1. Two vertical wooden blocks support a central rod (removable) that go through the bearing-rotor subassembly. A wooden block in the middle (properly supported and belted onto a strong and rigid table) transfers the weight of the sub assembly to the table and to the ground. The subassembly was also belted centrally for extra support.

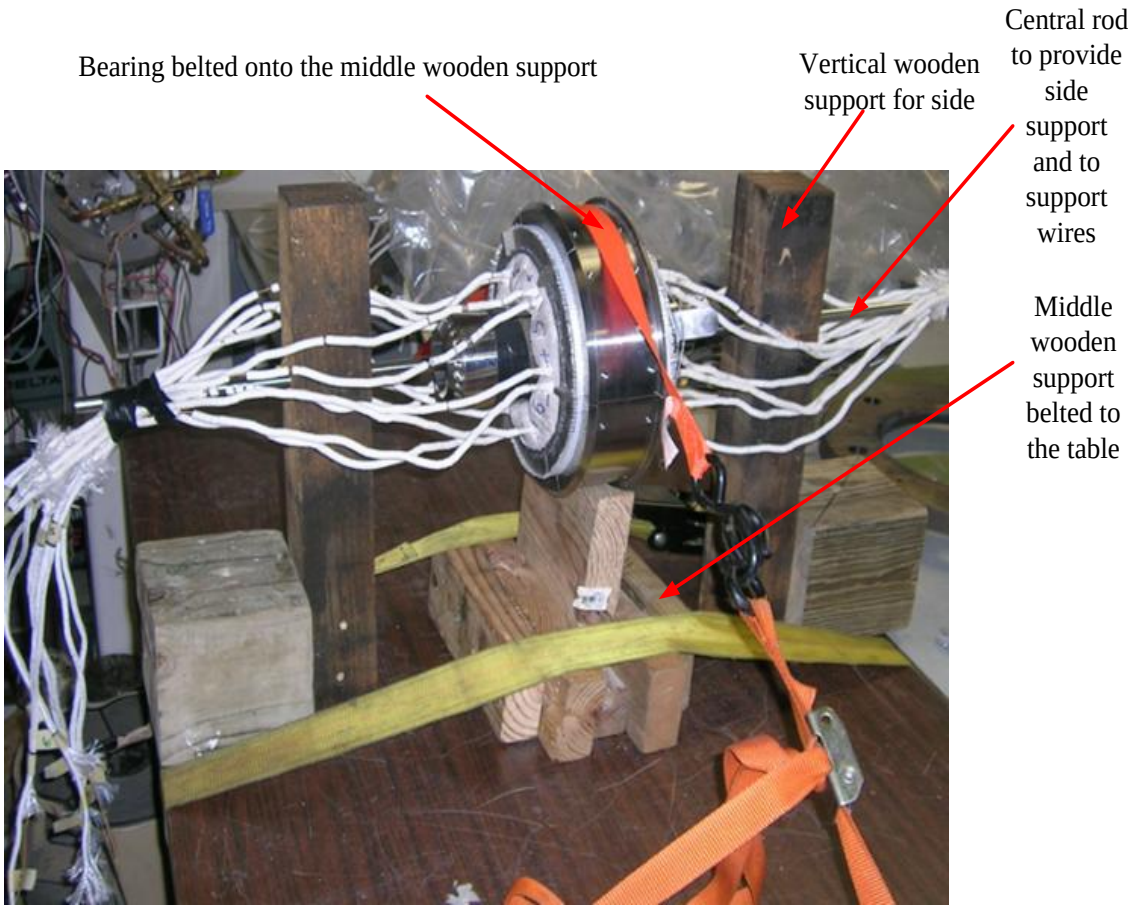

Figure 5-1 Setting up the bearing for assembly

5.3 STEP 2: Lifting the bearing/motor using the special fixture and lift

A special fixture was used to lift the bearing and support the centered rotor piece inside the bearing at the same time. If the rotor's weight (rotor being held in the center with shims around and not supported in any other way) is not supported then the rotor will fall off while trying to lift the bearing and assemble it. So a special fixture with cross type arrangement was fabricated as shown in Figure 5-2.

Figure 5-2 Cross fixture for assembly

The crosses have all thread rods at their ends. These all thread rods are tightened with nuts and washers on either side so that they are rigid. The fixture has a central eye bolt so that it could be lifted.

Now one of the vertical wooden supports was removed from one side. The special fixture was assembled onto the bearing as shown in Figure 5-3. One could see that the all thread rods go and embrace the outer surface area of the bearing. The all thread rods are held in place by a hose clamp.

Figure 5-3 Mounting cross-fixture onto the bearing

Another hose clamp mounted on the center rotor piece is tied with a metal wire on to the cross so that the rotor will not fall while lifting. A hydraulic lift was used to lift the assembly. The hook of the hydraulic lift was inserted into the eye of the fixture to lift it.

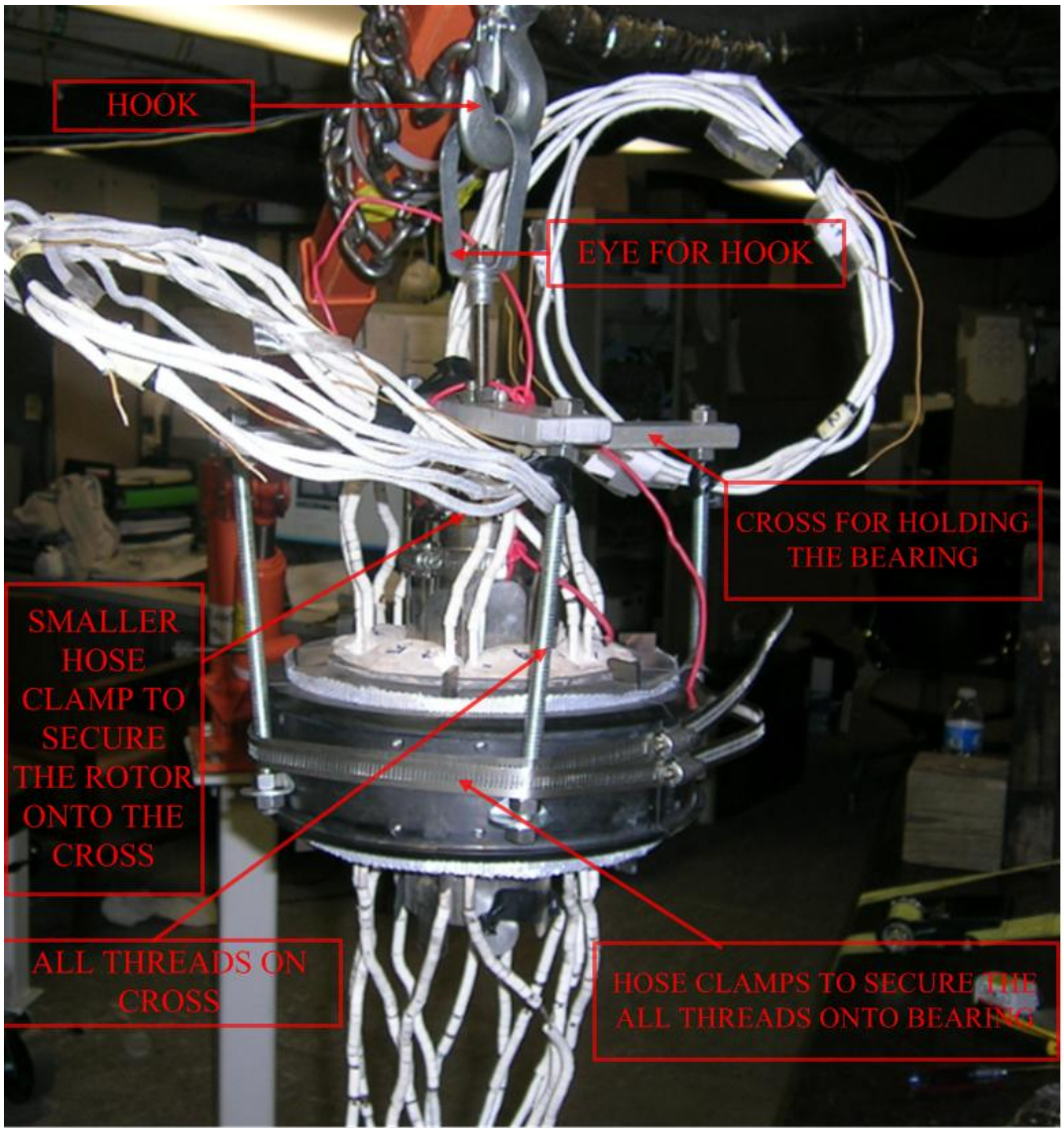

Figure 5-4 Lifting of bearing using cross fixture

A complete pictorial description of the lifting process is as shown in Figure 5-4.

5.4 STEP 3: Aligning the bearing/motor onto the bottom stator plate

Figure 5-5 Aligning the bearing onto stator plate-1

Now the bearing stator plate which goes in the bottom is setup on a rigid table. It is made to stand with the help of four all thread rods screwed into the drilled and tapped holes in the plate.

The bearing while being lifted as shown in Figure 5-5 should be treated with extreme sensitivity and the high temperature wires coming out of the bearings should be properly

supported. The hydraulic lift's lever is very sensitive and should be turned with extreme care. There should be at least 3 people to do this operation. Now the bearing should be raised and lowered onto the stator plate so that the chamfer on the bottom of the bearing and that on the bearing plate match with each other.

Figure 5-6 Aligning the bearing onto stator plate-2

The pictures showed in Figure 5-6 show the alignment of the chamfer lips so that the bearing sits perfectly onto the bottom stator plate, so that the bearing is level.

5.5 STEP 4: Lifting the motor/bearing by the bottom stator plate

Now the bearing is ready to be assembled inside the test rig as shown in Figure 5-7. A cross bar (square cross section) with all thread rods at the ends and an eyebolt in the center is used to lift the bearing. The hydraulic lift is used to lift the bearing. The cross fixture is still in place, supporting the rotor.

Hydraulic lift is slowly moved into the test rig enclosure for assembly into the rig.

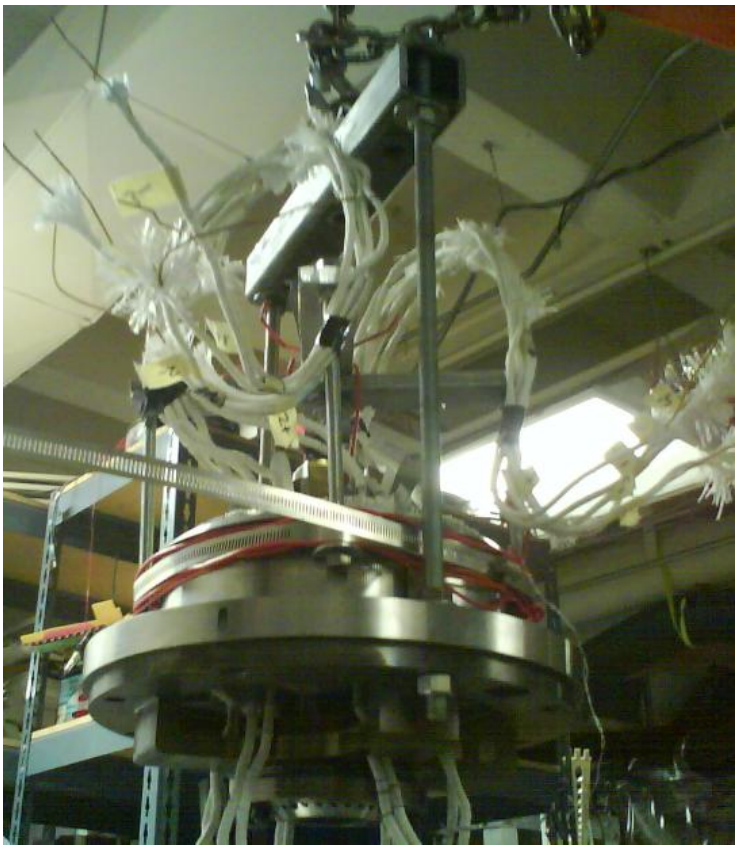

Figure 5-7 Lifting the bearing by the bottom stator plate

5.6 STEP 5: Assembling the motor/bearing into the test rig

A couple of standard mechanical devices (winch and pulley) are used to finally assemble the bearing inside the rig. The pulley and winch installed inside the test rig enclosure is as shown below shown in Figure 5-8.

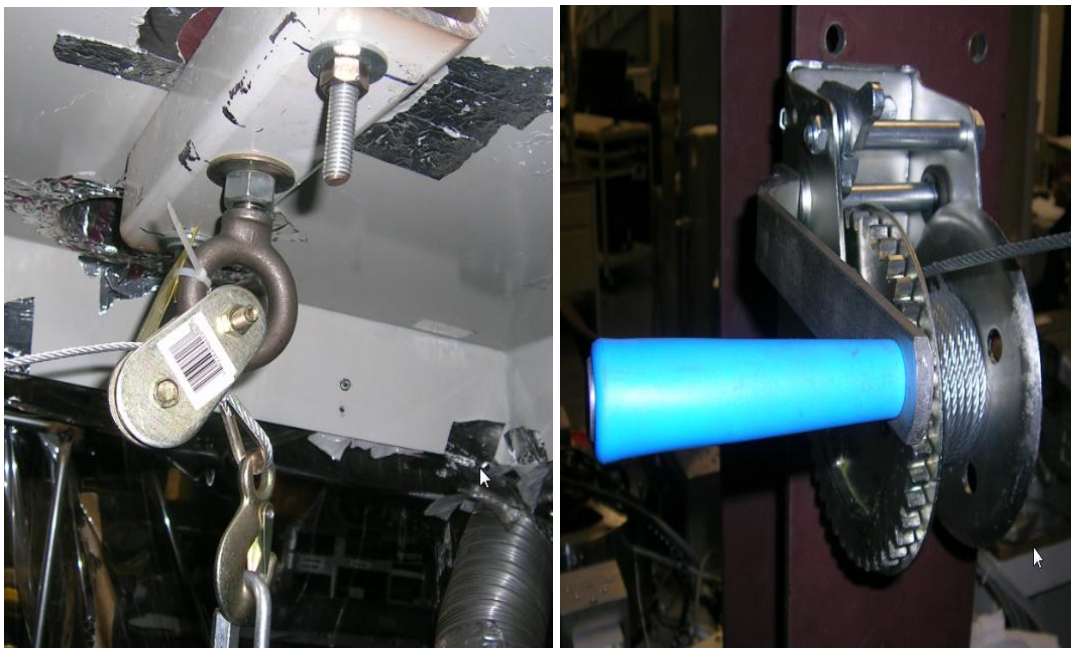

Figure 5-8 Pulley and winch used for assembly

As the bearing is brought inside the test rig enclosure the hook at one end of the winch rope is assembled onto the eye bolt of the square cross bar. Now the winch is operated slowly thereby lowering the bearing into the outer cylinder as shown in Figure 5-9. At least three people are required to achieve proper and safe assembly. The wires need to be pulled carefully and slowly out of the access windows of the cylinder.

Figure 5-9 Assembly of the bearing into the rig

After the assembly the view from the top is as shown in Figure 5-10

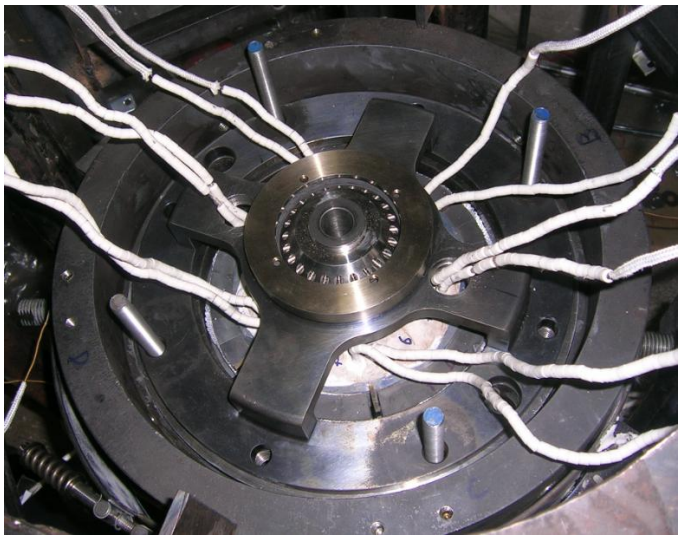

Figure 5-10 After assembly-top view

5.7 STEP 6: Centering of stator plates

The stator plates need to be centered to make sure that the rotor is in the center. It is known that the individual rotor pieces are centered using shims around in the corresponding bearing/motor (except for axial bearing). Now the following procedure needs to be followed to ensure that each of the bearing units /motor unit is positioned to allow for a centered rotor assembly.

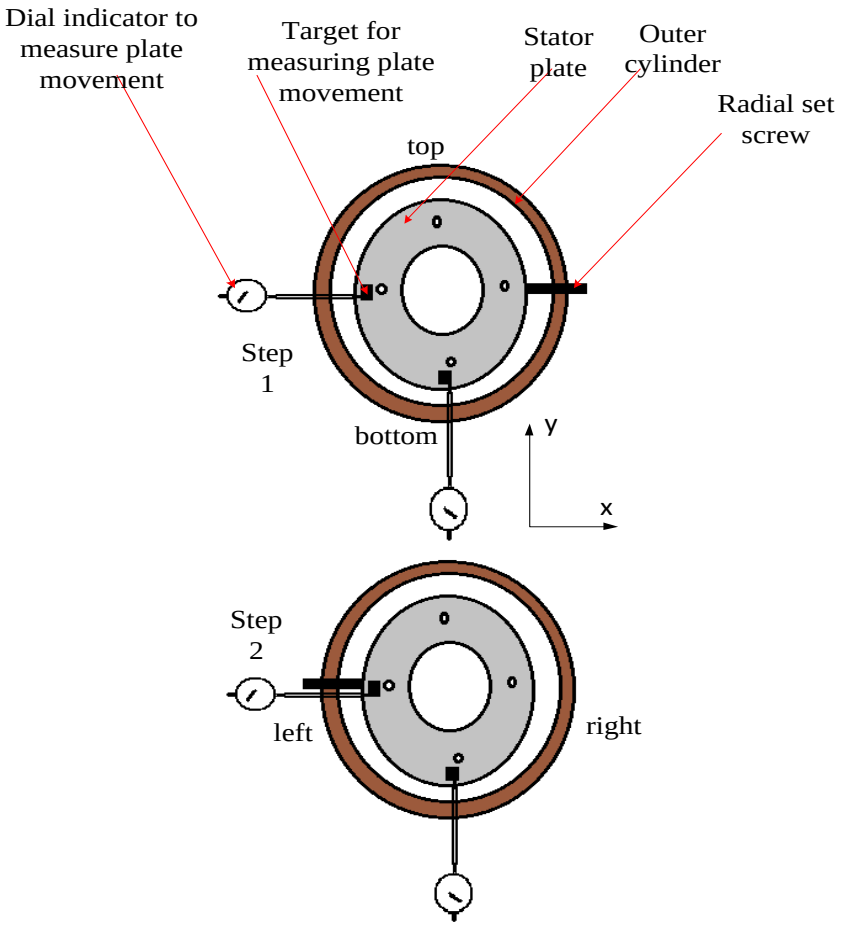

Figure 5-11 Centering of stator plates

In this procedure the plate movement is measured by using indicators. The dial indicators point against a target affixed to the plates. Two dial indicators are fixed for both x and y directions. Once they are fixed they are not touched/disturbed until the operation is complete. The targets could be a bolt with a nut at its end. The plate could be moved using the radial set screws already discussed above. This procedure is schematically shown in Figure 5-11.

The objective is to keep the dial indicator readings at zero right from the start of the experiment to the end of the experiment.The steps are as follows:

1. The axial nuts above the stator plates are loosened.
2. The radial set screws are loosened.
3. The axial nuts above the stator plates are tightened.
4. Now the dial indicators are set to zero.
5. Now the radial set screw on the right is moved so that the dial indicator for x direction shows a small displacement say 3-4 mils.
6. Now the radial set screw from the left is moved to make the dial indicator for x direction to reach zero.
7. Now the same procedure is repeated for y direction.
8. Now steps 5 and 6 are repeated until all 4 radial set screws are tight enough.
9. It is ensured that both dial indicators show zero at the end of the operation.

5.8 Levitation-Problems/issues

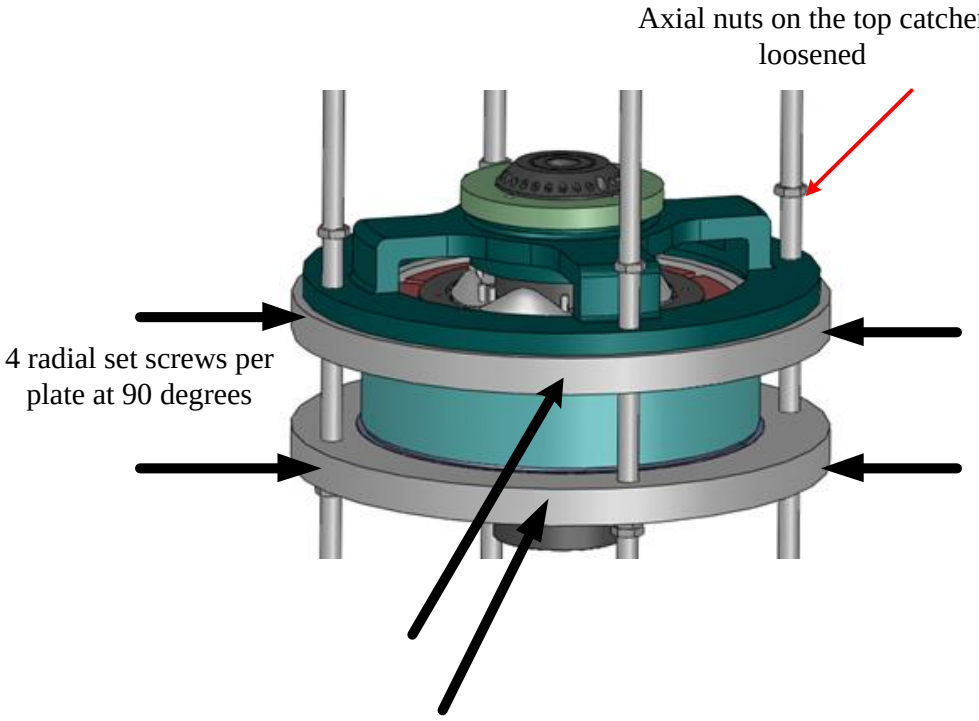

Figure 5-12 Problem during levitation process

After the assembly was done it was required to levitate the shaft. During the levitation process it was required to move the shaft to the extreme positions in the x and y directions. The voltage outputs of the sensors corresponding to the extreme positions are supposed to be noted. The median voltage positions will levitate the shaft in the center.

Before levitation it was required to loosen the catcher bearing plates. This needs to be done so that central position of the catcher bearing could be determined. It may be noted that if the catcher bearing plates are to be loosened the axial nuts above them need to be loosened. As the axial nuts were loosened, the bearing stator plates lost their axial preload. The stator plates were held in position only by the radial screws.

It was assumed that the radial preload is enough to keep the plates from moving, while trying to levitate the shaft. But it was seen that the force generated by the radial bearings was too large. Too much acceleration and force were witnessed, when the rotor hit the bearings. This resulted in slight translation and rotation of the radial bearing. This is pictorially shown in Figure 5-12.

Since the radial bearing moved the initial centering position is lost. Now it is worth wile to remember that the shims have been removed. So the process of reinserting the shims has to be repeated.

A design modification which allows for applying axial preload while freeing the catcher bearing plate needs to be devised.

6. SAFETY FEATURES

6.1 Conduits and wiring

Insulated metal wires were installed from the outer cylinder to the control electronics. The stainless steel conduits were installed on the floor to protect these wires, thereby protect any human electrocution during the testing of the rig. Before arranging the insulated wires into the conduit they were covered with high temperature fiber glass insulation sleeves. These conduits were installed using screws that were drilled and turned into concrete. The holes were drilled using hammer drill. The conduits also prevent any trip hazards. They are shown in Figure 6-1.

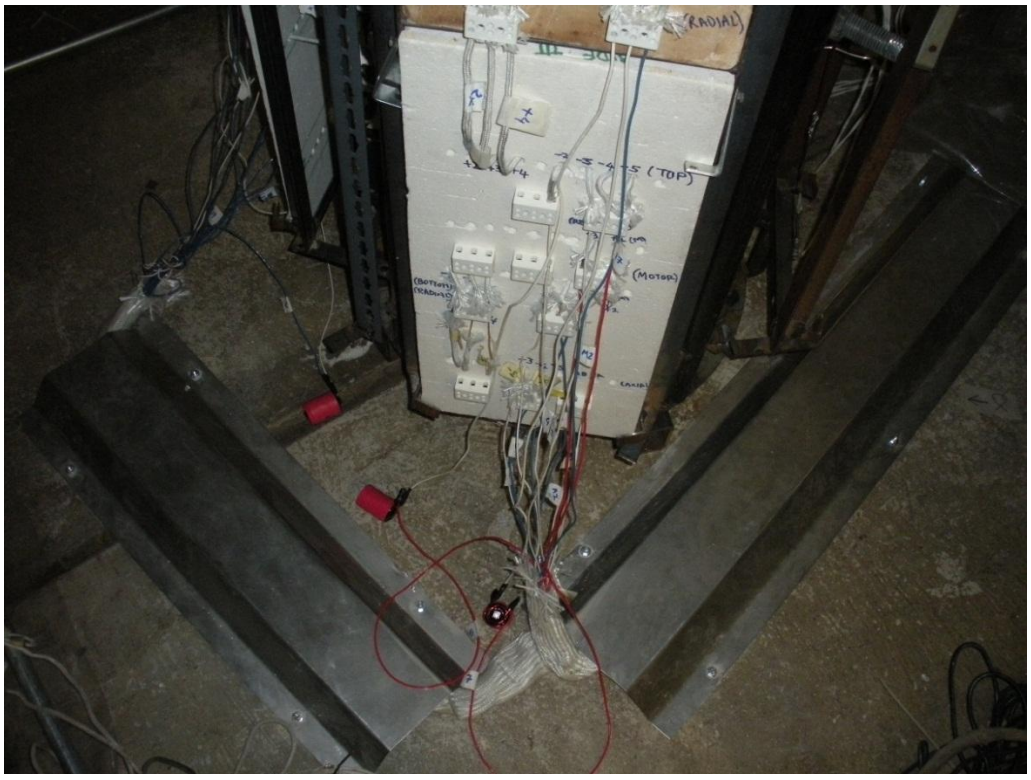

Figure 6-1 Stainless steel conduits

High temperature resistant terminal blocks were mounted onto high temperature insulation board (Zircar sheet) so as to form a junction between the outside wiring and the test rig.

6.2 Fiber glass sleeves for wires

The high temperature wires which come out of the bearings and motor have current flowing through them. If they come into contact with some metal part, might compromise personnel safety and cause elctrocution. So high temperature fiber glass sleeves were used to insulate the each of the wires coming out of the bearings/motor. It wa smade sure that the wires are held in place by twisting high temperature wires onto the sleeves.They are as shown in Figure 6-2.

Figure 6-2 Fiberglass sleeve for protection

7. ROTOR DROP MODELING

7.1 Introduction

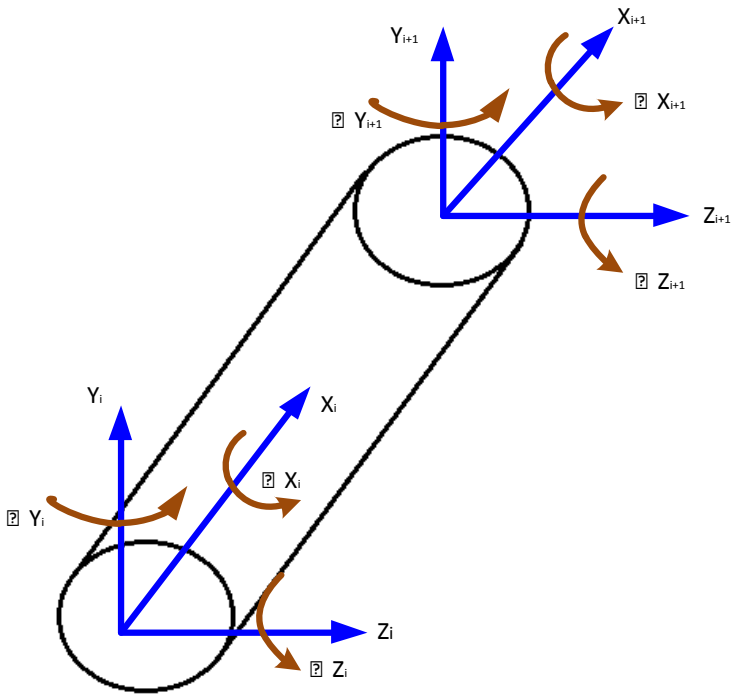

Figure 7-1 Degrees of freedom of a 3D beam element

All the elements in the finite element model are modeled on the 3D beam element. . Each element has two nodes. Each node has six degrees of freedom (three translational degrees of freedom and 3 rotational degrees of freedom) as shown in Figure 7-1.

But the model used in the study, is a 2D model since only four degrees of freedom per node is considered for calculations (axial displacement Zi and rotation about Θ_{zi} are not considered for calculations.

7.2 Mass matrix

The current analysis uses a lumped mass approach. So the mass matrix is a diagonal matrix.

Since only four degrees of freedom are considered, the mass matrix is a 4 X 4 matrix.

The mass of an element is calculated by using the formula:

$$m_e = \frac{\pi}{4}\left(D^2{}_{O,e} - D^2{}_{I,e}\right)L_e$$

m_e - Mass of the element e

$D_{O,e}$ - Outer diameter of the element e

$D_{I,e}$ - Inner diameter of the element e

L_e - Length of the element e

ρ - Density of the element material

The transverse moment of inertia of the element is given by the formula:

$$I_{t,e} = \frac{m_e}{48}\left(3D^2{}_{O,e} + 3D^2{}_{I,e} + 4L_e^2\right)$$

The mass matrix is an 8 X 8 matrix because, only 4 degrees of freedom per node is considered.

Therefore in the mass matrix the diagonal terms can be assembled as follows:

$$M_e = \begin{bmatrix} m^i{}_e & & & & & & & \\ & m^i{}_e & & & & & 0 & \\ & & I^i{}_{t,e} & & & & & \\ & & & I^i{}_{t,e} & & & & \\ & & & & m^{i+1}{}_e & & & \\ & & & & & m^{i+1}{}_e & & \\ & 0 & & & & & I^{i+1}{}_{t,e} & \\ & & & & & & & I^{i+1}{}_{t,e} \end{bmatrix}$$

7.3 Stiffness matrix

The element stiffness matrix could be assembled based on the linear elasticity assumptions. Sufficient compensation is provided for out of plane shear deformation.

Below are the descriptions for variables used in stiffness matrix:

$$\Phi_y = 12EI_t\alpha_y / (GAL_e^2)$$

$$\Phi_z = 12EI_t\alpha_z / (GAL_e^2)$$

α_y Transverse shear from factor in Y direction

α_z Transverse shear from factor in Z direction

G Elastic Shear Modulus

E Young's modulus

A cross sectional area of beam element

$$K_e = \begin{bmatrix} 12EI_{ta,e}/L_e^{\,2}\beta_z & 0 & 0 & 6EI_{ta,e}/L_e\beta_z & -12EI_{ta,e}/L_e^{\,2}\beta_z & 0 & 0 & 6EI_{ta,e}/L_e\beta_z \\ & 12EI_{ta,e}/L_e^{\,2}\beta_y & -6EI_{ta,e}/L_e\beta_y & 0 & 0 & -12EI_{ta,e}/L_e^{\,2}\beta_y & -6EI_{ta,e}/L_e\beta_y & 0 \\ & & EI_{ta,e}(4+\Phi_y)/\beta_y & 0 & 0 & 6EI_{ta,e}/L_e\beta_y & EI_{ta,e}(2-\Phi_y)/\beta_y & 0 \\ & & & EI_{ta,e}(4+\Phi_z)/\beta_z & -6EI_{ta,e}/L_e\beta_z & 0 & 0 & EI_{ta,e}(2-\Phi_z)/\beta_z \\ & & & & 12EI_{ta,e}/L_e^{\,2}\beta_z & 0 & 0 & -6EI_{ta,e}/L_e\beta_z \\ & & & & & 12EI_{ta,e}/L_e^{\,2}\beta_y & 6EI_{ta,e}/L_e\beta_y & 0 \\ & & & & & & EI_{ta,e}(4+\Phi_y)/\beta_y & 0 \\ SYM & & & & & & & EI_{ta,e}(4+\Phi_y)/\beta_z \end{bmatrix}$$

$I_{ta,e}$ Transverse area moment of inertia

$$I_{ta,e} = \frac{\pi}{64}(D_{o,e}^{\,4} - D_{i,e}^{\,4})$$

7.4 Gyroscopic matrix

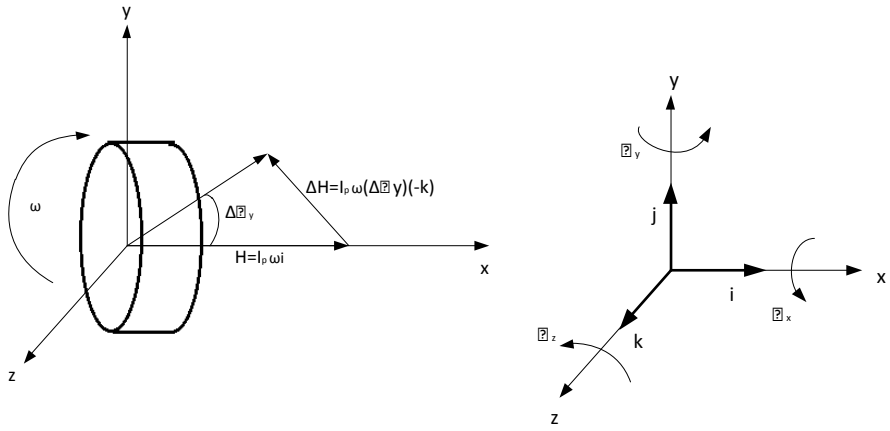

Figure 7-2 Gyroscopic effect

Figure 7-2 could be used to determine the elements of the gyroscopic matrix. The angular momentum is given by $H = I_p.\omega$.

The torque in the Z-direction is given by

$$T_z = \frac{dH}{dt} \qquad Tz = -Ip.\omega.\frac{d\theta_y}{dt}.k$$

Similarly in the y direction, $T_y = Ip.\omega.\frac{d\theta_y}{dt}.j$

So, the gyroscopic matrix could be assembled for a two noded element with four degrees of freedom per node as

$$G_i = \begin{bmatrix} 0 & 0 & 0 & 0 \\ 0 & 0 & 0 & 0 \\ 0 & 0 & 0 & I_{p,i}\omega \\ 0 & 0 & -I_{p,i}\omega & 0 \end{bmatrix}$$

7.5 Negative stiffness

The magnetic bearings are present at nodes 8, 14 of the finite element model. The rotor is subjected to magnetic forces due to the permanent magnets present in the magnetic bearing system. Due to permanent nature of the magnets these forces are present even when there is loss of power. Our objective is to model the rotor drop, when a spinning rotor is dropped onto the catcher bearings, after the magnetic bearing system losses power. So this effect due to the magnets needs to be modeled into the system since it would greatly affect the way in which the rotor behaves after rotor drop.

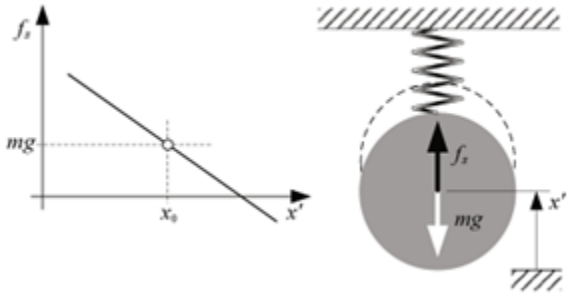

Figure 7-3 Spring stiffness

The Figure 7-3 the behavior of a magnetic spring is shown.

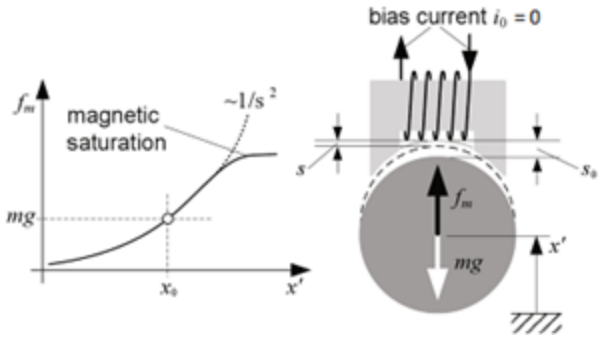

Figure 7-4 Magnetic bearing stiffness

Figure 7-4 shows the behaviors of magnetic bearing stiffness.

The way in which a magnetic bearing behaves is opposite to the way in which a mechanical spring operates. In Figure 7-3 it is shown how if the distance x' decreases, the spring force also decreases. In Figure 7-4, it is shown how if the distance decreases, (closer the rotor comes in touch with the magnet) the magnetic attraction increases. Smaller the air gap, higher is the magnetic attraction.

The force in a spring is given by the relation:

$$f_s = k_s.x$$

k_s stiffness of the spring

x elongation of the spring

In contrast, the force to due to a magnet can be linearized as:

$$f_m = -k_m.x$$

k_m stiffness of the bearing (measured experimentally)

x air gap

7.5.1 *Treatment of negative stiffness*

Force due to permanent magnets act at the magnetic bearing locations. This force is indirectly proportional to air gap. Thus a negative stiffness is added to the diagonal elements at nodes 8,14 (for the y and z translational degrees of freedom only). Thus the force due to magnets is taken care of.

7.6 Condition for contact force

The smaller circle shown in the figure below depicts the rotor and the larger circle is the inner surface of the catcher bearing shell. When the rotor is centered inside the catcher bearing shell, there would be a uniform clearance around the rotor.

At the each time step during the finite element simulations, the distance between the centers of the rotor and the catcher bearing are checked. If this distance is greater than the clearance, (the magnitude of this would be the deflection) then a force acts on the contact point, directed towards the center of the rotor. This is shown in Figure 7-5.

Another force acts tangential to this force. This tangential force will depend upon the friction coefficient. The tangential force could be denoted by F_t and the contact force by F_c .

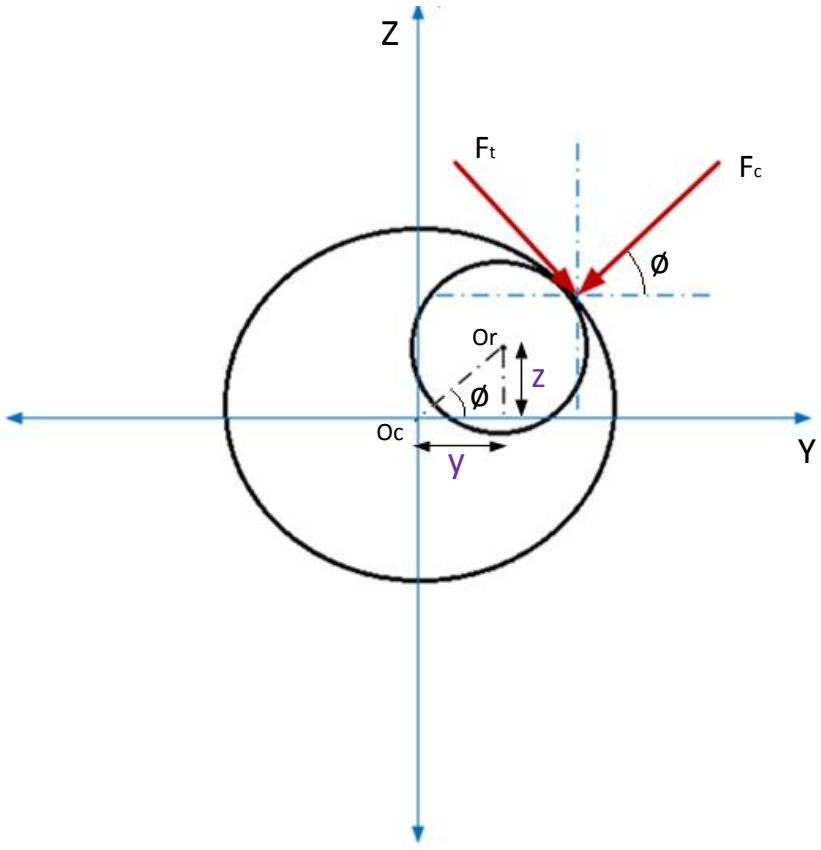

Figure 7-5 Contact force – resolution

Condition for contact force to exist

$$\sqrt{(z^2 + y^2)} - c > 0$$

z the z component of the position of the center of the rotor

y the y component of the position of the center of the rotor

c clearance between rotor and catcher bearing inner surface

The angle ϕ can be calculated by:

$$\phi = \tan^{-1}(z / y)$$

From the above figure we can derive

$$F_{cy} = -F_c.\cos\phi$$

$$F_{cz} = -F_c.\sin\phi$$

$$F_{ty} = F_t.\sin\phi$$

$$F_{tz} = -F_t.\cos\phi$$

$$F_t = \mu.F_c$$

μ Friction coefficient

Therefore

$$F_{ty} = \mu.F_c.\sin\phi$$

$$F_{tz} = -\mu . F_c . \cos\phi$$

Thus the tangential force and the normal force could be put forth in terms of the contact force due to the deflection produced by the rotor onto the catcher bearing.

7.7 Calculation of contact force

The contact force that is developed due to the contact of a rotor (which is a cylinder) inside the catcher bearing shell (which is a cylinder) can be found out using hertzian contact equations. The cylinder-cylinder contact could be approximated by using a cylinder-plane contact equation as shown in Figure 7-6.

$$\delta = \sqrt{(z^2 + y^2)} - c$$

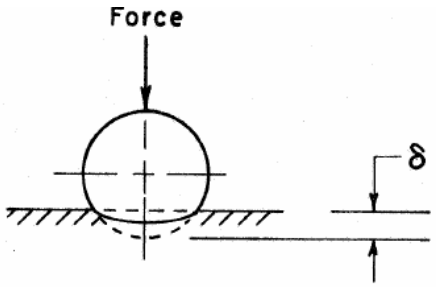

Figure 7-6 Contact force calculation

$$\delta = \left(\frac{F_c}{L}\right).(\lambda_1 + \lambda_2).\left[1 + \ln\left(\frac{L^3}{(\lambda_1 + \lambda_2).F_c.R}\right)\right]$$

where

$$\lambda_1 = \frac{1-\nu_1^{\,2}}{\pi.E_1}$$

$$\lambda_2 = \frac{1-\nu_2^{\,2}}{\pi.E_2}$$

L width of catcher bearing

ν_1 Poisson's ratio of Graphalloy

E_1 Young's modulus of Graphalloy

ν_2 Poisson's ratio for inconel (shaft)

E_2 Young's modulus for inconel (shaft)

7.7.1 *Interpolation to find out contact force*

Since the deflection at each time step would be known, the force that deflection would cause could be calculated using the above expression.

The above equation is non linear involving $F_{c.}$ So an interpolation process was initiated at end of each time step to calculate the force for the next time step.

By trial and error it was found that the deflection does not cross 10 mils for any extreme condition. So a distance a ten mils was divided into 1000 parts (gradually increasing from 0 to 10 mils). Each value of this deflection was used to solve the corresponding contact force. The graph drawn below in Figure 7-7 utilizes these values.

Now when the deflection of the previous time step is known, it is checked whether it lies between which two interpolation steps of distance. The corresponding contact force could be calculated as follows by interpolation.

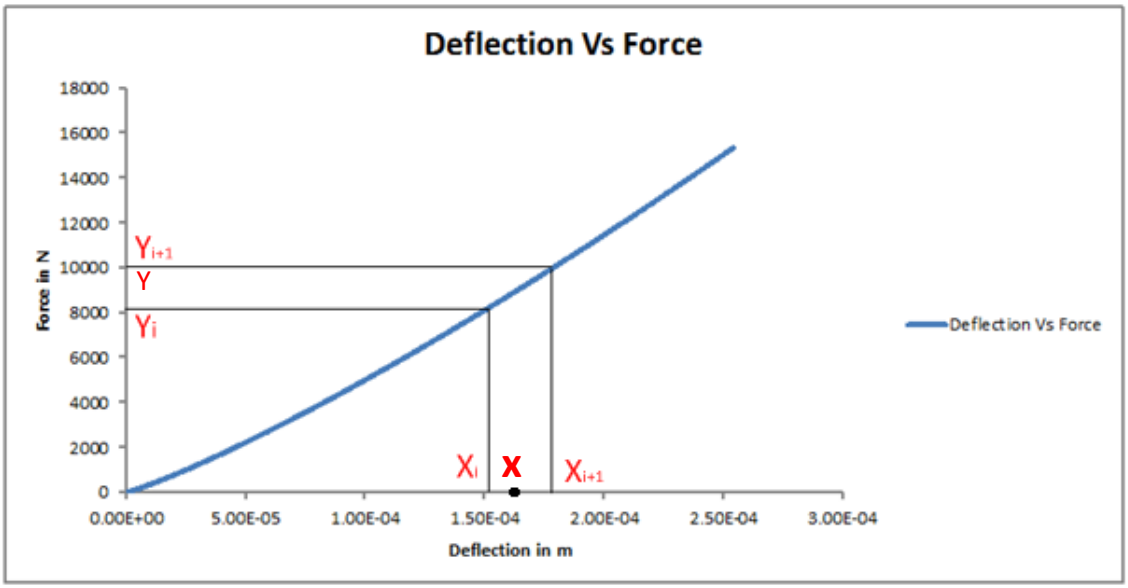

Figure 7-7 Interpolation for contact force

$$Y = Y_i + \left(\frac{X - X_i}{X_{i+1} - X_i} \right) \left(Y_{i+1} - Y_i \right)$$

7.8 Force vector

The force vector consists of forces that act on the rotor. The two set of forces that act on the rotor are:

- Contact force due to the rotor hitting the catcher bearing.
- Unbalance forces due to rotor mass imbalance.

$$\{ f \} = \{ f_{cb} \} + \{ f_{ub} \}$$

f_{cb} Forces due to rotor hitting the catcher bearing

f_{ub} Forces due to rotor mass imbalance

$$\{ f_{cb} \} = \begin{Bmatrix} \cdot \\ \cdot \\ \cdot \\ f_{ya} \leftarrow (i_{ca} - 1)4 + 1 \\ f_{za} \leftarrow (i_{ca} - 1)4 + 2 \\ \cdot \\ \cdot \\ \cdot \\ f_{yb} \leftarrow (i_{cb} - 1)4 + 1 \\ f_{zb} \leftarrow (i_{cb} - 1)4 + 2 \\ \cdot \\ \cdot \end{Bmatrix}$$

f_{ya}, f_{yb} Forces along y direction at catcher bearing nodes a, b

f_{za}, f_{zb} Forces along z direction at catcher bearing nodes a, b

$$\{f_{ub}\} = \begin{Bmatrix} \vdots \\ m_a e_a \omega^2 (\cos(\omega t + \phi_a) \\ m_a e_a \omega^2 (\sin(\omega t + \phi_a) \\ \vdots \\ m_b e_b \omega^2 (\cos(\omega t + \phi_b) \\ m_b e_b \omega^2 (\sin(\omega t + \phi_b) \\ \vdots \end{Bmatrix} \begin{matrix} \\ \\ \\ \leftarrow (i_{ua} - 1)4 + 1 \\ \leftarrow (i_{ua} - 1)4 + 2 \\ \\ \\ \leftarrow (i_{ub} - 1)4 + 2 \\ \leftarrow (i_{ub} - 1)4 + 1 \\ \\ \end{matrix}$$

i_{ua}, i_{ub} Unbalance nodes

m_a, m_b Unbalance masses at unbalance nodes a,b

$e_{a,} e_b$ Unbalance eccentricities at nodes a,b

$\phi_{a,} \phi_b$ Pressure angles at nodes a,b

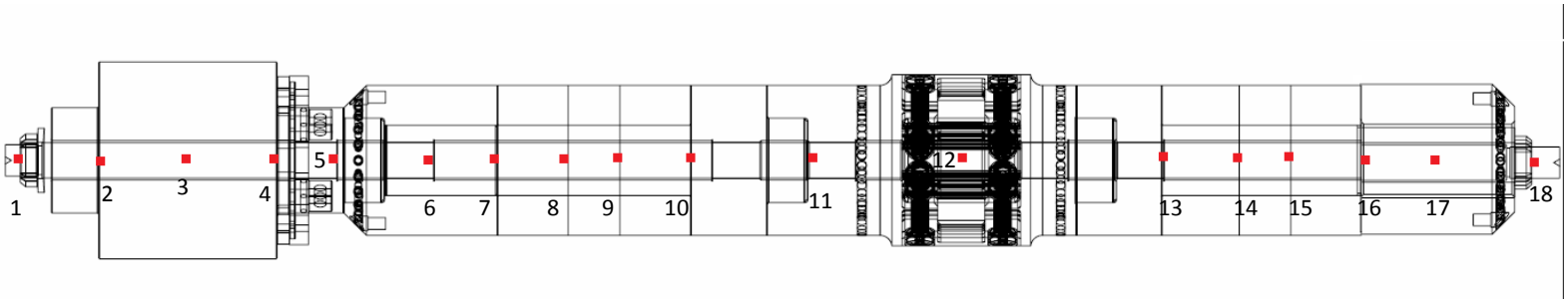

Figure 7-8 FEA model of rotor

7.9 Finite element model of rotor

The finite element model of the rotor used for dynamic analysis is shown in Figure 7-8. It's composed of 2 noded elements in series. A total of 18 nodes, comprising of 17 elements with 4 degrees of freedom per node were used.

7.9.1 *Salient features of finite element model of rotor*

No of nodes	:	18
No of elements	:	17
No of degrees of freedom per node	:	4
Total no of degrees of freedom	:	72
Total length	:	0.835 m
Catcher bearing nodes	:	6, 17
Magnetic bearing nodes	:	8,14
Shaft Material	:	Inconel
Young's Modulus	:	30.3×10^9 N/m^2
Rigidity Modulus	:	79×10^9 N/m^2
Catcher bearing Material	:	Graphalloy

Poisson's ratio : 0.30

The element data is shown in Table 7-1.

Table 7-1 Element data for FEA model of rotor

Element	**Start node**	**End node**	**Outer Diameter**	**Inner Diameter**	**Length**
			m	**m**	**m**
1	1	2	0.0429	0.0192	0.0410
2	2	3	0.1067	0.0214	0.0489
3	3	4	0.1067	0.0214	0.0489
4	4	5	0.0286	0.0198	0.0347
5	5	6	0.0813	0.0206	0.0318
6	6	7	0.0813	0.0214	0.0508
7	7	8	0.0813	0.0214	0.0377
8	8	9	0.0813	0.0214	0.0278
9	9	10	0.0813	0.0214	0.0377
10	10	11	0.0813	0.0214	0.0706
11	11	12	0.0870	0.0204	0.0738
12	12	13	0.0851	0.0208	0.1078
13	13	14	0.0813	0.0214	0.0412
14	14	15	0.0813	0.0214	0.0278
15	15	16	0.0813	0.0214	0.0377
16	16	17	0.0813	0.0214	0.0487
17	17	18	0.0550	0.0214	0.0425

Finally the equations of motion look like this:

$$M\ddot{x}+(G+C)\dot{x}+Kx=f$$

$$\ddot{x}=\begin{pmatrix}\ddot{y}_1\\ \ddot{z}_1\\ \ddot{\theta}_{y,1}\\ \ddot{\theta}_{z,1}\\ \ddot{y}_2\\ \ddot{z}_2\\ \ddot{\theta}_{y,2}\\ \ddot{\theta}_{z,2}\\ \cdot\\ \cdot\\ \cdot\\ \cdot\\ \cdot\\ \cdot\\ \cdot\\ \ddot{y}_{18}\\ \ddot{z}_{18}\\ \ddot{\theta}_{y,18}\\ \ddot{\theta}_{z,18}\end{pmatrix} \qquad \dot{x}=\begin{pmatrix}\dot{y}_1\\ \dot{z}_1\\ \dot{\theta}_{y,1}\\ \dot{\theta}_{z,1}\\ \dot{y}_2\\ \dot{z}_2\\ \dot{\theta}_{y,2}\\ \dot{\theta}_{z,2}\\ \cdot\\ \cdot\\ \cdot\\ \cdot\\ \cdot\\ \cdot\\ \cdot\\ \dot{y}_{18}\\ \dot{z}_{18}\\ \dot{\theta}_{y,18}\\ \dot{\theta}_{z,18}\end{pmatrix} \qquad x=\begin{pmatrix}y_1\\ z_1\\ \theta_{y,1}\\ \theta_{z,1}\\ y_2\\ z_2\\ \theta_{y,2}\\ \theta_{z,2}\\ \cdot\\ \cdot\\ \cdot\\ \cdot\\ \cdot\\ \cdot\\ \cdot\\ y_{18}\\ z_{18}\\ \theta_{y,18}\\ \theta_{z,18}\end{pmatrix}$$

As already discussed:

- In the current FE model used for analysis there are 18 nodes.
- Each element has two nodes, therefore there are 17 elements.
- Each node has two translational and two rotational degrees of freedom.
- Total no of degrees of freedom is 72.
- Therefore the $\ddot{x}, \dot{x}, x$ vectors each have a length of 72 X 1.
- Therefore there are 72 simultaneous and homogenous equations to be solved.

Solving these 72 simultaneous and homogeneous differential equations is an arduous task if solved using matrix inversion method. So a special method called modal coordinates transformation is used to and quickly and effectively solve it.

Modal coordinate transformation method:

In the modal coordinate transformation method, the simultaneous and homogeneous equations are converted into same no of independent equations which would make solving the system of equations a whole lot easier.

In the absence of damping and external forces this equation reduces to :

$$M\ddot{x} + Kx = 0$$

The set of equations of motion equation could be rewritten as:

$$\sum_{j=1}^{n} m_{ij}\ddot{x}_j(t) + \sum_{j=1}^{n} k_{ij}x_j(t) = 0$$

where m_{ij} and k_{ij} are individual elements in the mass and stiffness matrices (i^{th} row and j^{th} column) and $\ddot{x}_j(t), x_j(t)$ denote the j^{th} row elements in the respective matrices

For i=1 to n (in our case n=72)

Now let's put

$$x(t) = U.g(t)$$

$$\dot{x}(t) = U.\dot{g}(t)$$

$$\ddot{x}(t) = U.\ddot{g}(t)$$

Rewriting the equations:

$$\ddot{g}(t)\sum_{j=1}^{n} m_{ij}u_j + g(t)\sum_{j=1}^{n} k_{ij}u_j = 0$$

Rearranging terms we get,

$$-\frac{\ddot{g}(t)}{g(t)} = \frac{\sum_{j=1}^{n} k_{ij}u_j}{\sum_{j=1}^{n} m_{ij}u_j}$$

Equating the above to λ

$$-\frac{\ddot{g}(t)}{g(t)} = \frac{\sum_{j=1}^{n} k_{ij} u_j}{\sum_{j=1}^{n} m_{ij} u_j} = \lambda$$

Therefore

$$\ddot{g}(t) + \lambda\, g(t) = 0$$

And

$$\sum_{j=1}^{n} k_{ij} u_j - \lambda \sum_{j=1}^{n} m_{ij} u_j = 0$$

In matrix form this could be written as

$$K.U = \omega^2.M.U$$

This is an eigen value problem.

The characteristic equation $\det(K - \omega^2 M) = 0$ is used to solve for

ω^2 a diagonal matrix whose diagonal elements represent the eigen values

U the transformation matrix or the matrix of Eigen vectors (each column of this matrix U_r, r = 1 to n is an Eigen vector)

$$Ku_r = \omega_r{}^2 Mu_r$$
$$Ku_s = \omega_s{}^2 Mu_s$$

where

ω_r , ω_s — r[th] and s[th] rows in the Eigen value diagonal matrix ω^2

u_r , u_s — r[th] and s[th] columns in the Eigen vector matrix U

Premultiplying both sides of the first equation by $u_s{}^T$ and the second one by $u_r{}^T$

$$u_s{}^T Ku_r = \omega_r{}^2 u_s{}^T Mu_r$$
$$u_r{}^T Ku_s = \omega_s{}^2 u_r{}^T Mu_s$$

Transpose the second of the above equations and subtract it from the first equations and considering that M and K matrices are symmetric ($M^T = M; K^T = K$)

$$(\omega_r{}^2 - \omega_s{}^2) u_s{}^T Mu_r = 0$$

Since each natural frequency is different $\omega_r \neq \omega_s$

$$u_s{}^T Mu_r = 0$$

$$u_s{}^T Ku_r = 0$$

where s and r are not equal

$$Ku_r = \omega_r{}^2 Mu_r$$
$$Ku_s = \omega_s{}^2 Mu_s$$

From above formulas

$$Ku_1 = \omega_1^2 Mu_1$$
$$Ku_2 = \omega_2^2 Mu_2$$

Pre multiplying first equation by u_1^T and second equation by u_2^T

$$u_1^T Ku_1 = \omega_1^2 u_1^T Mu_1$$
$$u_2^T Ku_2 = \omega_2^2 u_2^T Mu_2$$

Let's introduce

$$u_1^T Mu_1 = m'_{11}$$
$$u_2^T Mu_2 = m'_{22}$$

$$u_1^T Ku_1 = k'_{11}$$
$$u_2^T Ku_2 = k'_{22}$$

From the above equations, we can derive

$$\omega_1^2 = \frac{k'_{11}}{m'_{11}} \quad \omega_2^2 = \frac{k'_{22}}{m'_{22}}$$

This is true for each w_r for each r = 1 to n

In matrix form

$$U^T MU = 1$$
$$U^T KU = \omega^2$$

Now returning back to the equation

$$M\ddot{x}+\left(G+C\right)\dot{x}+Kx=f$$

Let's put

$$x\left(t\right)=U.g(t)$$

$$\dot{x}(t)=U.\dot{g}(t)$$

$$\ddot{x}(t)=U.\ddot{g}(t)$$

We get,

$$M.U.\ddot{g}(t)+\left(G+C\right).U.\dot{g}(t)+K.U.g(t)=f(t)$$

Premultiply by U^T

$$\ddot{g}(t)+U^T.\left(G+C\right).U.\dot{g}(t)+\omega^2.g(t)=U^T.f(t)$$

This equation will give n uncoupled/independent equation to be solved for g(t).

$\ddot{g}(t),\dot{g}(t)$ could be calculated by comparing g(t) of current time step with previous time steps.

After solving for $\ddot{g}(t),\dot{g}(t)$,g(t) they could be converted back into $\ddot{x}(t)$, $\dot{x}(t)$,x(t) by using

$$x\left(t\right)=U.g(t)$$

$$\dot{x}(t) = U.\dot{g}(t)$$

$$\ddot{x}(t) = U.\ddot{g}(t)$$

7.10 Assembly of matrices

7.10.1 *Stiffness matrix*

A stiffness matrix is assembled for each element. There are 17 elements in our FE model. So, 17 different stiffness matrices are assembled. Since there are 18 nodes, they need to be assembled to form a 72 X 72 matrix (in other words, 72 different equations- 18 X 4 degrees of freedom per node).

If the arrangement of nodes and elements could be remembered, it is a very linear arrangement with elements arranged from one end of the rotor to the other. In other words elements 2 to 16 have one element to their left and one element to their right. So, they share a common node with each of these elements noted above. This affects the way in which the stiffness matrix is assembled (the same is true for the assembly of global mass matrix).

The assembly for the first two element matrices in the global stiffness matrix is as shown below. The assembly of other elements into the global stiffness matrix is very similar. The superscript (1 or 2) denotes the element number. The subscript (11 to 88) denotes the position of the element in the corresponding element stiffness matrix. For example

K^{1}_{48} denotes the element in fourth row and 8th column of the stiffness matrix for element1.

7.10.2 *Mass matrix*

The concept assembly of the mass matrix and the naming terminology is exactly the same as that of stiffness matrix. The assembly of mass matrices for the first two elements into global mass matrix is as shown on pages 132-133. The other element mass matrices are assembled in the same fashion.

$$
\begin{bmatrix}
K^1_{11} & K^1_{12} & K^1_{13} & K^1_{14} & K^1_{15} & K^1_{16} & K^1_{17} & K^1_{18} & & & & & & & & \\
K^1_{21} & K^1_{22} & K^1_{23} & K^1_{24} & K^1_{25} & K^1_{26} & K^1_{27} & K^1_{28} & & & & & & & & \\
K^1_{31} & K^1_{32} & K^1_{33} & K^1_{34} & K^1_{35} & K^1_{36} & K^1_{37} & K^1_{38} & & & & & & & & \\
K^1_{41} & K^1_{42} & K^1_{43} & K^1_{44} & K^1_{45} & K^1_{46} & K^1_{47} & K^1_{48} & & & & & & & & \\
K^1_{51} & K^1_{52} & K^1_{53} & K^1_{54} & K^1_{55}+K^2_{11} & K^1_{56}+K^2_{12} & K^1_{57}+K^2_{13} & K^1_{58}+K^2_{14} & K^2_{15} & K^2_{16} & K^2_{17} & K^2_{18} & & & & \\
K^1_{61} & K^1_{62} & K^1_{63} & K^1_{64} & K^1_{65}+K^2_{21} & K^1_{66}+K^2_{22} & K^1_{67}+K^2_{23} & K^1_{68}+K^2_{24} & K^2_{25} & K^2_{26} & K^2_{27} & K^2_{28} & & & & \\
K^1_{71} & K^1_{72} & K^1_{73} & K^1_{74} & K^1_{75}+K^2_{31} & K^1_{76}+K^2_{32} & K^1_{77}+K^2_{33} & K^1_{78}+K^2_{34} & K^2_{35} & K^2_{36} & K^2_{37} & K^2_{38} & & & & \\
K^1_{81} & K^1_{82} & K^1_{83} & K^1_{84} & K^1_{85}+K^2_{41} & K^1_{86}+K^2_{42} & K^1_{87}+K^2_{43} & K^1_{88}+K^2_{44} & K^2_{45} & K^2_{46} & K^2_{47} & K^2_{48} & & & & \\
 & & & & K^2_{51} & K^2_{52} & K^2_{53} & K^2_{54} & K^2_{55}+\ldots & K^2_{56}+\ldots & K^2_{57}+\ldots & K^2_{58}+\ldots & & & & \\
 & & & & K^2_{61} & K^2_{62} & K^2_{63} & K^2_{64} & K^2_{65}+\ldots & K^2_{66}+\ldots & K^2_{67}+\ldots & K^2_{68}+\ldots & & & & \\
 & & & & K^2_{71} & K^2_{72} & K^2_{73} & K^2_{74} & K^2_{75}+\ldots & K^2_{76}+\ldots & K^2_{77}+\ldots & K^2_{78}+\ldots & & & & \\
 & & & & K^2_{81} & K^2_{82} & K^2_{83} & K^2_{84} & K^2_{85}+\ldots & K^2_{86}+\ldots & K^2_{87}+\ldots & K^2_{88}+\ldots & & & & \\
 & & & & & & & & \ldots & \ldots & \ldots & \ldots & \ldots & \ldots & \ldots & \ldots \\
 & & & & & & & & \ldots & \ldots & \ldots & \ldots & \ldots & \ldots & \ldots & \ldots \\
 & & & & & & & & \ldots & \ldots & \ldots & \ldots & \ldots & \ldots & \ldots & \ldots \\
 & & & & & & & & \ldots & \ldots & \ldots & \ldots & \ldots & \ldots & \ldots & \ldots \\
 & & & & & & & & & & & & & & & \\
 & & & & & & & & & & & & & & &
\end{bmatrix}
$$

$$
\begin{bmatrix}
M^1_{11} & M^1_{12} & M^1_{13} & M^1_{14} & M^1_{15} & M^1_{16} & M^1_{17} & M^1_{18} & & & & & & & & \\
M^1_{21} & M^1_{22} & M^1_{23} & M^1_{24} & M^1_{25} & M^1_{26} & M^1_{27} & M^1_{28} & & & & & & & & \\
M^1_{31} & M^1_{32} & M^1_{33} & M^1_{34} & M^1_{35} & M^1_{36} & M^1_{37} & M^1_{38} & & & & & & & & \\
M^1_{41} & M^1_{42} & M^1_{43} & M^1_{44} & M^1_{45} & M^1_{46} & M^1_{47} & M^1_{48} & & & & & & & & \\
M^1_{51} & M^1_{52} & M^1_{53} & M^1_{54} & M^1_{55}+M^2_{11} & M^1_{56}+M^2_{12} & M^1_{57}+M^2_{13} & M^1_{58}+M^2_{14} & M^2_{15} & M^2_{16} & M^2_{17} & M^2_{18} & & & & \\
M^1_{61} & M^1_{62} & M^1_{63} & M^1_{64} & M^1_{65}+M^2_{21} & M^1_{66}+M^2_{22} & M^1_{67}+M^2_{23} & M^1_{68}+M^2_{24} & M^2_{25} & M^2_{26} & M^2_{27} & M^2_{28} & & & & \\
M^1_{71} & M^1_{72} & M^1_{73} & M^1_{74} & M^1_{75}+M^2_{31} & M^1_{76}+M^2_{32} & M^1_{77}+M^2_{33} & M^1_{78}+M^2_{34} & M^2_{35} & M^2_{36} & M^2_{37} & M^2_{38} & & & & \\
M^1_{81} & M^1_{82} & M^1_{83} & M^1_{84} & M^1_{85}+M^2_{41} & M^1_{86}+M^2_{42} & M^1_{87}+M^2_{43} & M^1_{88}+M^2_{44} & M^2_{45} & M^2_{46} & M^2_{47} & M^2_{48} & & & & \\
 & & & & M^2_{51} & M^2_{52} & M^2_{53} & M^2_{54} & M^2_{55}+\ldots & M^2_{56}+\ldots & M^2_{57}+\ldots & M^2_{58}+\ldots & & & & \\
 & & & & M^2_{61} & M^2_{62} & M^2_{63} & M^2_{64} & M^2_{65}+\ldots & M^2_{66}+\ldots & M^2_{67}+\ldots & M^2_{68}+\ldots & & & & \\
 & & & & M^2_{71} & M^2_{72} & M^2_{73} & M^2_{74} & M^2_{75}+\ldots & M^2_{76}+\ldots & M^2_{77}+\ldots & M^2_{78}+\ldots & & & & \\
 & & & & M^2_{81} & M^2_{82} & M^2_{83} & M^2_{84} & M^2_{85}+\ldots & M^2_{86}+\ldots & M^2_{87}+\ldots & M^2_{88}+\ldots & & & & \\
 & & & & & & & & \ldots & \ldots & \ldots & \ldots & \ldots & \ldots & \ldots & \ldots \\
 & & & & & & & & \ldots & \ldots & \ldots & \ldots & \ldots & \ldots & \ldots & \ldots \\
 & & & & & & & & \ldots & \ldots & \ldots & \ldots & \ldots & \ldots & \ldots & \ldots \\
 & & & & & & & & \ldots & \ldots & \ldots & \ldots & \ldots & \ldots & \ldots & \ldots
\end{bmatrix}
$$

8. RESULTS OF SIMULATION

8.1 Introduction

The equations of motion derived in the previous section were simulated using MATLAB software. The response was simulated by varying the following input conditions:

1. Negative position stiffness
2. Coefficient of friction
3. Initial spin speed
4. Clearance between rotor and catcher bearing

The system responses that were tracked using the simulation were:

1. Orbit of the center of the rotor after rotor is dropped
2. Displacement in the X direction
3. Displacement in the Y direction
4. Angular displacement of the rotor
5. Whirl velocity of the rotor
6. Bearing force at catcher bearing node

The following parametric studies were performed:

1. Effect of negative stiffness, friction, clearance and spin speed on rotor stoppage time
2. Effect of friction, clearance and spin speed on bearing force
3. Effect friction, clearance and spin speed on whirl velocity
4. Effect of presence/absence of negative stiffness on rotor behavior with regards to tendency to hit and bounce back from the walls

8.2 Actual input conditions

Friction coefficient	:	0.15
Negative stiffness	:	6131545 N/m (35000lb/in)
Clearance (radial)	:	0.00254 m (10 mils)
Initial Angular velocity	:	7000 rpm

8.3 Effect of system parameters on rotor stoppage time

The rotor after being dropped (in a rare case of power failure/failure of control system) loses its ability to levitate in the center and hits the catcher bearing walls and thereby protecting magnetic bearings. The rotor then progressively loses its spin speed due to constant hitting and dragging, whirling along the walls of the rotor before it comes to a

stop. The amount of time taken by the rotor to reach zero rpm is called stoppage time. The stoppage time depends mainly on negative stiffness of the magnetic bearings, initial spin speed, friction of catcher bearing and catcher bearing clearance.

8.3.1 *Effect of negative stiffness on rotor stoppage time*

More the negative stiffness more is the attraction towards the magnets. Hence there is more deflection into the catcher bearing material. Thereby there is more normal force onto the rotor. More the normal force more is the tangential friction force acting opposite to the direction of tangential velocity of rotor. Hence there is more resistance to spin. So, the rotor comes to a stop sooner.

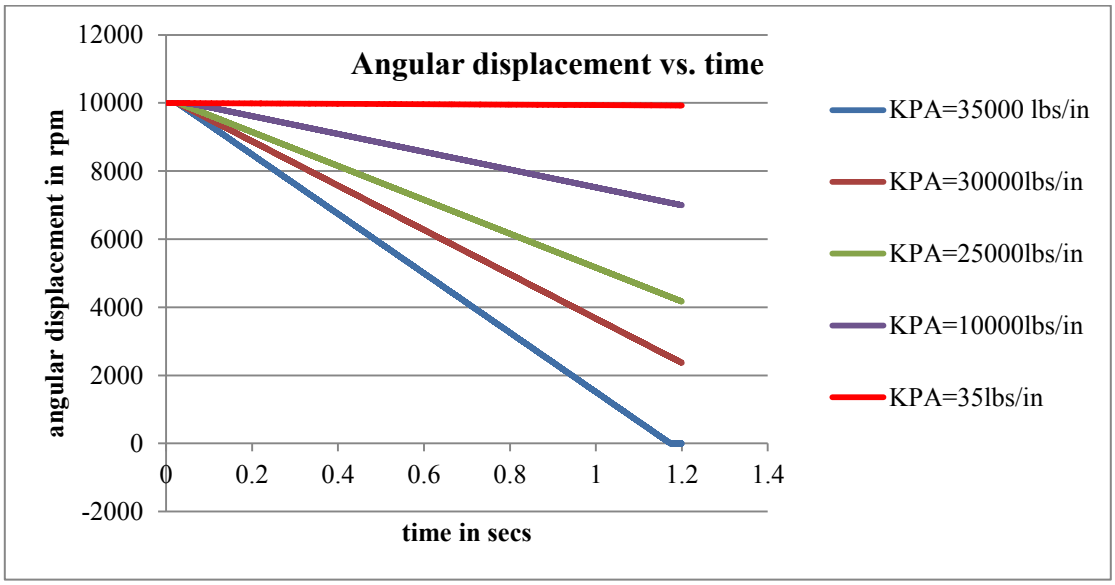

Figure 8-1 Effect of negative position stiffness on stoppage time

As shown in Figure 8-1 the rotor stoppage time drops from about 4.1 seconds for a negative stiffness of 10000 lbs. /in to about 1 second for a negative stiffness of 35000 lbs. /in. (other variables used were coefficient of friction-0.15, radial clearance -0.00254 (10 mils), initial spin speed -10000 rpm).

8.3.2 *Effect of friction on rotor stoppage time*

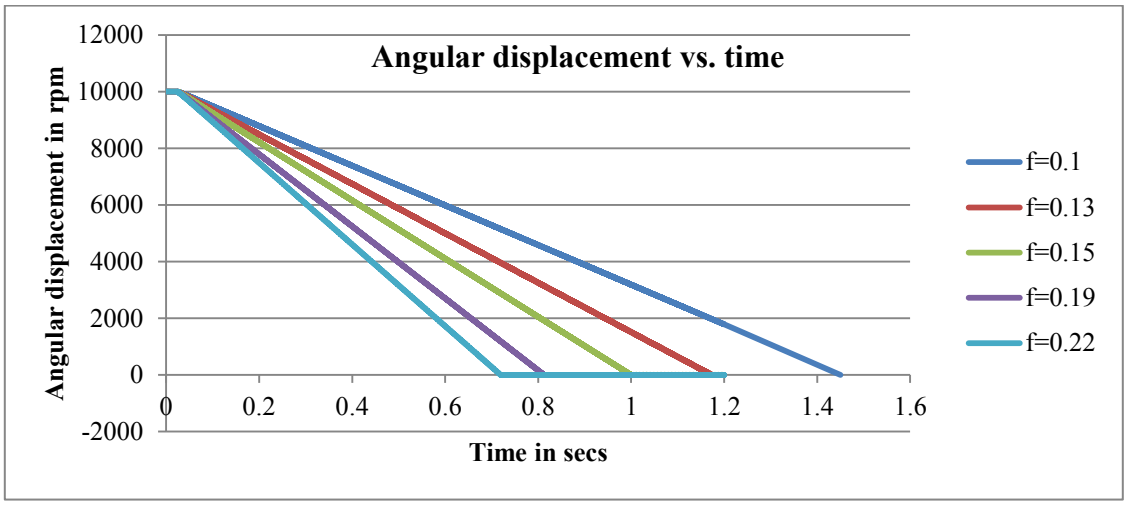

Figure 8-2 Effect of friction on stoppage time

More the friction more will be the tangential friction force acting on the rotor opposite to the tangential velocity. Hence greater friction coefficients of the catcher bearing material will result in rotor stopping relatively quickly. Hence more the friction less is the stoppage time.

A shown in Figure 8-2 the stoppage time decreases from about 1.4 seconds to about 0.72 seconds for corresponding friction coefficients of 0.22 and 0.1. (Other variables used were negative stiffness-35000 lbs. /in, radial clearance -0.00254 (10 mils), initial spin speed -10000 rpm).

8.3.3 *Effect of spin speed on rotor stoppage time*

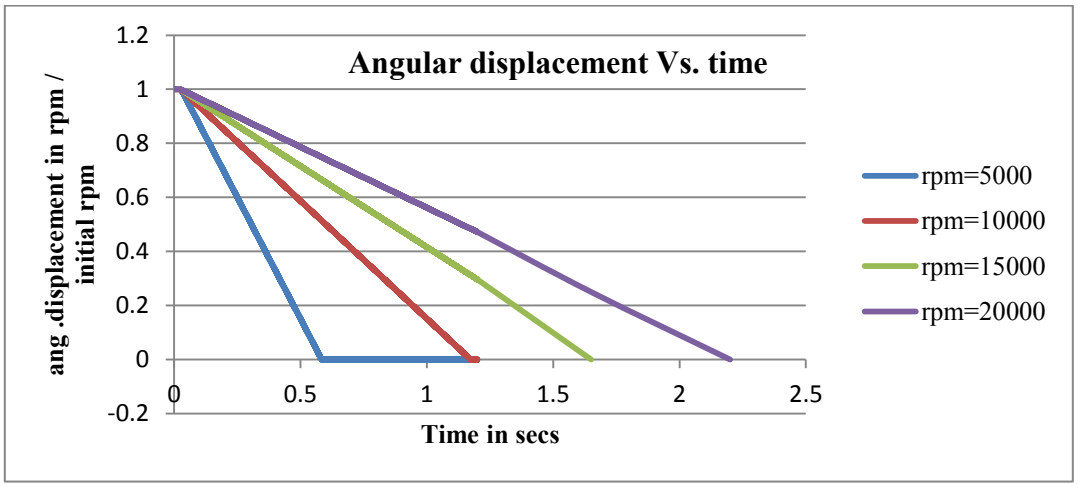

Figure 8-3 Effect of initial spin speed on stoppage time

The Figure 8-3 plots the percentage of initial spin speed (with respect to the initial spin speed) over time. Higher the spin speed of the rotor greater will be the energy at its disposal to overcome the tangential frictional force acting on the rotor .Lesser the initial rpm, lesser will be the time taken for the rotor to come to a halt. So, less is the stoppage time.

The stoppage time decreases from about 1.6 seconds to about 0.6 seconds for corresponding rotor rpms of 20000 and 5000. (Other variables used were negative stiffness-35000 lbs. /in, radial clearance -0.00254 (10 mils), friction-0.15).

8.3.4 *Effect of clearance on rotor stoppage time*

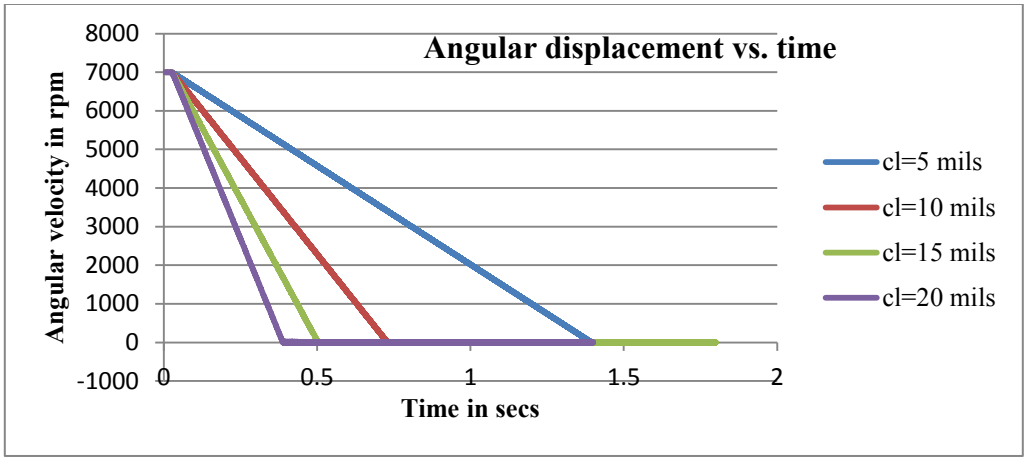

Figure 8-4 Effect of clearance on stoppage time

More the clearance more is the room for the rotor to accelerate more. More the rotor accelerates more force it has at its disposal before hitting the catcher bearing. More the force more is the deflection. More the deflection more is the normal force acting on the rotor. More the normal force more is the tangential frictional force acting opposite to tangential velocity of rotor. Hence more resistance and the rotor would have a relatively lesser stoppage time.

From Figure 8-4 we can conclude that the rotor stoppage time reduces from about 1.4 seconds to 0.4 seconds for a corresponding clearance of 5 mils to 20 mils. (Other variables used -negative stiffness-35000 lbs. /in,spin speed-10000 rpm, friction-0.15).

8.4 Effect of friction, clearance and spin speed on bearing force

The bearing force is the normal force exerted by the catcher bearing on to the rotor. The catcher bearing force is directly proportional to the deflection of the catcher bearing material by the hitting of the rotor on to it. This force is calculated as discussed in the previous section.

The plot of bearing force vs. time follows the same pattern for any set of input variables. A sample bearing force vs. time plot is as shown below (friction=0.15; radial clearance = .00254 m (10 mils); negative stiffness =35000 lbs. /in and spin speed of 7000 rpm).

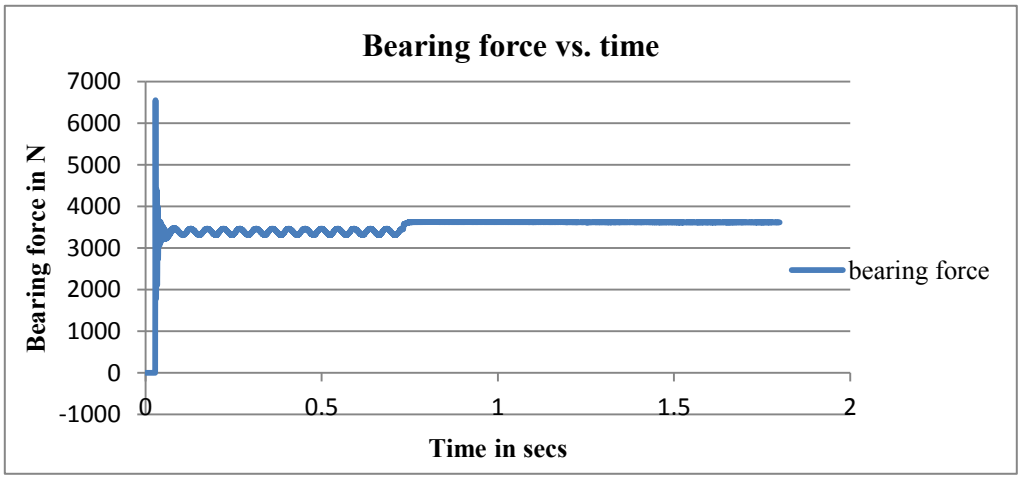

Figure 8-5 Bearing force vs. time

As shown in Figure 8-5, during the start of the rotor drop, the rotor hits against the catcher bearing surface with a good amount of acceleration (origin/center at levitated position to periphery). So it hits the catcher bearing with a good force which in turn produces a momentary high bearing force. After that there is a steady period which follows, with bearing force oscillating between a high and low until the rotor rpm comes to zero. Then there is a steady deflection which produces a steady bearing force at the end of stoppage time.

8.4.1 *Effect of friction on bearing force*

Table 8-1 shows the effect of friction on the bearing force encountered.

Table 8-1 Effect of friction on bearing force

Friction	**Maximum bearing force**	**Maximum bearing force during steady period**
no unit	**Newton**	**Newton**
0.05	6438	3606
0.1	6478	3551
0.15	6554	3465
0.2	6672	3352
0.25	6729	3304

Friction does not produce any noticeable increase / decrease in maximum bearing force (less than 5% of change). The tangential friction force acts only to bring the rotor to a quick stop by opposing its motion.

8.4.2 *Effect of spin speed on bearing force*

Table 8-2 reports effect of different spin speeds on the bearing force encountered.

Table 8-2 Effect of spin speed on bearing force

Spin speed	**Maximum bearing force**	**Maximum bearing force during steady period**
rpm	**Newton**	**Newton**
5000	3465	6585
7000	3465	6554
10000	3465	6483
15000	3465	6457
20000	3465	6462

Increasing spin speed does not produce any noticeable change in bearing force. The bearing force depends upon the force with which the rotor hits the catcher bearing, which in turn is dictated by the clearance and negative stiffness.

8.4.3 *Effect of clearance on bearing force*

More the clearance more will be the room for acceleration. More the acceleration more will be the force with which rotor hits the catcher bearing. Thereby more deflection results in bigger bearing force. Table 8-3 reports the effect of changing clearance on the bearing force encountered.

Table 8-3 Effect of clearance on bearing force

Clearance	Maximum bearing force	Maximum bearing force during steady period
10e-6m	Newton	Newton
127	3189	1779
254	6554	3465
381	9976	5118
508	13552	8929

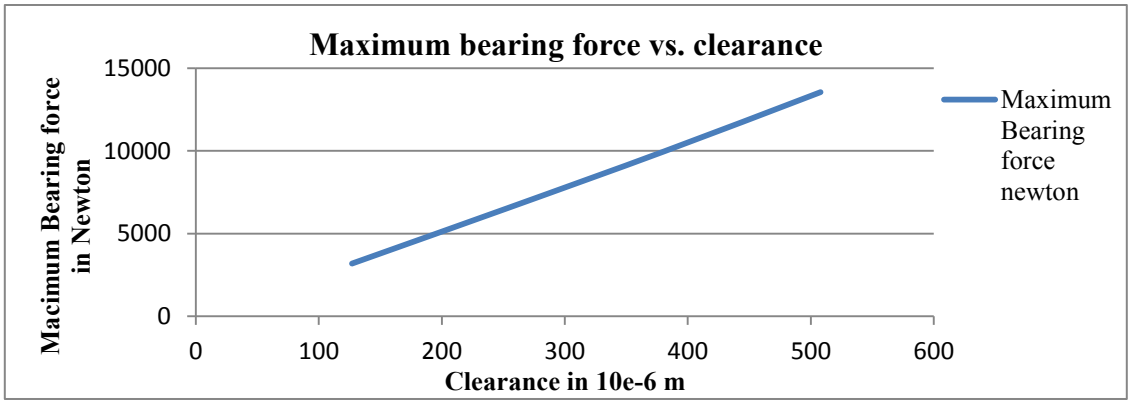

Figure 8-6 Maximum bearing force vs. clearance

Figure 8-6 shows the effect of changing clearance on peak bearing force.

Increasing the clearance from 5 mils to 20 mils increases the maximum bearing force from 3189N to 13552 N.

8.5 Effect of different variables on whirl velocity

The whirl velocity is the velocity with which the rotor revolves around in the central space of the magnetic bearing. Mathematically it is defined as:

$$\text{Whirl velocity} = \dot{\emptyset} = \frac{y\dot{z} - z\dot{y}}{y^2 + z^2}$$

The rotor is said to be in forward whirl if the rotor revolves around in the same direction as its direction of spin (around its axis of symmetry), which corresponds to a positive value of whir velocity.

The rotor is said to be in backward whirl if the rotor revolves around in the opposite direction to its direction of, which corresponds to a positive value of whirl velocity. The plot of whirl velocity over time has the same pattern for any set of input variables. Only magnitudes differ. The motion in Y and Z directions and plot of whirl velocity over time are as shown below.

(The plots are for friction=0.15; radial clearance=.00254m (10 mils); spin speed 7000 rpm; negative stiffness=35000 lbs. /in^2). The corresponding whirl velocity plot over time

is also shown. Motion in y direction over time is plotted in Figure 8-7

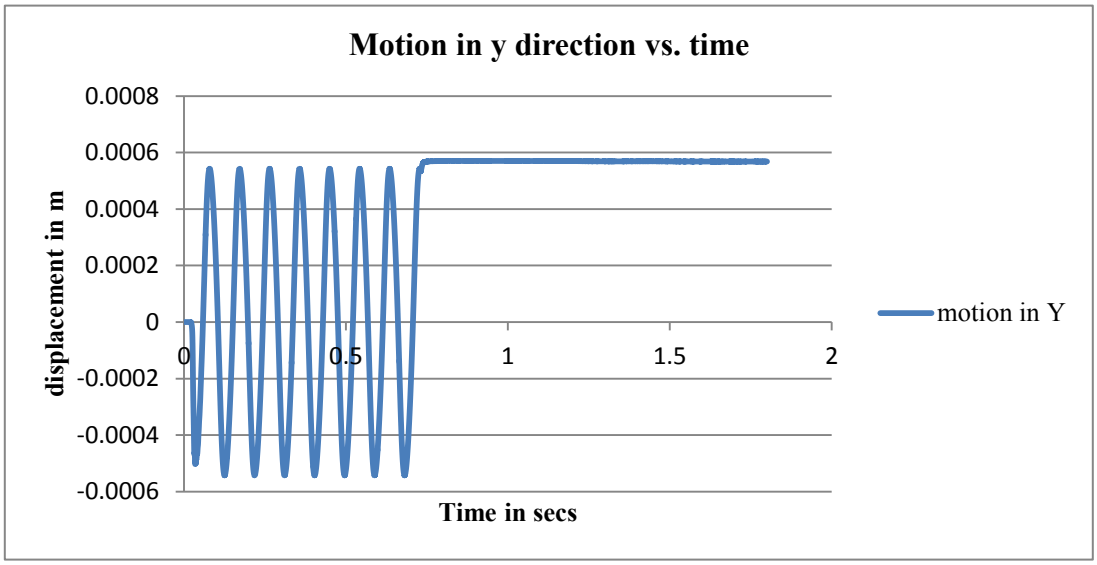

Figure 8-7 Motion in z direction vs. time

Motion in z direction over time is plotted in Figure 8-8

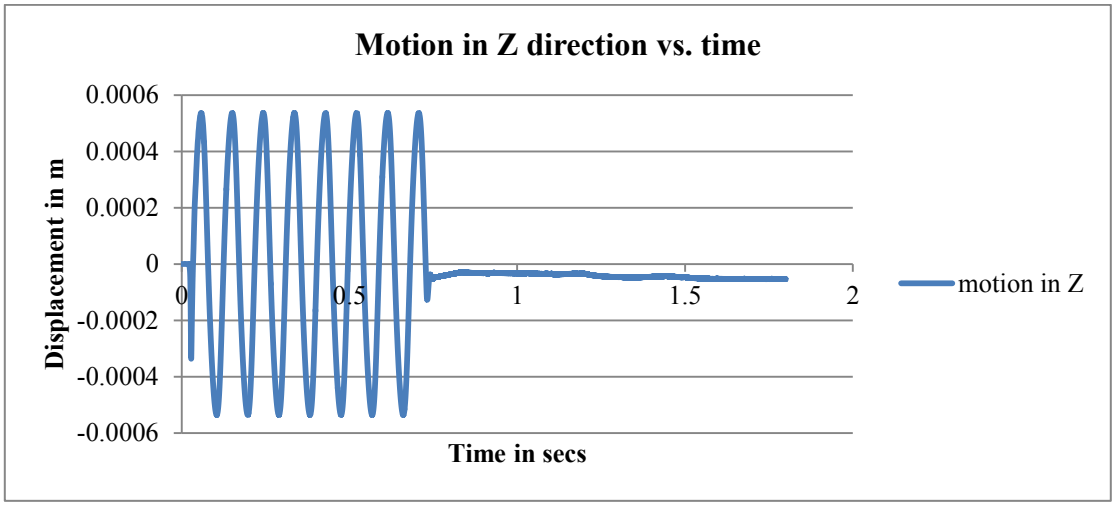

Figure 8-8 Motion in z direction vs. time

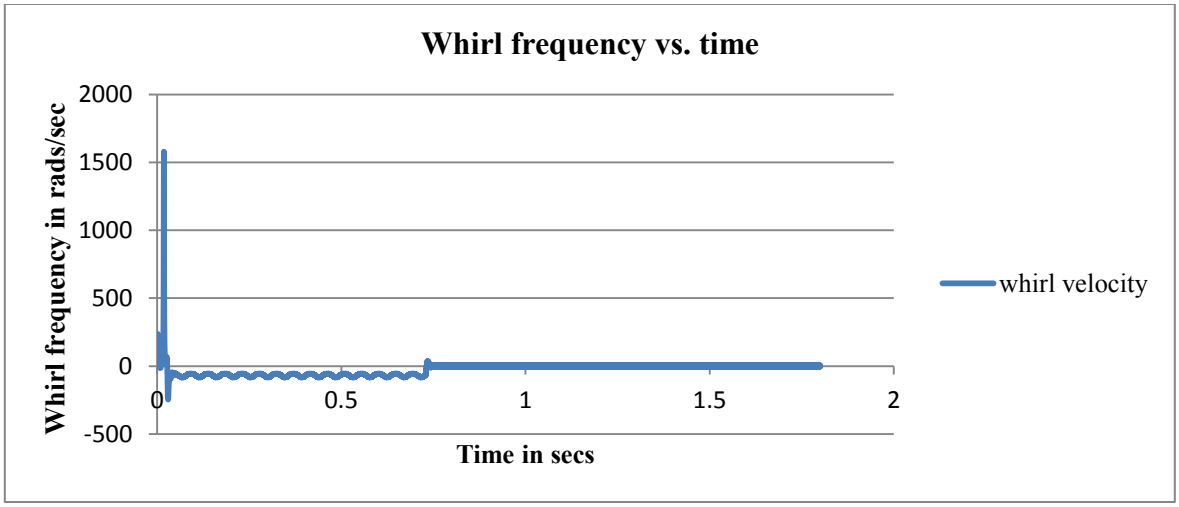

Figure 8-9 Whirl velocity vs. time

Figure 8-9 shows the effect of whirl velocity over time.Each of the system response (with regard to whirl velocity) follows the same pattern as above. There is a peak in whirl velocity in both directions during touchdown (it's very instantaneous and momentary). After that, there is a steady period of backward whirl (alternating between two values). After stoppage time the whirl velocity settles to zero.

8.5.1 *Effect of friction on whirl and whirl velocity*

Effect of friction on whirl velocity is reported as shown in Figure 8-10.

Table 8-4. Increasing the friction from, 0.05 to 0.25, increases the backward whirl velocity from 33 to 155 rad / sec.

Table 8-4 Effect of friction on whirl velocity

Friction	Maximum whirl velocity	Minimum whirl velocity during the intermediate steady stage	Minimum whirl velocity	Forward/ backward whirl
no unit	**rad/sec**	**radians/sec**	**rad/sec**	
0.05	1578	-33	-78	backward
0.1	1578	-57	-167	backward
0.15	1578	-83	-245	backward
0.2	1578	-154	-326	backward
0.25	1578	-155	-358	backward

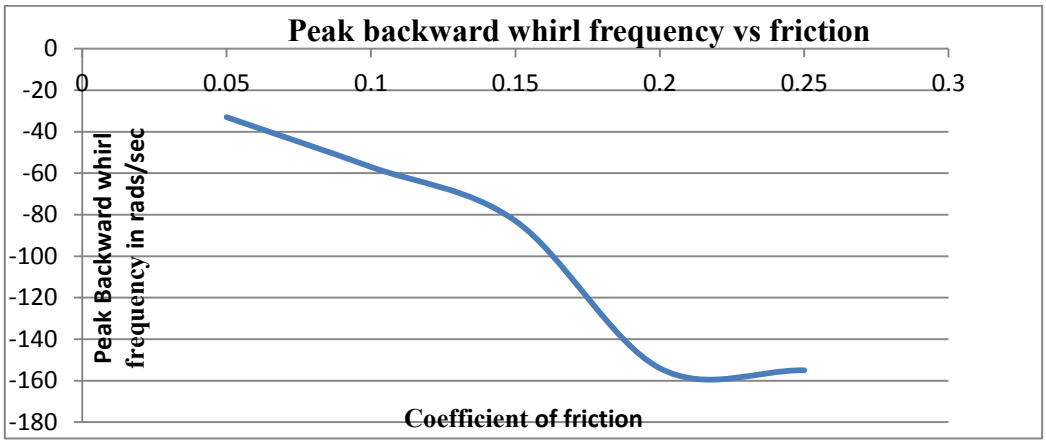

Figure 8-10 Peak backward whirl frequency vs. friction

8.5.2 *Effect of spin speed on whirl and whirl velocity*

Table 8-5 Effect of spin speed on whirl velocity

Spin speed	**Maximum whirl velocity**	**Minimum whirl velocity during the intermediate steady stage**	**Minimum whirl velocity**	**Forward/ backward whirl**
rpm	**radians/sec**	**radians/sec**	**radians/ sec**	
5000	1298	-85	-244	backward
7000	1578	-83	-245	backward
10000	3412	-83	-242	backward
15000	512	-82	-3702	backward
20000	662	-83	-1423	backward

As shown in Table 8-5 changing the spin speed from 5000 to 20000 rpm does not produce noticeable changes in whirl velocity. It changes only the instantaneous momentary spikes in whirl velocity.

8.5.3 *Effect of clearance on whirl and whirl velocity*

As shown in Table 8-6 below changing the clearance from 5 to 20 mils does not produce noticeable changes in whirl velocity.

Table 8-6 Effect of clearance on whirl velocity

Clearance	**Maximum whirl velocity**	**Minimum whirl velocity during the intermediate steady stage**	**Minimum whirl velocity**	**Forward/ backward whirl**
mils	**radians/sec**	**radians/sec**	**radians/sec**	
5	1578	-83	-247	backward
10	1578	-83	-245	backward
15	1578	-83	-245	backward
20	1578	-87	-246	backward

8.6 Effect of negative stiffness on rotor behavior

The negative stiffness factor decides how powerfully the rotor will be pulled towards the magnetic bearings. This in turn defines the way in which the rotor will behave. The orbit plots of different cases of negative stiffness values are given below.

Figure 8-11 gives the orbit plot for negative stiffness=6130 N/m (35 lbs. /in).

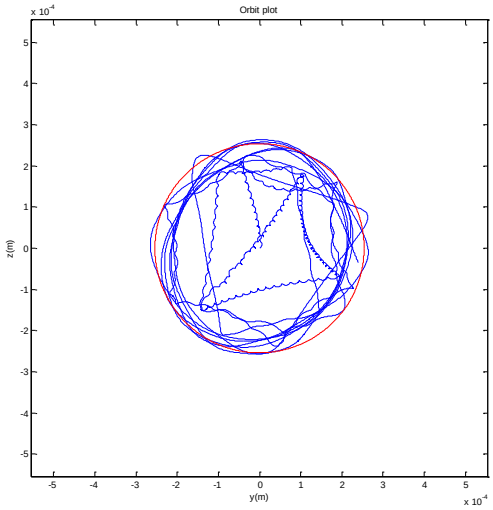

Figure 8-11 Orbit plot for negative stiffness=6130 N/m (35 lbs. /in)

Figure 8-12 gives the orbit plot for negative stiffness =613154 N/m (3500 lbs. /in).

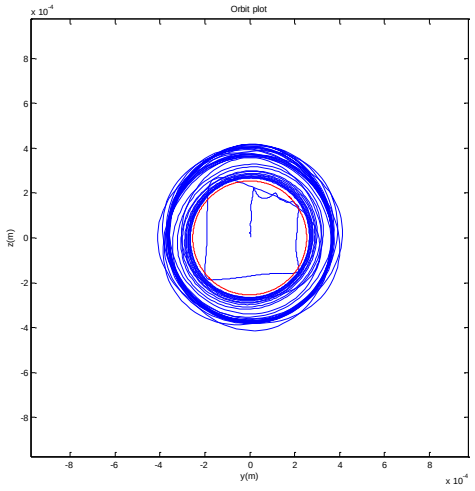

Figure 8-12 Orbit plot for negative stiffness =613154 N/m (3500 lbs. /in)

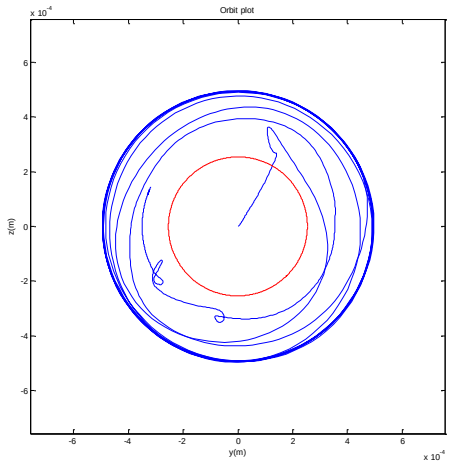

Figure 8-13 Orbit plot for negative stiffness =6131545 N/m (35000 lbs. /in)

Figure 8-13 gives the orbit plot for negative stiffness =6131545 N/m (35000 lbs. /in).

8.6.1 *Inference*

- As the amount of negative stiffness is increased one could see that greater is the tendency for the shaft to get stuck to the walls readily.

- More the negative stiffness less is the no of bumps onto the wall before the shaft gets stuck to the walls.

8.7 Simulation of as built conditions

8.7.1 *As built conditions*

Friction coefficient	:	0.15
Negative stiffness	:	6131545 N/m (35000lb/in)
Clearance (radial)	:	0.00254 m (10 mils)
Initial Angular velocity	:	5000 rpm

8.7.1.1 Orbit plot

The rotor whirls around the catcher bearing walls (backward whirl) before getting stuck to the walls due to negative stiffness from permanent magnets as shown in Figure 8-14.

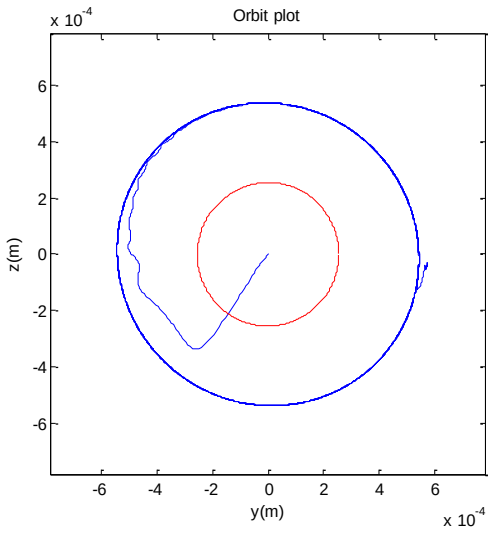

Figure 8-14 Orbit plot-as built conditions

8.7.1.2 Bearing force vs. time

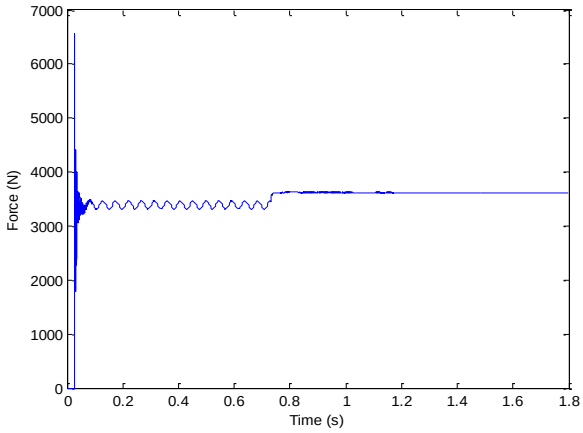

Figure 8-15 Bearing Force vs. time plot-as built conditions

The peak bearing force is about 6500 N for the as built conditions.

8.7.1.3 Displacement vs. time

The displacements in the y and z directions over time show oscillatory movements until the rotor loses its energy and it comes to equilibrium as shown in Figure 8-16 and Figure 8-17.

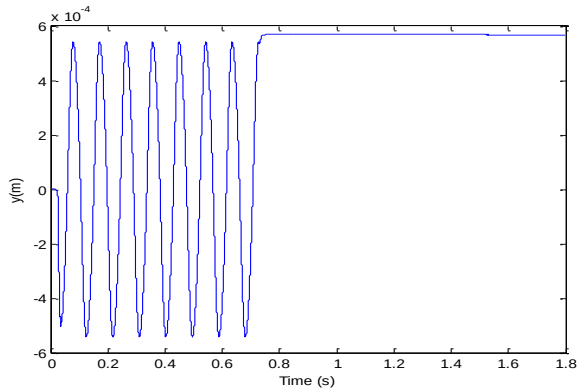

Figure 8-16 Displacement in y direction over time-as built conditions

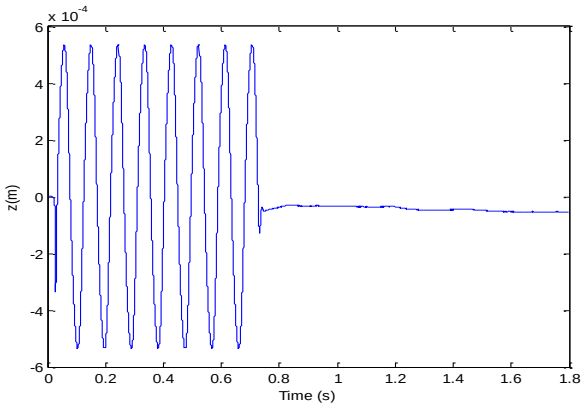

Figure 8-17 Displacement in z direction over time-as built conditions

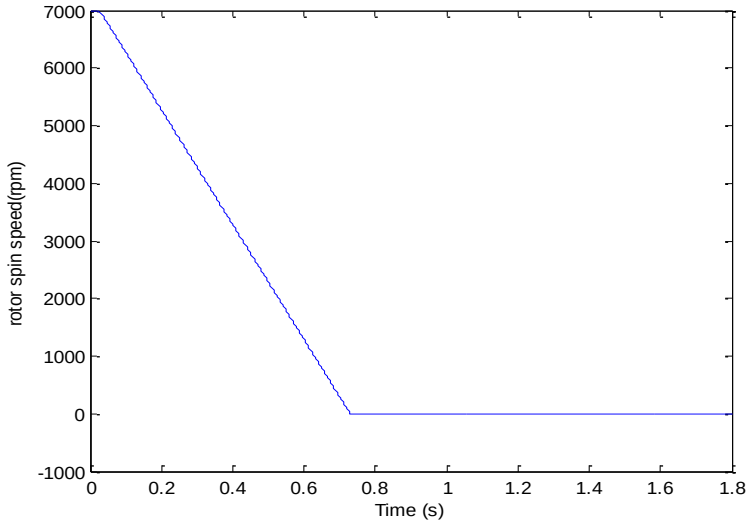

Figure 8-18 Rotor rpm vs. time – as built conditions

As the rotor loses its energy the rpm decreases to zero as shown in Figure 8-18.

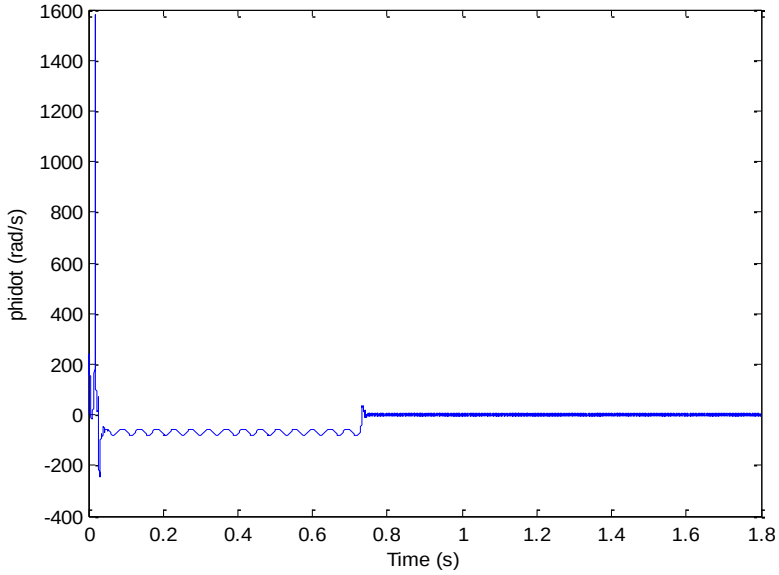

Figure 8-19 Whirl frequency vs. time– as built conditions

The whirl frequency is negative indicating that it's a backward whirl. The frequency becomes zero once the rotor loses its energy as shown in Figure 8-19.

8.8 Prediction of rolling/slipping

To predict whether the rotor is rolling/slipping against the walls of the catcher bearing, we need to investigate the relative velocity of the rotor. The rotor is supposed to have a relative velocity in the band of -1e-6 m/s to +1e-6m/s to if its rolls without slipping. If its beyond this band, the rotor would have a sliding motion thereby loosing energy.

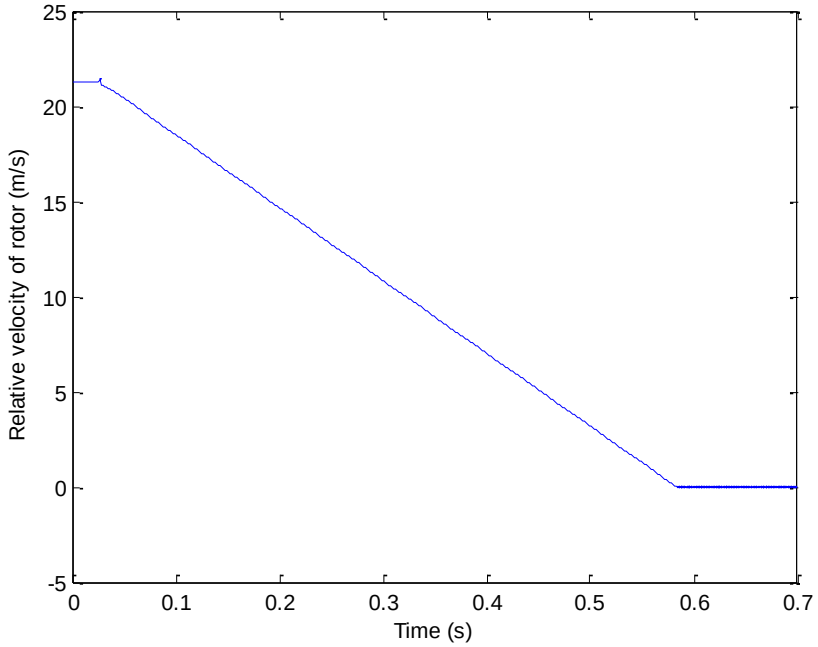

Figure 8-20 Relative velocity of the rotor in m/s vs. time

The plot of relative velocity of the rotor vs. time is as shown in Figure 8-20.

The plot shows that the relative velocity of the rotor is very high, which means that the rotor has a sliding motion. This explains why rotor loses energy.

The velocity of the bearing at the point of contact is as shown in Figure 8-21.

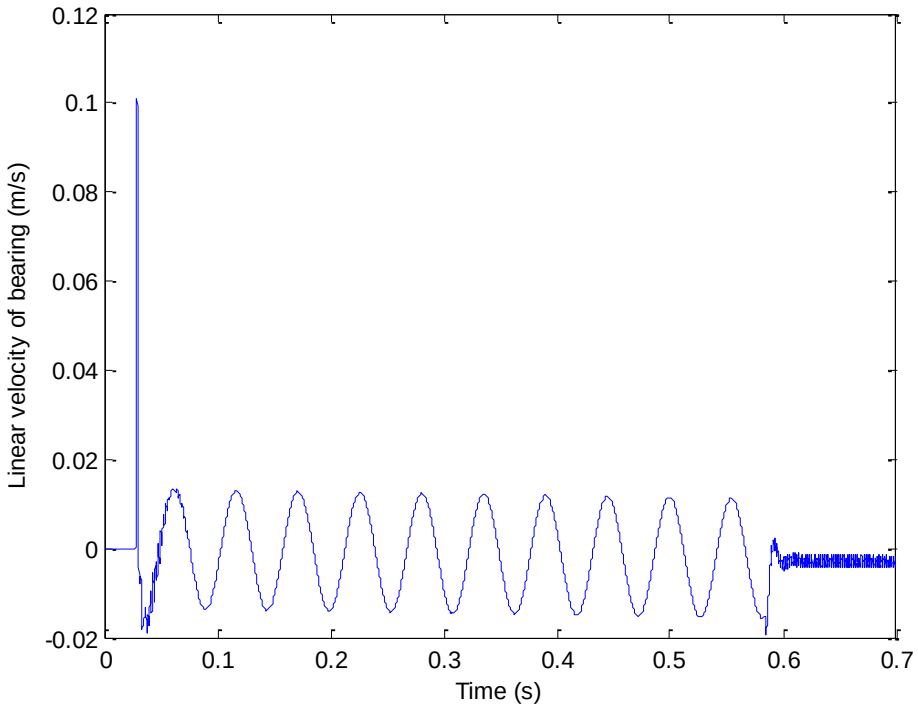

Figure 8-21 Velocity of bearing at the point of contact

The velocity of the bearing at the point of contact is almost zero, which is understandable from the fact that the catcher bearing is fixed and does not have a moving part.

8.9 Calculation of maximum stress at the point of contact

The contact forces have been calculated by modeling the contact as Hertzian contact between a cylinder and a plane. The maximum stress is given by the formula:

$$\text{Maximum stress} = \frac{2P}{\pi L b}$$

$$b = \sqrt{\left[\frac{4R(\lambda_1+\lambda_2)*P}{L}\right]}$$

$$\lambda_1 = \frac{1-\nu_1^2}{\pi.E_1} \qquad \lambda_2 = \frac{1-\nu_2^2}{\pi.E_2}$$

P - Force due to deflection

L - Contact length between catcher bearing and rotor

R - Radius of catcher bearing inner surface

b - Hertzian half-width of contact

The allowable stress (compressive) for catcher bearing material graph alloy is 8.2 X 10^7 N/m^2 (after a factor of safety of 1.5). The maximum stress under as-built conditions is as shown in Figure 8-22.

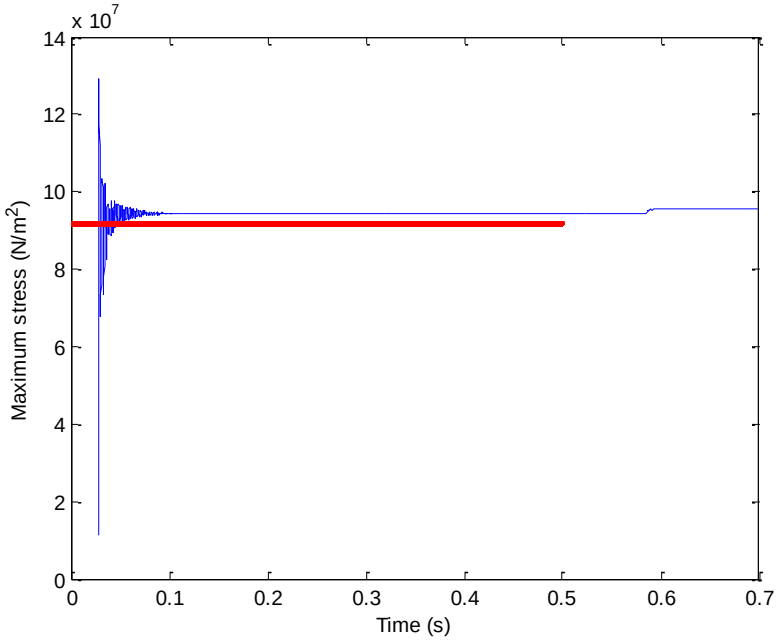

Figure 8-22 Maximum stress in as built conditions

It could be noticed that the maximum stress is more than the allowable stress when the rotor plunges onto the catcher bearing after rotor is dropped. So it might be noted that the catcher bearing system might have to be redesigned for safe operation.

8.10 Conclusion from parametric studies

The effect of increasing negative stiffness from 10000 lbs. /in to 35000 lbs. /in is to lessen the stoppage time from 4.1 seconds to 1 second.

1. The effect of increasing the friction from 0.05 to 0.20 is:

i. To decrease the stoppage time from 1.5 seconds to 0.5 seconds

ii. To increase the backward whirl from 33 rad/sec to 155 rad /sec

2. The effect of increasing the clearance from 5 mils to 20 mils is:

   a. To reduce the stoppage time from 1.4 to 0.4 seconds

   b. To increase the peak bearing force from 3189 N to 13552 N

3. The effect of increasing the initial spin speed from 5000 to 20000 rpm is to increase the rotor stoppage time from 0.6 seconds to 1.6 seconds.

4. The rotor slides along the walls of the catcher bearing during whirl motion which explains the rotor loses its energy (rpm reduces to zero).

5. The maximum stress encountered under as built conditions (for rotor drop) is more than the allowable limits. Hence the catcher bearing system might have to be redesigned to allow for safe operation.

9. CONCLUSIONS AND FUTURE WORK

9.1 Conclusions

- Successful methods were developed to assemble all the components viz bearings and motor along with the stator plates inside the test rig.
- However there were some problems with respect to maintaining sufficient axial preload to prevent any small motion of the bearing to levitate the shaft.
- Otherwise the integrity of all other components of the test rig was maintained without any damage to them.
- After assembly while trying to levitate the shaft, the maximum horizontal movement of the shaft achieved was about 8-10 mils; which would mean sufficient concentricity of the components was achieved.
- Though the catcher bearing was designed and fabricated, interference would not maintain itself at higher temperatures.
- Other accessories like sensor holders and other assembly fixtures were successfully designed , fabricated, installed and proven in use.
- The sensors were calibrated, tested and the position of the shaft was successfully determined consistently by them.
- Testing, calibration and installation of all other control electronics was done.

- The wiring between internal components of the test rig and all other external components/control electronics was accomplished and tested.
- A dynamic model of the falling rotor into a system of catcher bearings and magnetic bearings was successfully modeled and simulated.
- A parametric study of the effect of the spin speed and coefficient of friction was completed.
- Safety measures were successfully implemented to ensure 100% safe operating and testing conditions of the test rig.

9.2 Future work

- To make design modifications in the catcher bearing system so that it would allow sufficient axial preload to be maintained even after loosening the catcher bearing.
- The method of disassembly to take all the components out of the test rig, without any damage to them needs to be devised. Probably it could be achieved by using a threaded rod which goes into the internal threads of the bearings and motor(the dimension of the internal thread inside the radial bearings was determined as M20 x 1.5).

- The different pieces of the rotor need to be removed and the shims have to be reinserted so as to center the shafts approximately in their corresponding bearing/motor.

- All the internal parts need to be reassembled again using the standard assembly methods and fixtures developed.

- The levitation of the shaft needs to be achieved. In other words the shaft needs to be centered in the central concentric space of the bearing and motor.

- In the levitated position the motor needs to power the rotor through the torque it develops.

- The levitation and running of the motor need to be repeated at higher temperatures (1000 ^{o}F).

- The catcher bearing system might have to be redesigned for safe operation and to withstand the maximum stress encountered during rotor drop.

REFERENCES

[1] Schweitzer, G., Bleuler, H. and Traxler, A., 1994, "Basics, Properties and Applications of Active Magnetic Bearings," Active Magnetic Bearings, **210**, pp. 1-112.

[2] Zhengxin, Z., 2010, "High temperature, buried permanent magnet, brushless dc motor," M.S. thesis, Department of Mechanical Engineering, Texas A&M University, College Station.

[3] Gandhi, V R., 2008, "High temperature, permanent magnet biased, magnetic bearings," M.S. thesis, Department of Mechanical Engineering, Texas A&M University, College Station.

[4] Sun, G., 2006, "Detailed Ball Bearing Model for Magnetic Suspension Auxiliary Service," Journal of Sound and Vibration, **269**, pp. 933–963.

[5] Sun, G., 2006, "Rotor Drop and Following Thermal Growth Simulation Using Detailed Auxiliary Bearing and Damper Models," Journal of Sound and Vibration, **289,** pp. 334–359.

[6] Kärkkäinen, A., Sopanen, J., and Mikkola, A., 2006, "Dynamic Simulation of AMB Supported Electric Motor during Rotor Drop on Retainer Bearings," Journal of Sound and Vibration, **306**, pp. 601-617.

[7] Kirk, R G., 1999, "Evaluation of AMB Turbo Machinery Auxiliary Bearings," Journal of Vibration and Acoustics, **121,** pp.156-162.

[8] Kirk, R G., Ishii, T., 1996, "Transient Response Technique Applied to Active Magnetic Bearing Machinery during Rotor Drop," Journal of Vibration and Acoustics, **118,** pp. 154-163.

[9] Kirk, R G., Ishii, T., 1993, "Transient Rotor Drop Analysis of Rotors Following Magnetic Bearing Power Outage," In Proceedings of MAG '93 - Magnetic Bearings, Magnetic Drives and Dry Gas Seals Conference & Exhibition, Alexandria, VA, **1**, pp. 53-61.

[10] Kirk, R G., Raju, K V S., Ramesh, K., 1997, "Evaluation of AMB Rotor Drop Stability," The Eighth Workshop on Rotordynamic Instability Problems in High Performance Turbomachinery, Turbomachinery Laboratory, Texas A & M University,

Texas.

[11] Sortore, C. K., Allaire, P. E., Maslen, E. H., Humphris, R. R., and Studer, P. A., 1990, "Permanent Magnetic Biased Bearings—Design, Construction, and Testing," Proc. of the Second International Symposium on Magnetic Bearings, Tokyo, **2**, pp. 175–182.

VITA

Ashwanth Narayanaswamy was born to Sugantha and Narayanaswamy in India. He pursued his primary and secondary education in Coimbatore, India. He received his Bachelor of Engineering degree in mechanical engineering from Kumaraguru College of Technology, India, in the year 2003. He received his MBA in marketing and finance from St. Joseph's College of Business Administration, Bangalore, India in 2005.

Ashwanth Narayanaswamy started his MS in mechanical engineering degree at Dwight Look College of Engineering at Texas A&M University in Spring 2008. He began his research in the Vibration Control and Electro mechanics Lab, under Dr. Alan Palazzolo in Fall 2008. He received his M.S. degree in mechanical engineering in May 2011.

Ashwanth can be reached at:

Department of Mechanical Engineering

c/o Dr.Alan Palazzolo,

3123 TAMU,

College Station, TX 77843- 3123, USA.

ashwanthnarain@gmail.com